STRESS REDISTRIBUTION AROUND FIBER BREAKS IN UNIDIRECTIONAL STEEL FIBER COMPOSITES UNDER LONGITUDINAL TENSILE LOADING

A THESIS SUBMITTED TO
THE GRADUATE SCHOOL OF NATURAL AND APPLIED SCIENCES
OF
MIDDLE EAST TECHNICAL UNIVERSITY

BY

ÇAĞLAR MUTLU

IN PARTIAL FULFILLMENT OF THE REQUIREMENTS
FOR
THE DEGREE OF MASTER OF SCIENCE
IN
MECHANICAL ENGINEERING

SEPTEMBER 2019

Approval of the thesis:

STRESS REDISTRIBUTION AROUND FIBER BREAKS IN UNIDIRECTIONAL STEEL FIBER COMPOSITES UNDER LONGITUDINAL TENSILE LOADING

submitted by **ÇAĞLAR MUTLU** in partial fulfillment of the requirements for the degree of **Master of Science in Mechanical Engineering Department, Middle East Technical University** by,

Prof. Dr. Halil Kalıpçılar
Dean, Graduate School of **Natural and Applied Sciences**

Prof. Dr. M. A. Sahir Arıkan
Head of Department, **Mechanical Engineering**

Prof. Dr. Fevzi Suat Kadıoğlu
Supervisor, **Mechanical Engineering, METU**

Assoc. Prof. Dr. Barış Sabuncuoğlu
Co-Supervisor, **Mechanical Engineering, Hacettepe Uni.**

Examining Committee Members:

Prof. Dr. Haluk Darendeliler
Mechanical Engineering, METU

Prof. Dr. Fevzi Suat Kadıoğlu
Mechanical Engineering, METU

Prof. Dr. Serkan Dağ
Mechanical Engineering, METU

Assoc. Prof. Dr. Merve Erdal Erdoğmuş
Mechanical Engineering, METU

Assoc. Prof. Dr. Barış Sabuncuoğlu
Mechanical Engineering, Hacettepe University

Date: 03.09.2019

I hereby declare that all information in this document has been obtained and presented in accordance with academic rules and ethical conduct. I also declare that, as required by these rules and conduct, I have fully cited and referenced all material and results that are not original to this work.

Name, Surname: Çağlar Mutlu

Signature:

ABSTRACT

STRESS REDISTRIBUTION AROUND FIBER BREAKS IN UNIDIRECTIONAL STEEL FIBER COMPOSITES UNDER LONGITUDINAL TENSILE LOADING

Mutlu, Çağlar
Master of Science, Mechanical Engineering
Supervisor: Prof. Dr. Fevzi Suat Kadıoğlu
Co-Supervisor: Assoc. Prof. Dr. Barış Sabuncuoğlu

September 2019, 95 pages

Due to their significant advantages, such as high strength-to-weight, stiffness-to-weight ratio, flexibility in design and excellent fatigue resistance, use of fiber-reinforced composite materials has increased remarkably. Because of their widespread use, a comprehensive understanding of failure of composite materials is an important issue. Recently, steel fibers are increasingly seen as reinforcement material in composites thanks to their advantages like ductility, high stiffness and wide range of production diameters. Strength and failure strain of composites are calculated by strength models. Stress concentration factor and ineffective length are two important input parameters for these strength models. Some parameters that arise from the properties of steel fibers may affect the mechanical behavior of steel fiber composites under loading. In this study, effects of these parameters on stress concentrations and ineffective length in unidirectional steel fiber composites under longitudinal tensile loading are investigated. A parametric study is performed by using 3D finite element models with random fiber packings. Non-circular cross-sections of steel fibers are shown to have a negligible effect on the results. Also, it is found that mechanical properties of constituent materials and applied strains cause differences in the results. Loading and reloading processes are found to have similar results for same applied strains. Reloading to a lower loading levels than the one in loading resulted in different results.

Keywords: Steel Fiber Composites, Stress Concentrations, Ineffective Length, Finite Element Analysis, Random Fiber Distribution

ÖZ

BOYUNA ÇEKME YÜKLEMESİ ALTINDAKİ TEK YÖNLÜ ÇELİK ELYAFLI KOMPOZİTLERDE ELYAF KIRIKLARI ÇEVRESİNDEKİ GERİLİMİN YENİDEN DAĞILIMI

Mutlu, Çağlar
Yüksek Lisans, Makina Mühendisliği
Tez Danışmanı: Prof. Dr. Fevzi Suat Kadıoğlu
Ortak Tez Danışmanı: Doç. Dr. Barış Sabuncuoğlu

Eylül 2019, 95 sayfa

Yüksek mukavemet/ağırlık, sertlik/ağırlık oranları, tasarımda esneklik ve mükemmel yorulma direnci gibi avantajlarından dolayı elyaf takviyeli kompozit malzemelerin kullanımı kayda değer bir şekilde artmıştır. Geniş ölçekli kullanımlarından dolayı kompozit malzemelerin başarısızlıklarını kapsamlı bir şekilde anlamak önemli bir konudur. Süneklik, yüksek sertlik ve geniş üretim çapı aralıkları gibi avantajlarından dolayı çelik elyaflar son zamanlarda kompozitlerde, artan bir şekilde takviye malzemesi olarak kullanılmaktadır. Kompozitlerin mukavemet ve başarısızlık gerinimi değerleri mukavemet modelleri aracılığıyla hesaplanmaktadır. Gerilme konsantrasyonu faktörü ve etkisiz uzunluk mukavemet modellerinde girdi olarak kullanılan iki önemli etkendir. Çelik elyafların özelliklerinden dolayı ortaya çıkan bazı parametreler yük altındaki çelik elyaflı kompozitlerin mekanik davranışlarını etkileyebilirler. Bu çalışmada, bu parametrelerin, boyuna yük altındaki çelik elyaflı kompozitlerdeki gerilme konsantrasyonu ve etkisiz uzunluk sonuçları üzerindeki etkileri araştırılmaktadır. Rastgele dağılımlı elyaflar içeren üç boyutlu sonlu eleman modelleri kullanılarak parametrik bir çalışma gerçekleştirilmiştir. Çelik elyafların dairesel olmayan kesitlerinin sonuçlar üzerinde ihmal edilebilir etkisi olduğu gösterilmiştir. Bunun yanında, bileşen malzemelerin mekanik özelliklerinin ve gerinim girdilerinin sonuçlarda farklılıklara sebep olduğu bulunmuştur. Yükleme ve tekrar yükleme süreçlerinin aynı yükleme seviyesi altında benzer sonuçlara sebep olduğu bulunmuştur. Yüklemeye göre daha düşük seviyelerde geri yükleme durumu farklı sonuçlara neden olmuştur.

Anahtar Kelimeler: Çelik Elyaflı Kompozitler, Gerilme Konsantrasyonları, Etkisiz Uzunluk, Sonlu Eleman Analizi, Rastgele Elyaf Dağılımı

To my family

ACKNOWLEDGMENTS

I would like to express my deepest gratitude to my supervisors Prof. Dr. F. Suat Kadıoğlu and Assoc. Prof. Dr. Barış Sabuncuoğlu for their invaluable help, guidance and support.

I would also like to express my special gratitude to my parents Demet Mutlu and Şahap Mutlu and to my sister Pınar Mutlu for all their love, patience and encouragement.

TABLE OF CONTENTS

CHAPTERS

LIST OF TABLES

TABLES

LIST OF FIGURES

FIGURES

LIST OF ABBREVIATIONS

SCF	Stress Concentration Factor
3D	Three Dimensional
RVE	Representative Volume Element

LIST OF SYMBOLS

$z*$	Axial distance of a certain plane from crack plane
SCF_{avg}	Cross-sectional average stress concentration factor
z	Axial distance
$\sigma_{z,avg}$	Cross-sectional average stress on a certain plane
L	Model length
SCF_{peak}	Peak stress concentration factor
$\sigma_{z,peak}$	Peak stress on a certain plane
r_f	Fiber radius
w	Model width
V_f	Fiber volume fraction
R_h	Distance between hexagonal fiber center and corner
R	Circular fiber radius
E	Young’s modulus
ν	Poisson’s ratio
ε_p	Plastic strain
ε_{total}	Total strain
σ	Stress
δ	Displacement
$S11$	Axial stress

E_{ii}	Elastic moduli in i direction
ν_{ij}	Poisson’s ratio
G_{ij}	Shear modulus
d	Surface-to-surface distance
d_h	Surface-to-surface distance of hexagonal fibers
d_c	Surface-to-surface distance of circular fibers
ε_e	Elastic strain
$\sigma_{residual}$	Residual stress

CHAPTER 1

INTRODUCTION

Due to their significant advantages, such as high stiffness- and strength-to-weight ratio, flexibility in design and lower production costs compared to commonly used materials, use of fiber-reinforced composite materials in many areas has increased over the time. Also, complex shapes can be manufactured in one operation with the advantage of reduced part count. Naturally, they have some disadvantages regarding difficulties in repairing, storage and requirement of special equipment, but these can be disregarded and considered as minor problems in some applications in which their advantages yield much better profits. Because of their widespread use, a comprehensive understanding of failure mechanisms of composite materials is an important issue. Therefore, studies conducted in this field allow designers and engineers to overcome the challenges encountered and design better parts for the industry. Although, in some cases, there could be visible warning, a complete failure of fiber-reinforced composite materials mostly occurs without an apparent sign of damage and so, predicting the failure of a composite is not an easy task. In most cases, failures of multidirectional and unidirectional composites coincide with each other [1]. Therefore, understanding the failure mechanism of unidirectional composites is an important task and it gives insight about the nature of the composite failure. Carbon, glass and aramid fiber-reinforced composites are more commonly used in the industry. However, due to some advantages like ductility and wide range of production diameter, steel fiber-reinforced composites have also become popular [2]. Besides these advantages, steel fibers are nearly as stiff as carbon fibers. Therefore, understanding the failure mechanism of steel fiber-reinforced composites is necessary. Compared to carbon and glass fibers, higher density of steel fibers may cause problems in weight sensitive applications. For those applications, in which ductility is also necessary, hybrid composites including carbon and steel fibers can be a solution that provides ductility with a small increase of weight [3]. Another disadvantage of steel fibers is that the interfacial strength between matrix and steel fibers is low. Therefore, silane coupling agents are used to increase the interfacial strength [4,5]. Besides increasing the interfacial strength, these coupling agents improve chemical and moisture resistances and thermal properties of the material [5]. Steel as a reinforcement material is generally used in concrete and automobile tires. However, to the best of author's knowledge, polymer composites with the reinforcement of steel fibers in micro level are not available in structural applications yet. Therefore, they are recently in research phase. In the future, because of the advantage of high toughness and consequently high energy absorption, they can be potentially used in the applications in which impact resistance is important, such as car bumpers and helmets [6,7].

One of the common ways to estimate the strength and failure strain of the composite is the strength models [1,8]. Strengths of each fiber in the composite are different than each other and they follow a statistical Weibull strength distribution [9]. Due to the differences in fiber strengths, some of the fibers fail earlier. These statistical distributions are implemented in the strength models. Stress concentration factor (SCF) and ineffective length are two important input parameters for strength models of composite materials. As mentioned in Smith et. al. [10], in case of a broken fiber, that fiber locally loses its load-carrying capability and that load is distributed to the other surrounding fibers which causes the load on them to increase. This relative increase on the surrounding fibers is called SCF. Due to the load increase in the neighboring fibers, failure probability of those fibers increases. After a critical number of fiber failures, a complete failure in the composite material takes place. Therefore, SCF term becomes important for predicting the strength of the material. As mentioned in Swolfs et. al. [11], stress redistribution is not constant through the cross-section of an intact fiber after a fiber break which is shown in Figure 1.1. Stresses are greater in the regions closer to the broken fiber.

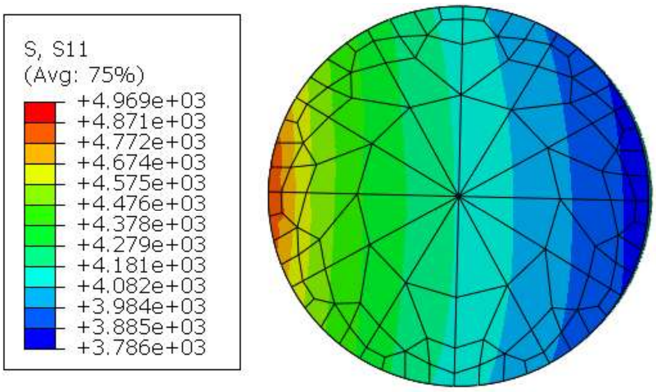

Figure 1.1. Stress field of an intact fiber in case of a broken fiber.

Cross-sectional average SCF on a certain plane, $z*$, is defined as the relative increase in average fiber stress with respect to stress value on a plane far away from the break plane. SCF definition in [12] is used for the calculations. Its formulation is given as follows [11]:

$$SCF_{avg}(z = z*) = \frac{\sigma_{z,avg}(z = z*) - \sigma_{z,avg}(z = L)}{\sigma_{z,avg}(z = L)} * 100\% \qquad \text{(Eq. 1.1)}$$

The peak SCF on a certain plane, $z*$, is found similarly. It is calculated with respect to the peak stress value on the fiber cross-section on that plane. Its formulation is given as follows:

$$SCF_{peak}(z = z*) = \frac{\sigma_{z,peak}(z = z*) - \sigma_{z,avg}(z = L)}{\sigma_{z,avg}(z = L)} * 100\% \qquad \text{(Eq. 1.2)}$$

Ineffective length definition in [13] was used for the calculations. After broken fiber loses its load-carrying capability, shear stress takes place on the surrounding matrix. Due to the shear stress on the surrounding matrix, the load is transferred back to the broken fiber over a length in longitudinal direction (z-direction). Ineffective length is defined in [11] as ‘twice the fiber length over which 90% of strain recovery occurs’. While getting away from the break plane, stress concentrations on the intact fibers decreases and stresses on them turn back to their initial values over a length. Therefore, ineffective length is also an important term while making calculations for the prediction of material's strength. Calculating SCFs and ineffective lengths is the first step while predicting the strength and failure strain of a material. In later studies, these calculated values can be used as an input for mathematical strength models to estimate the strength of the materials.

1.1. Aims and Objectives of the Study

The main aim of this study is to investigate the effects of different parameters on SCF and ineffective length for unidirectional steel fiber-reinforced composites in case of a broken fiber under longitudinal tensile loading by developing numerical models with finite element approach. Finite element models were created by using parametric modelling strategy developed in programming language Python®. A script compatible with the finite element software Abaqus® was used for this purpose. In some cases, creating a finite element model by using the user interface takes hours or even days for detailed and complex models. In a parametric study, several of these models should be created and creation of these costs too much time. Also, correcting a mistake in a model may take hours. By using the script in a parametric study, the creation time of models is significantly reduced, and complex models are created easily. For example, by changing a few lines in the script, finite element models with completely different properties can be created in a few minutes.

As the first objective of this study, the effects of cross-sectional shape of fibers on SCF and ineffective length were investigated in terms of both peak and cross-sectional average fiber stresses. Unlike carbon and glass fibers, final product of steel fibers has cross-sectional shapes of irregular polygons due to their manufacturing processes [14]. Since there is a possibility of higher stress concentrations on the fibers with polygonal shapes, hexagonal and circular cross-sections were compared for this purpose. All finite element models were created with randomly distributed fibers to have more realistic models. Also, all fibers were randomly rotated around their longitudinal axes in the models with hexagonal-shaped fibers.

Secondly, steel fibers have an advantage of high ductility compared to carbon and glass fibers, which results in that steel fiber composites can resist higher strains until fracture. Therefore, effects of mechanical behaviors of the materials on SCF and ineffective length were examined in terms of cross-sectional average fiber stresses. Also, effects of different strain inputs in the elasto-plastic range were analyzed.

Lastly, in some cases, the materials do not always remain in the loaded condition, they may be unloaded and reloaded. In those cases, stress redistribution around and at the interface of a broken fiber may be different. Therefore, SCF results of intact fibers and stress recovery profiles of broken fibers for unloading and reloading processes were obtained in this study.

1.2. Research Methodology

The study starts with an extensive literature survey. Previous studies related with the current subject are researched and the current subject is selected. Then, a parametric modelling strategy is utilized to create several finite element models with different properties. After that, using these finite element models, several analyses are performed to investigate the effects of different parameters on the results. For each analysis, the effects of a different aspect on the results are examined. All results are given in the figures and/or tables and they are discussed in related sections. Finally, the key findings and outcomes of the entire study are presented and suggestions for future work are given.

1.3. Outline of the Study

The current study includes 7 chapters whose summaries are given below:

Chapter 2, Literature Survey: Previous studies related with the current study are presented.

Chapter 3, Development of Finite Element Models for Unidirectional Steel Fibers: Parametric modelling methodology is presented. Each step for creation of finite element models are described in detail. Accuracy of the created finite element models are verified.

Chapter 4, Effects of Cross-sectional Fiber Shape on SCF and Ineffective Length: The effects of different cross-sectional shape of fibers on SCF and ineffective length are investigated. Hexagonal and circular shapes are compared. The results are examined in terms of both peak and cross-sectional average fiber stresses.

Chapter 5, Effects of Mechanical Behavior of Materials on SCF and Ineffective Length: Effects of different mechanical properties of materials on SCF and ineffective length are examined. Mechanical behavior of each constituent material is examined separately. Effects of different strain inputs are analyzed.

Chapter 6, Stress Concentrations in Steel Fibers after Unloading and Reloading: Procedure for unloading and reloading analyses is described. Stress concentration factors and ineffective length results at the end of unloading and reloading processes are obtained.

Chapter 7, Conclusions: The summary of the study is presented. Key findings and outcomes of the study are given, and further recommendations are made.

CHAPTER 2

LITERATURE SURVEY

There are many studies in the literature regarding the stress concentrations, ineffective lengths and strength of the fiber-reinforced composites. Various computational and experimental methods such as continuum theory of elasticity, shear lag and finite element approaches etc. were used concerning the several aspects that influences the stress concentrations and composite strengths. Each one of these methods has distinctive advantages and disadvantages.

A shear lag model was developed by Hedgepeth [15] to calculate SCFs within elastic limits. Fibers were modelled to be aligned in a single row of parallel fibers with equal distances. In this model, it was assumed that fibers and matrix can carry only normal and shear loads, respectively. SCF of 33% was found in the study. The model was improved in a subsequent study by aligning the fibers with square and hexagonal arrays [16]. SCFs of 14.6% and 10.4% were found for square and hexagonal packings, respectively. Nedele and Wisnom [17] performed a finite element analysis with a broken fiber and six equally-spaced fibers and obtained 5.8% SCF which is much lower than Hedgepeth's prediction. In [18], 3D finite element models and shear lag models were compared for polymer-matrix and aluminum-matrix composites with hexagonal fiber packing. Stress redistribution calculations were found to be accurate in shear lag models for high fiber/matrix stiffness ratios and high fiber volume fractions whereas there were some discrepancies in the other cases due to neglecting fiber shear deformation and matrix load carrying capability. To examine the damage accumulation in carbon/epoxy composites, results of a multi-scale model and computed tomography experiments were compared in [19]. The results obtained from the experiments and the model were found to be in good agreement. Both showed that the failure progression of the composite begins with a single fiber break and evolves into a cluster of broken fibers at higher loads which results in a complete failure of the material in the end. Similar results were obtained by Thionnet et. al. [20] using a multi-scale model. Callens et. al. [6] performed quasi-static tensile tests to examine the properties of steel fiber composites with brittle and ductile matrices. Steel fiber composites were found to have a failure strain value around 3-4 times the failure strain of glass and carbon fiber composites with brittle epoxy matrix. Using ductile matrix improved the failure strain around 75% compared to the case with brittle matrix.

Some of the studies took the interfacial properties into consideration. In [21], a modified shear lag model was used to determine the SCFs with the inclusion of matrix stiffness and interfacial damage. The study showed that the stress concentrations are increased with increasing interface shear strength and fiber/matrix stiffness ratio. Also, interfacial shear yielding was found to reduce the stress concentrations. Landis and McMeeking [22] improved the Hedgepeth's study by including fiber/matrix interface sliding and matrix stiffness. These two terms were found to decrease the stress concentrations. In [23], interfacial sliding via Coulomb friction was introduced to the 3D finite element models of metal matrix composites with hexagonal array of fibers. Tensile strength of the material was calculated using the results of the analyses. The tensile strength was found to be insensitive to friction coefficient. Lane et. al. [24] showed that the interphase stiffness has an insignificant effect on stress transfer process for elastic deformation. However, it affects the process for higher strains with plastically deformed matrix. 3D finite element analyses were performed in [25] to compare the perfect and poor fiber/matrix adhesion systems in unidirectional carbon/epoxy composites with hexagonal arrangement of fibers. With increasing friction coefficient, higher SCFs were obtained. Also, good adhesion was found to lead to brittle failure while poor adhesion caused brush-like failure. Johnson et. al. [26] investigated influences of matrix cracks on stress transfer behavior of matrix by using finite element analyses. The study showed that the stress transfer mechanism is significantly affected by the presence of transverse matrix crack. Also, magnitude of the shear stress in matrix strongly depends on the crack size. Li et. al. [27] found that low and high interfacial shear sliding strengths give rise to debonding and matrix cracking, respectively. Moderate interfacial shear sliding strengths caused the opposite which results in enhanced composite strength. In [4], an experimental procedure was followed to enhance the mechanical properties of steel fiber-reinforced composites by modifying the fiber/matrix adhesion. Unidirectional and cross-ply laminates with different silane coupling agents deposited on surfaces of the fibers were produced. It was shown that higher yield strengths in both configurations were obtained by increasing the adhesion by 50%. Decreasing it by 30% has a negligible effect on the tensile yield strength, but it decreases the 90° ply strength. Swolfs et. al. [1] examined the effects of matrix cracks around fiber breaks on SCF and ineffective length using 3D finite element analyses with random fiber packings. Also, the obtained results were implemented into a strength model to observe the influence of matrix crack on cluster development and failure strain. It was shown that effects of matrix cracks on stress redistribution, cluster development and failure strain are negligible.

Different approaches were adopted for the mechanical properties of matrix material such as elastic, perfectly plastic, linearly plastic, viscoelastic etc. In [28], a parametric study with 3D finite element analyses were performed by using planar array alignment with 5 carbon fibers. SCF results were shown to depend on the applied load in the elasto-plastic matrix case. Also, this material behavior caused longer ineffective lengths and larger SCFs compared to elastic behavior which are consistent with the results of this study presented in chapter 5. Similar results were obtained from the studies in [29,30]. Fiedler et. al. [31] showed that elastic-perfectly plastic material behavior of matrix leads to significant restriction of load transfer to intact fibers. SCFs in the models with hypoelastic matrix, which exhibits nonlinear but reversible stress-strain behavior, were found to depend on the applied strain and authors interpreted this behavior of matrix to be more realistic. In [32], the effects of matrix shear yield stress on stress redistribution were investigated by using Raman spectroscopy. It was observed that no debonding between fiber and matrix was present after fiber failure for all considered matrix systems. Also, local shear yielding of matrix took place just near the broken fiber. Authors found that lower yield strength caused larger ineffective lengths, however, no conclusion could be drawn from the study for the effects of shear yield strength of matrix on SCF. In [33,34], Blassiau et. al. found that plastic behavior of matrix was shown to lead to build-up of stresses on intact fibers due to plastic deformation accumulation in matrix in the case of cyclic loading.

Considering the previous studies in the literature, it can be deduced that fiber distributions affect the SCF and ineffective length results. Landis and McMeeking [22] examined the effects of uneven fiber spacing and calculated higher stress concentrations when intact fibers got closer to the broken fiber. In [35], random fiber packings were compared with the square and hexagonal packings under transverse loading by performing finite element analyses. Random fiber packings were found to influence the results significantly, especially at high fiber volume fractions. In a similar study [36], higher stresses were obtained for random packings compared to square and hexagonal packings with the same fiber volume fraction. Also, stress concentrations were found to depend strongly on the distance between the fibers. Matsuda et. al. [37] deduced that random distribution of fibers significantly influences the microscopic behavior while it does not have a remarkable influence on the macroscopic behavior of the laminates. Swolfs et. al. [11] investigated the influences of the random fiber packing for carbon and glass/epoxy composites under longitudinal tensile loading using 3D finite element models. It was shown that due to closer fibers to the broken fiber, maximum SCFs obtained in random packings were greater than those in square and hexagonal packings. Smaller ineffective lengths were obtained due to the same reason. However, smaller SCFs for the same distances were obtained in random packings. Besides these, increasing fiber volume fraction was found to decrease the ineffective length and SCF at the same distances. Considering these results, the authors interpreted that random fiber distributions are more suitable for strength calculations because they are more realistic representations of real-life composites.

All those studies mentioned above were based on static cases. Dynamic stress concentrations were also investigated in the literature. Sakharova and Ovchinskii [38] calculated the dynamic SCFs on intact fibers near the broken fiber for break plane approximately twice as large as the SCFs in the static case. In [39], using finite element analyses, dynamic stresses caused by a fiber break in single- and multi-fiber composites were found to be significantly different from the static stresses, which consequently affects the subsequent fiber failure. Ochola et. al. [40] performed compressive tests on carbon and glass fiber-reinforced polymer laminates to examine the strain rate sensitivity of the materials. Dynamic strength of glass fiber composites was found to increase with increasing strain rate.

Time-dependent aspects were also taken into consideration. In [41], a shear lag model for metal matrix composites with long brittle fibers was used to examine the creep behavior. Effects of fiber breaks and consequential stress relaxation in broken fibers were included in the model. The results showed that ignoring stress relaxation in broken fiber causes overestimation of the creep rupture time. Iyengar and Curtin [42] observed progressive increase of the stresses on intact fibers due to the shear stress relaxation in the matrix. This causes the intact fibers to fail over time and in the end, a sudden failure of the composite takes place. In [34], it was shown that stress concentrations increase with time for viscoelastic matrix behavior and intact fibers continue to fail even when the load is unchanged. Using 3D multifiber unit cell models, fatigue behavior of carbon/glass hybrid composites were examined in [43]. It was shown that for the highest volume fraction of carbon fibers, composite has the longest lifetime under tension-tension cyclic loading while the opposite is valid for the highest volume fraction of glass fibers. The highest volume fraction of carbon fibers caused the material to show the lowest lifetime under compression-compression cyclic loading. Finally, under tension-compression cyclic loading, volume fraction of carbon fibers has a mixed effect on the lifetime of the composite.

Wisnom [44] explained that misalignments of fibers may take place during manufacturing and testing of composites, cutting out specimens and in prepreg tapes.

It was found that even a small angle between the fiber alignment and the loading axis leads to significant reduction in the compressive strength of the material. In [43], fiber misalignments were found to accelerate the damage on the fibers and to reduce the lifetime of the material.

Many other aspects were also considered in the previous studies. Ryvkin and Aboudi [45] claimed that calculations with average fiber stresses overestimate the composite strength. Therefore, they introduced point stress concentration factor concept into the calculations. In [46], effects of residual stresses due to curing of the material on the damage initiation and evolution in unidirectional polymer matrix composites were investigated under transverse loading. Residual stresses were found to be always harmful for compressive and pure shear loading. They are beneficial for tensile loading in the case of high resin strength but detrimental in the case of low resin strength. Behzadi and Jones [47] formed the stress-strain curve of the matrix material experimentally as a function of temperature. SCF results were found to decrease with increasing temperature. Statistical variability of fiber strengths were found to cause different composite strengths in [48]. Swolfs et. al. [11] showed that the carbon anisotropy resulted in larger ineffective lengths and SCFs at the same fiber distances. In [49], effects of different fiber radii and hybrid volume fractions on stress concentrations in hybrid composites with carbon and glass fibers were examined using 3D finite element models with random packings. Assuming equal fiber radius for both fibers resulted in significant differences in stress concentrations. Increasing the carbon ratio in the composite caused slight decrease in ineffective length and SCFs for both fiber types. In [14], 3D finite element models of steel fiber composites were prepared. The models were subjected to transverse tensile loadings and fibers with non-circular cross-sections were modelled. Extremely higher stress concentrations were found on the corners of polygonal cross-sections. In a similar study, Sabuncuoglu [50] introduced fillets on the corners of the polygons. Fillets on the corners significantly decreased the transverse stress concentrations but, they were still larger than the stress concentrations on the sides.

CHAPTER 3

DEVELOPMENT OF FINITE ELEMENT MODELS FOR UNIDIRECTIONAL STEEL FIBERS

3.1. Introduction

In this section, parametric creation steps of finite element models are described. The created models contain randomly distributed unidirectional steel fibers. Also, hexagonal fibers are rotated randomly around their longitudinal axes. Models are generated with finite element analysis software Abaqus® with the aid of programming language Python® that provides means for parametric modelling. With the aid of Python® scripts, creation time of finite element models is significantly reduced and by changing a model parameter in a single line, a different model is generated automatically. The scripts were obtained by modifying the script used in [1] and implementing the scripts developed in [14]. Creation of geometric model, meshing, material properties, boundary conditions and acquisition of the results are given in detail in this section.

3.2. Parametric Modelling Methodology

By applying the parametric modelling methodology with the aid of Python® script, finite element models completely get ready for the analysis. The final geometry is a cylindrical model with a diameter and length of 24 times and 120 times fiber radius (r_f), respectively, where fibers are randomly distributed in matrix.

3.2.1. Modelling of Square Representative Volume Element

At the beginning of the modelling, a 3-dimensional square representative volume element (RVE) is created before obtaining the final cylindrical geometry, whose dimensions depend on the radius of the fibers as fiber radius may vary depending on its material; carbon, glass or steel [14]. Width of square RVE is chosen to be greater than the diameter of final cylindrical geometry so that fibers are properly positioned in the model before the fibers on the edge are cut longitudinally. The dimensions of the square RVE is shown in Figure 3.1.

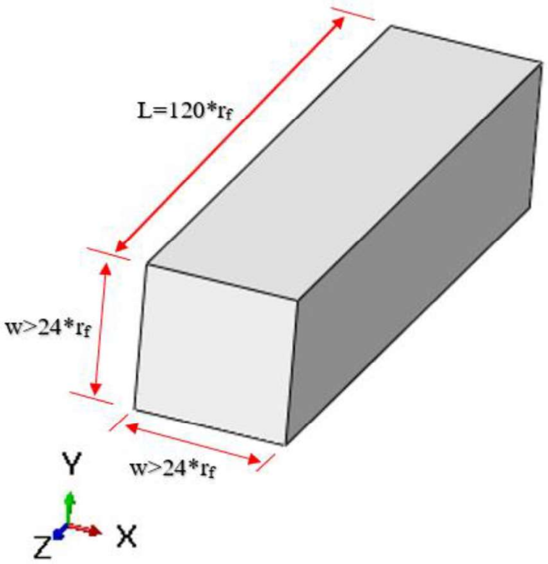

Figure 3.1. Square RVE with its dimensions.

3.2.2. Modelling of Fibers

After creating the 3-dimensional square RVE, fibers are positioned in the model by partitioning the geometry. Many strength models in literature ignore fiber-matrix interfacial debonding and also, observations of interfacial debonding do not exist for composites with thousands or millions of fibers [9]. Therefore, perfect fiber-matrix interfacial bonding is assumed in finite element models which is performed by modelling the fibers and matrix to share the nodes at interfaces. Cracks and voids can be present in steel fibers as well as other fiber types. As mentioned in [9], since there is no available Weibull strength distribution in this scale, cracks and voids are ignored in the strength models. In this work, it is assumed that there is no cracks and voids in the materials. This thesis work includes two different cross-sectional fiber shapes, circular and hexagonal, whose modelling implementations differ from each other at some steps. Firstly, before preparing finite element models, 2-dimensional random fiber coordinates are generated using the Matlab®-based algorithm presented in Melro et. al. [51]. The algorithm is used to create 2-dimensional fiber packings with a high degree of randomness by using three input parameters; fiber radius, fiber volume fraction and size of RVE and writes the coordinates of these randomly generated fibers into a file. The algorithm is slightly modified in this study. The minimum distance criteria between fiber centers are changed from 2-times fiber radius to a randomly generated number between 2 and 2.1-times fiber radius. This change is performed to increase the similarity of statistical descriptors between generated and real fiber distributions [52]. After the coordinates of fiber centers are written to a file according to the desired inputs, the Python® script in Abaqus® reads them and draws circles with a pre-defined fiber radius on either top or bottom plane of 3-dimensional square RVE. After that, these circles are used to extrude the fibers in longitudinal direction (z). In Figure 3.2, randomly distributed, circular cross-sectional fibers in square RVE for 60% and 30% fiber volume fractions (V_f) are presented. Note that these fractions are valid for cylindrical RVEs. In fiber coordinate generator algorithm, fibers are placed to the entire square RVE which meets the desired volume fractions. However, the Python® script excludes the fibers outside the diameter of $24 * r_f$ during creation of finite element models. Due to this reason, there is no fiber on the corners of square RVEs in Figure 3.2.

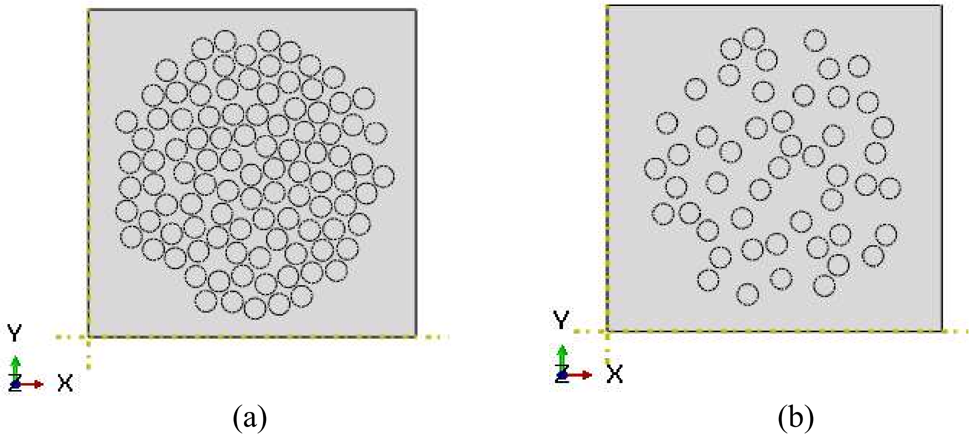

(a) (b)

Figure 3.2. Randomly distributed fibers with circular cross-section in square RVE for V_f of: (a) 60%, and (b) 30%.

Fibers with hexagonal cross-section require more effort to maintain randomness while positioning them in RVE. Unlike fibers with circular cross-section, hexagonal fibers have no radius due to their cornered shape. Therefore, dimensions of hexagonal fibers were determined according to approximate diameter of steel fibers of circular shape to have the same cross-sectional area [14]. Steel fiber radius is taken as 15 µm, which is the common value for steel fibers [14]. Considering the equality of circular and hexagonal shapes' areas, the distance between center of regular hexagon and its corner, R_h, is calculated with respect to radius of the circle, R, by the following equation:

$$R_h = \sqrt{\frac{2\sqrt{3} * \pi * R^2}{9}} \qquad \text{(Eq. 3.1)}$$

The random fiber coordinate generator algorithm has been created with respect to circular-shaped fibers. Therefore, for hexagonal-shaped fibers, there is a possibility for hexagons to overlap with each other due to their cornered shapes if the minimum distances between fiber centers are set considering the radius of circles as it is presented in Figure 3.3.

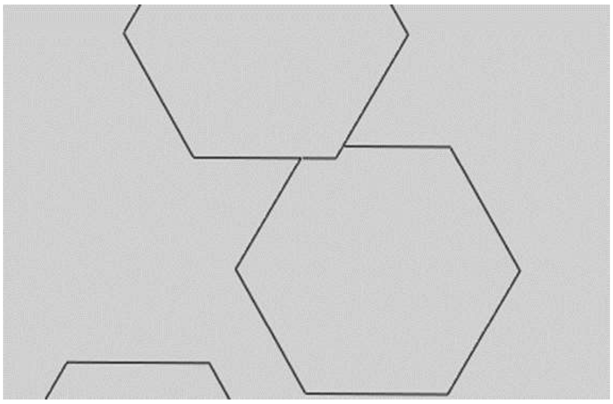

Figure 3.3. Overlapping fibers due to hexagonal shape

To prevent such overlapping of hexagonal-shaped fibers, minimum distance parameter in the random coordinate generator algorithm is re-set with respect to distance between center of hexagon and one of its corners as shown in Figure 3.4. This modification prevents the possibility of overlapping of hexagonal-shaped fibers with a drawback of obtaining lower maximum V_f (60%) compared to the maximum V_f (70% obtained by circular shaped fibers).

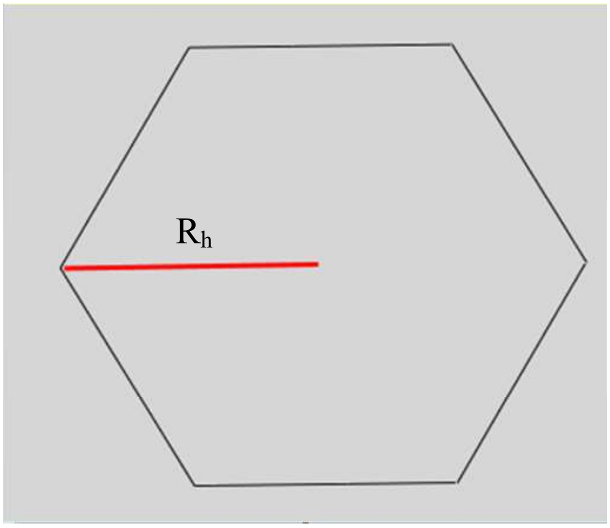

Figure 3.4. Distance between hexagonal fiber center and corner.

The rotations of fibers in the x-y plane were not considered in the original algorithm. In the case for the polygonal shaped fibers, the rotation of fibers should be considered as the location of the corners and polygonal sides can affect the distribution and the results. In this study, the individual rotations of fibers around their longitudinal axes are assigned randomly as well as their location. To accomplish this, “rand” command in Matlab® is used. Random numbers between 0 and 1 are assigned for each fiber.

The rotation possibility of 0 to π/3 radians is considered instead of 0 to 2π radians. The first reason is that the fibers return to the same orientation after the rotation of π/3 radians. The second reason is that multiplying by π/3 instead of 2π provides easiness in scripting for random orientations. Thus, in Python® script, the numbers generated by “rand” command are multiplied by π/3 radians for each fiber providing the modelling of randomly rotated fibers around their longitudinal axes in addition to their random locations. In Figure 3.5, randomly distributed and rotated fibers with hexagonal cross-section in square RVE for 60% and 30% fiber volume fractions (V_f) are presented.

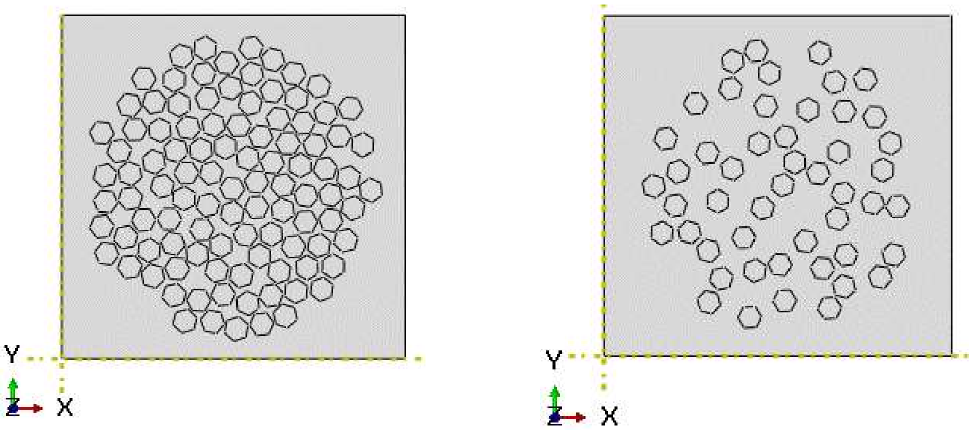

(a) (b)

Figure 3.5. Randomly distributed and rotated fibers with hexagonal cross-section in square RVE for V_f of: (a) 60%, and (b) 30%.

3.2.3. Creating Cylindrical RVE

After modelling the fiber geometries, square RVE is cut longitudinally to get the final cylindrical geometry. The fiber break is located on the bottom plane where $z = 0$. As it is mentioned in section 3.2, final geometry has $24 * r_f$ of diameter and $120 * r_f$ of length. 24 times fiber radius model diameter is large enough for stresses around broken fiber to be not affected by model size [11]. Also, 120 times fiber radius model length is considered large enough for stress results on top plane to avoid the effect of fiber break [1]. These final cylindrical geometrical models with circular- and hexagonal-shaped fibers for 60% RVE are presented in Figure 3.6 and Figure 3.7, respectively. It can be noticed that partially cut fibers on cylindrical RVE borders exist in models to preserve V_f. The broken fiber is positioned exactly at the center of final cylindrical geometry due to the Python® script.

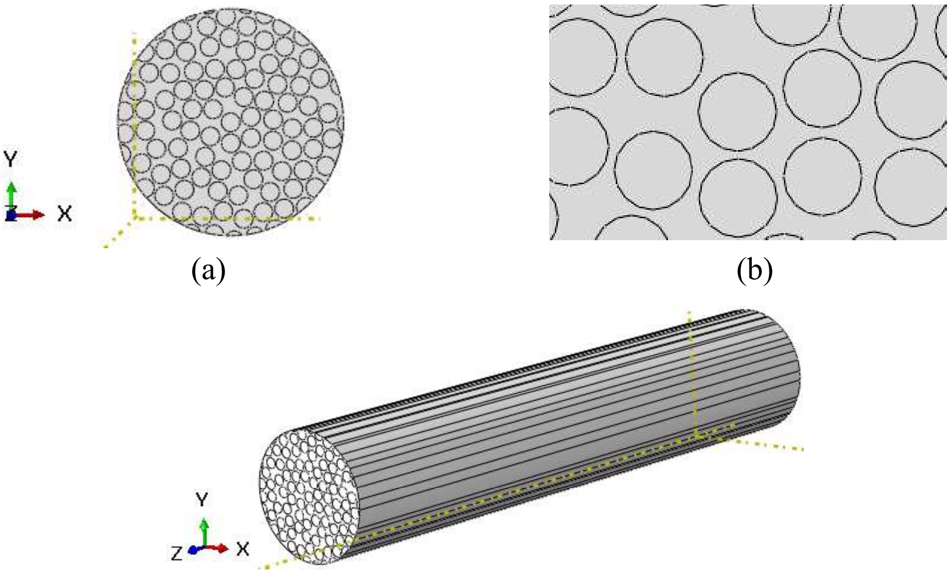

(a) (b)

(c)

Figure 3.6. Final cylindrical model with circular-shaped fibers for 60% RVE: (a) top view, (b) zoomed view, and (c) isometric view.

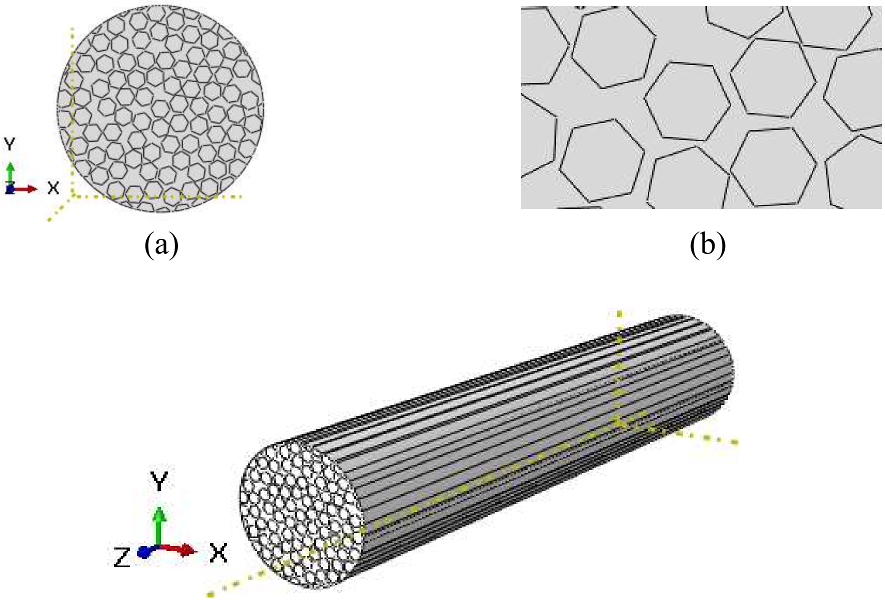

(a) (b)

(c)

Figure 3.7. Final cylindrical model with hexagonal-shaped fibers for 60% RVE: (a) top view, (b) zoomed view, and (c) isometric view.

3.2.4. Seeding and Meshing of Models

While carrying out the seeding process, it is aimed to obtain finer mesh in the vicinity of broken fiber and break plane as they are the most critical regions in the entire model. Seeding process (defining the location of the element borders) starts with adding extra circular partitions, having both slightly larger and smaller diameters than the fibers, on the borders of the broken fiber for circular-shaped fibers. For hexagonal-shaped fibers, these are extra hexagonal partitions, both larger and smaller than the fiber. These partitions provide finer mesh on the borders of the broken fiber and are also needed for implementation of the boundary conditions which will be clarified in detail in section 3.2.6. These partitions are shown in Figure 3.8.

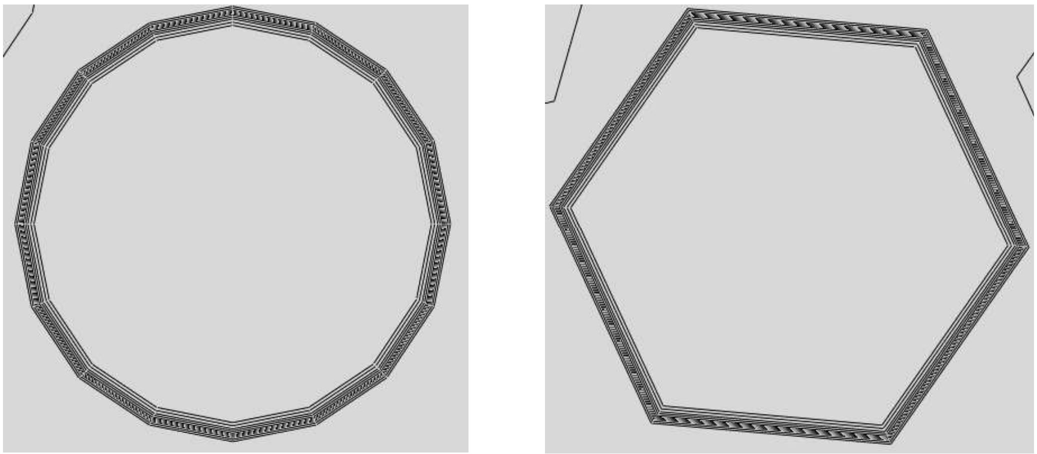

(a) (b)

Figure 3.8. Finer mesh on broken fiber borders for: (a) circular fibers, and (b) hexagonal fibers.

Seeding process continues with partitioning the fiber faces radially. For models with circular-shaped fibers, broken fiber and the closest fibers to center are partitioned with 12 equally-spaced radial lines while the rest with 8. For models with hexagonal-shaped fibers, regardless of the positions of fibers, all fibers are partitioned by drawing lines from fiber center to each fiber corner if both points are in circular RVE. These are presented in Figure 3.9.

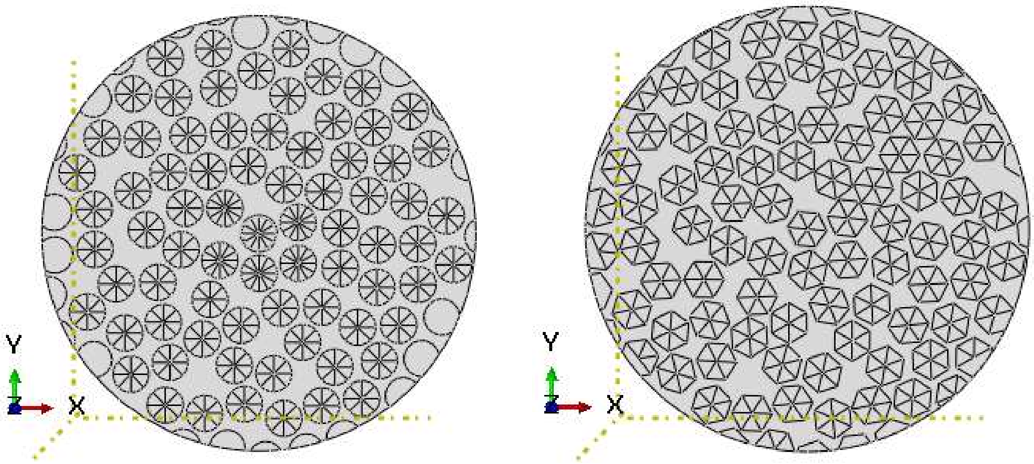

(a) (b)

Figure 3.9. Angle partition of fiber faces for: (a) circular-shaped fibers, and (b) hexagonal-shaped fibers.

After creating the lines on borders of broken fiber and inside all fibers, seeding of those lines are performed. In the entire model, the element sizes are set to be relatively smaller for fibers close to center of the model. In a single fiber, bias method is applied for the seeding of radial lines. This method applies the seeding non-uniformly by using the specified number of elements and size ratio as inputs [53]. Element sizes get smaller towards the fiber borders to get finer mesh on those regions. Seeding of circumferential lines on fiber borders is performed uniformly. Bias method is not applied, and lines are equally divided for each fiber. Some parts of the finite element models are shown in Figure 3.10 to present the seeding of circumferential lines on borders and radial lines.

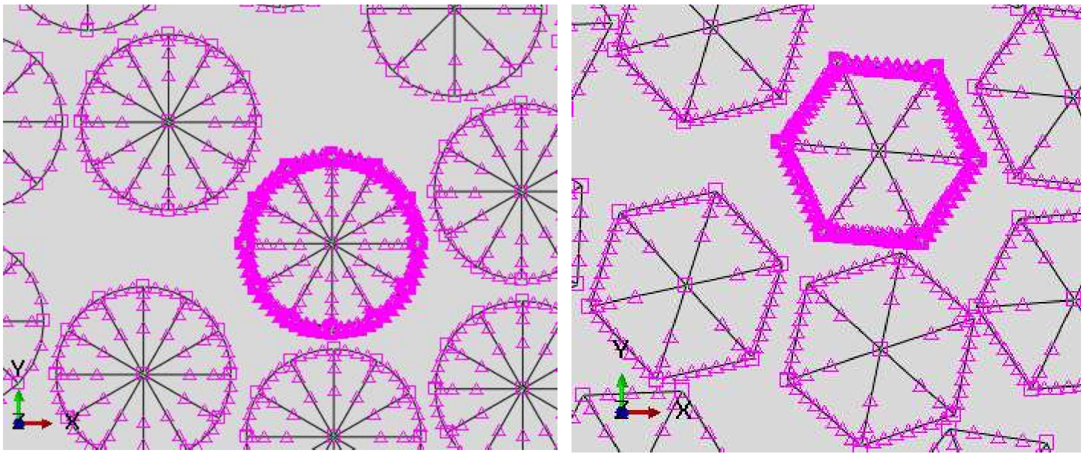

(a) (b)

Figure 3.10. Seeding of lines on borders and inside of fibers for: (a) circular-shaped fibers, and (b) hexagonal-shaped fibers.

Last parts of seeding process are the seeding along fiber direction (thickness) and global seeding. Seeding along fiber direction is performed by using bias method to get finer mesh towards break plane similar to the model in [1] (Figure 3.11). The model is divided into 25 nonuniform planes longitudinally.

Figure 3.11. Seeding along fiber direction by using bias method.

Mesh convergence analyses are performed to choose optimum element sizes which are varied only in radial direction (x-y plane). Three different meshing types are shown in Figure 3.12 and their corresponding number of elements and nodes are presented in

Table *3.1*. All finite element models consist of hexagonal-shaped fibers with 60% V_f. Both steel and epoxy are defined with elastic material properties. 0.1% strain is applied to all models.

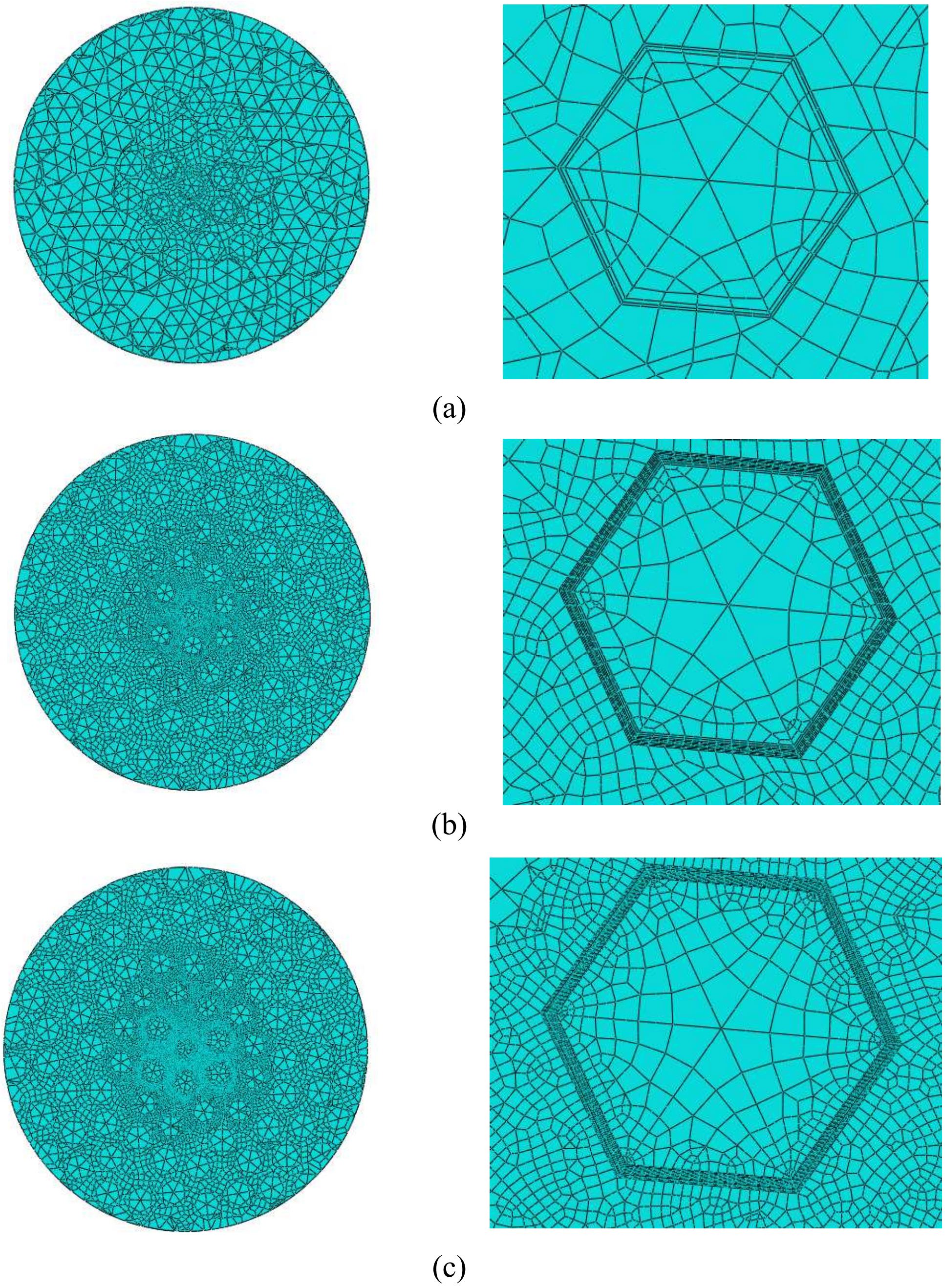
(a)

(b)

(c)

Figure 3.12. Mesh distributions with different element sizes: (a) coarse elements, (b) middle-sized elements, and (c) fine elements.

Table 3.1. *Number of elements and nodes for three different element sizes.*

Element Size	*Number of elements*	*Number of nodes*
Coarse	46475	160420
Middle	160250	619625
Fine	294850	1156775

Maximum SCF results of the closest intact fibers to the broken fiber and ineffective lengths of broken fibers are examined for comparison. The maximum difference is found as 6.7% between the models with coarse and middle-sized elements. This number is 0.4% for the models with middle-sized and fine elements. Since using finer element sizes than the middle-size costs more computational time and memory without changing accuracy of the results remarkably, middle-sized elements are used for the rest of the analyses. Reduced integration elements are used during meshing. Number of elements and nodes, element types and their numbers for circular- and hexagonal-shaped fiber models with 60% V_f are presented in Table *3.2*. All finite element analyses are executed with these corresponding meshing types regardless of parameter changes other than fiber volume fraction. Same information is presented in Table *3.3* for 30% V_f. Figure 3.13 and Figure 3.14 show 2-dimensional mesh distributions of circular- and hexagonal-shaped fiber models with 60% and 30% V_f, respectively.

Table 3.2. *Element types, number of elements and nodes for circular- and hexagonal-shaped fiber models with 60%* V_f.

Fiber Shape	**Element Type**	***Number of Nodes***	***Number of Elements***
Circular	C3D20R	-	114875
	C3D15	-	35875
	Total	569474	150750
Hexagonal	C3D20R	-	131300
	C3D15	-	28950
	Total	619625	160250

Table 3.3. *Element types, number of elements and nodes for circular- and hexagonal-shaped fiber models with 30%* V_f.

Fiber Shape	**Element Type**	***Number of Nodes***	***Number of Elements***
Circular	C3D20R	-	136975
	C3D15	-	19725
	Total	618397	156700
Hexagonal	C3D20R	-	148500
	C3D15	-	16250
	Total	657107	164750

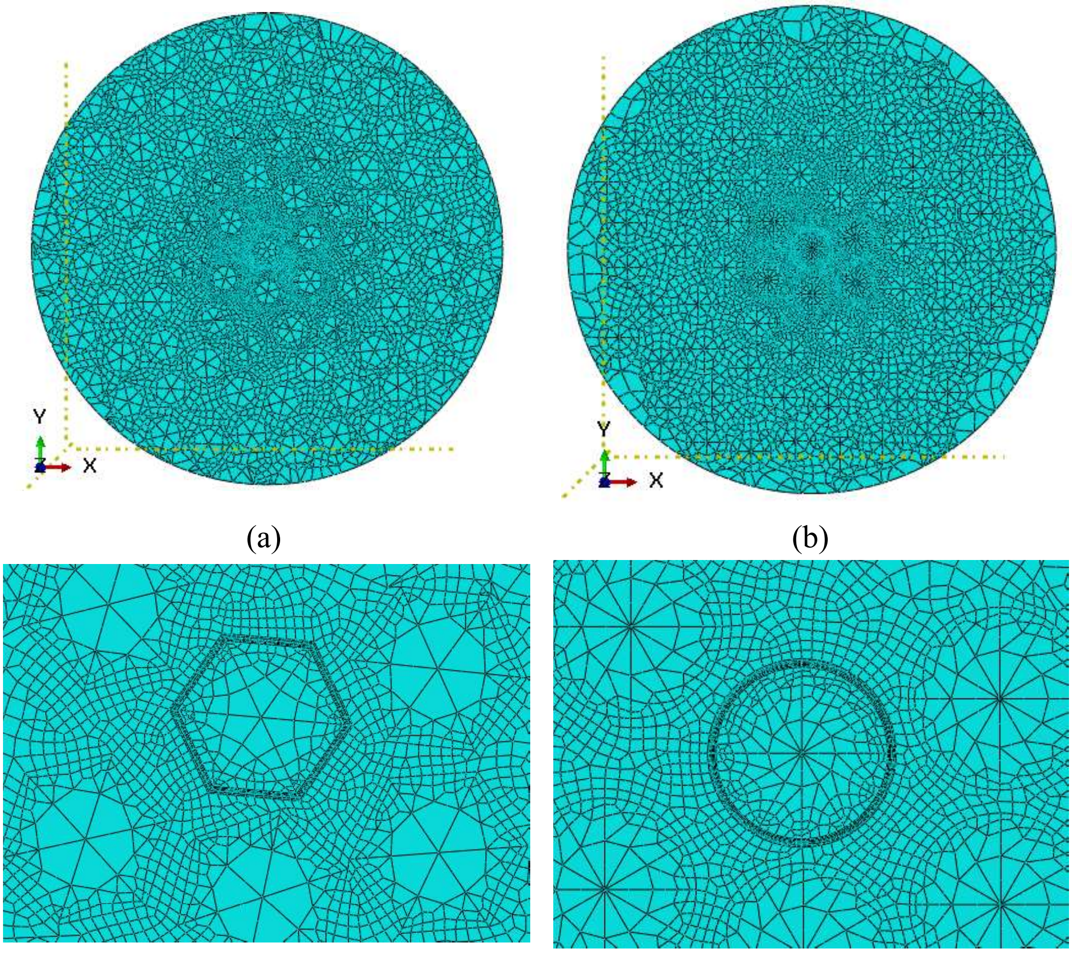

(a) (b)

(c) (d)

Figure 3.13. 2-dimensional mesh distributions of models for 60% V_f with: (a) hexagonal-shaped fibers, (b) circular-shaped fibers, (c) zoomed view of hexagonal-shaped fibers, and (d) zoomed view of circular-shaped fibers.

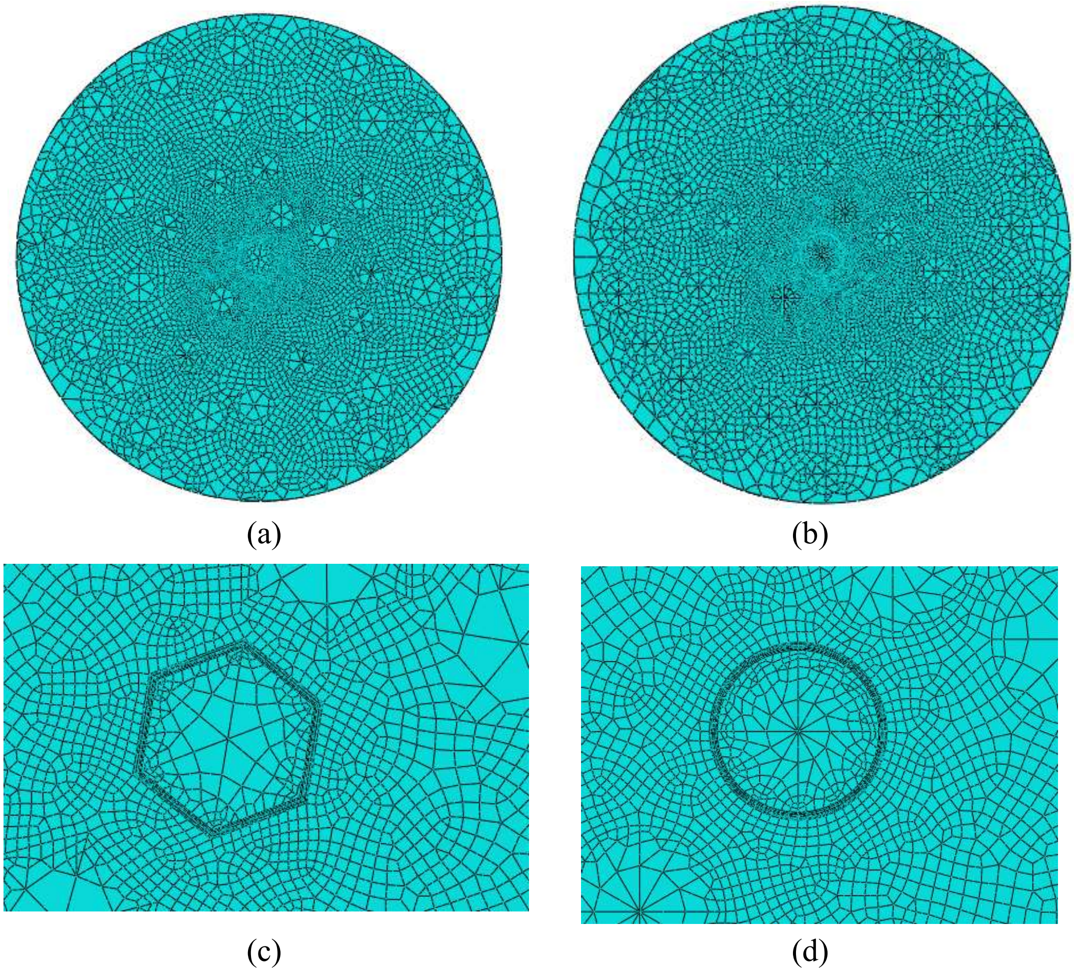
(a) (b)
(c) (d)

Figure 3.14. 2-dimensional mesh distributions of models for 30% V_f with: (a) hexagonal-shaped fibers, (b) circular-shaped fibers, (c) zoomed view of hexagonal-shaped fibers, and (d) zoomed view of circular-shaped fibers.

3.2.5. Material Properties

The modelling script assigns steel material properties to corresponding fiber regions using the fiber coordinates, their geometrical shape and dimension information. Then, epoxy material properties are assigned to the rest of the regions as matrix. Either elastic or elastoplastic material behavior is defined depending on the type of analysis. Elastic properties of epoxy and steel are shown on Table *3.4* [6,11]. True stress – true strain plots of epoxy and steel are presented in Figure 3.15 and Figure 3.16, respectively [6,54].

Table 3.4. *Elastic material properties of epoxy and steel.*

Material	*Stiffness, E [GPa]*	*Poisson's Ratio, v*
Epoxy	3	0.4
Steel	193	0.3

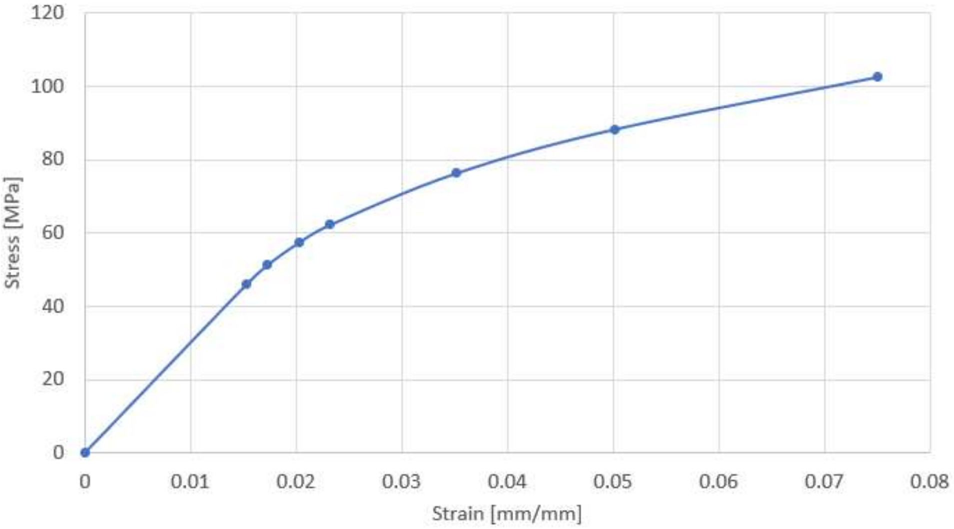

Figure 3.15. True stress - strain curve of epoxy

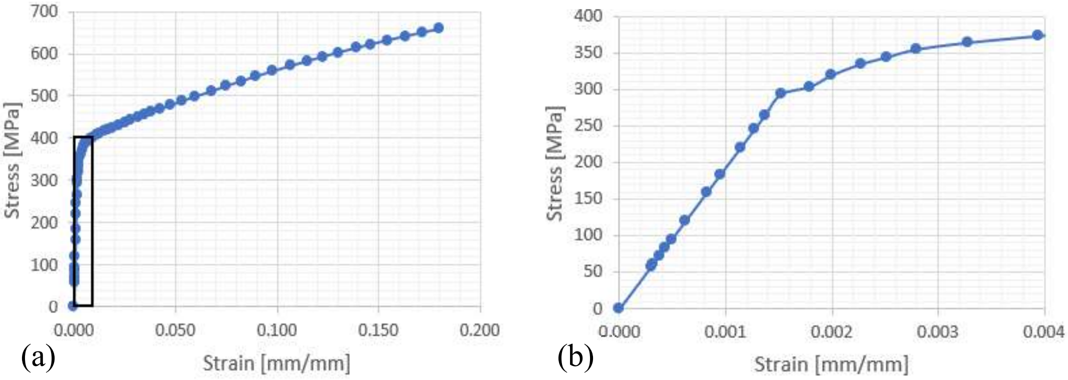

Figure 3.16. True stress - strain curve of steel: (a) entire curve, and (b) zoomed view up to 0.4% strain.

Elastic region is defined in the software with Young's modulus and Poisson's ratio. During plastic region modelling, isotropic hardening and von Mises yield criterion are defined and plastic strains instead of total strains are defined in the program with their corresponding stress values. These plastic strains are calculated by using the equation (3.2). Material property assignments of corresponding regions are presented in Figure 3.17.

$$\varepsilon_p = \varepsilon_{total} - \frac{\sigma}{E} \tag{Eq. 3.2}$$

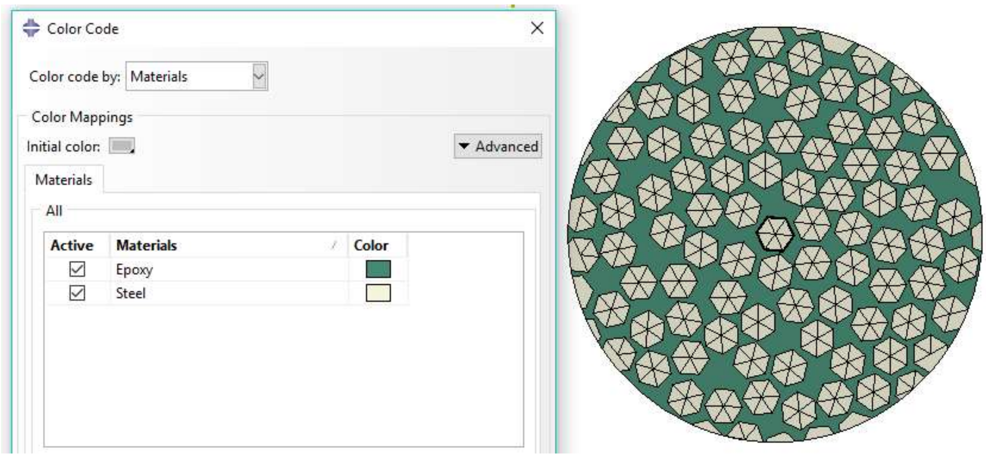

Color code by: Materials

Active	Materials	Color
☑	Epoxy	🟩
☑	Steel	⬜

Figure 3.17. Assignment of materials to corresponding regions.

3.2.6. Boundary Conditions

In this step of finite element modelling, boundary conditions are created. Displacement is applied as the loading type. Knowing the model length (L), a desired strain input (ε) is given by applying the corresponding displacement value (δ). In this study, a set of boundary conditions, used in [23] to represent a broken fiber in a composite, is applied with a modification described in [1], i.e. improved strategy. Displacement is applied to the entire top plane where coarse mesh along fiber direction is available. Fiber break exists on the bottom plane. Top plane boundary conditions are shown in Figure 3.18.

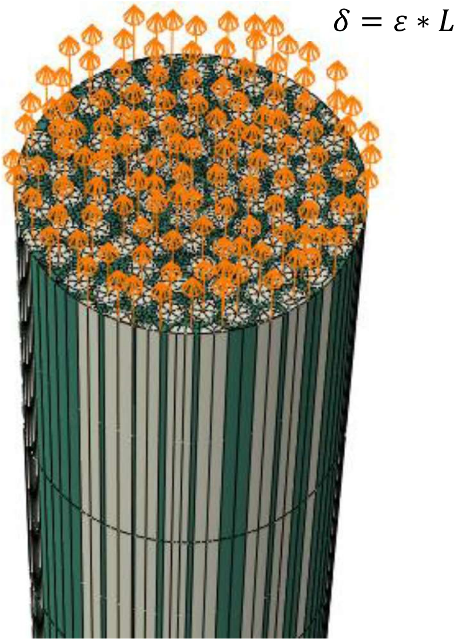

Figure 3.18. Top plane boundary conditions.

Symmetric boundary conditions are applied to the entire bottom plane except the fiber in the middle, which represents the broken fiber. Note that the broken fiber is positioned in the middle of the model for stresses around broken fiber to be not affected by edge effect. There are two strategies explained in [1] to apply symmetric boundary conditions: baseline and improved strategies. In baseline strategy, symmetric boundary conditions are applied to the nodes at the perimeter of the broken fiber. In improved strategy, these nodes are released, and the boundary condition is applied to the nodes just near them which represents a tiny matrix crack, i.e. $0.005 * r_f$, surrounding the fiber on the bottom plane. In [1], it was shown that baseline strategy led to rapid stress build-up to 45% within the first layer of elements of broken fiber which is not a realistic representation of a fiber break. The reason for this situation is the constraint on the nodes at the perimeter of broken fiber. The elements on the borders of broken fiber are stretched and stress build-up takes place on those elements. In improved strategy, which is suggested to be a more accurate one [1], that constraint is shifted to the nodes just near to the nodes at the perimeter of broken fiber which prevents rapid stress build-up on broken fiber elements. Bottom plane boundary conditions and a zoomed view to broken fiber borders are presented in Figure 3.19. Green and white regions represent matrix and fibers, respectively. As presented in Figure 3.19b, symmetric boundary conditions are not applied on the nodes at the perimeter of the broken fiber, instead, it is applied to the nodes just near them. Also, lateral cylindrical surface is traction free.

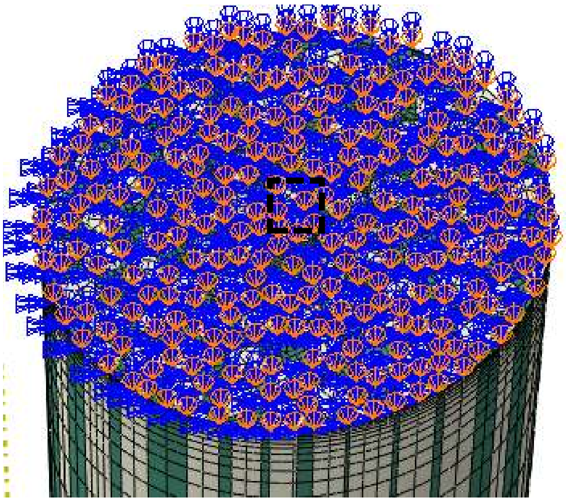

(a)

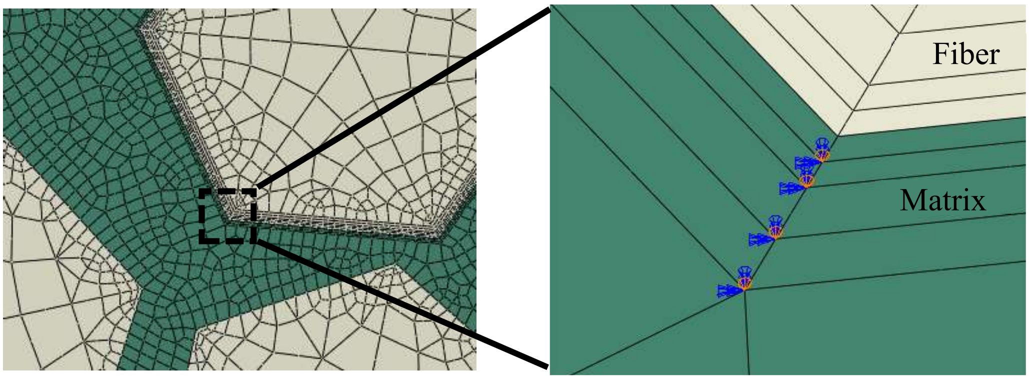

(b)

Figure 3.19. Bottom plane boundary conditions: (a) entire surface, and (b) broken fiber borders.

3.2.7. Analysis Parameters

In this section, step, field outputs and job are created in the finite element models. Only static analyses are executed and depending on the type of analysis, several steps can be defined in the software. For solely loading analyses, there is only one step created. This number is increased if there is a need for extra analyses, such as loading the part followed by the unloading process which can also be followed by reloading process. Field outputs and their explanations are given in Table *3.5* [53]. Job is created at this point and its properties are set according to the computer by which the finite element analysis is performed.

Table 3.5. *Field outputs and their explanations.*

Field Output	*Explanation*
S	All stress components
PE	All plastic strain components
PEEQ	Equivalent plastic strain
PEMAG	Plastic strain magnitude
LE	All logarithmic strain components
U	All physical displacement components
RF	All components of reaction forces
CF	All components of point loads
CSTRESS	Contact pressure and frictional shear stresses
CDISP	Contact opening and relative tangential motions
SVOL	Integrated section volume
EVOL	Current element volume
IVOL	Integration point volume
COORD	Coordinates of the integration point for solid elements and rebar

3.3. Acquisition of the Results

Stress concentration factors on intact fibers and ineffective length of broken fiber are the main results to obtain in this work. Since the models are for unidirectional fiber-reinforced composites, SCF and ineffective length are calculated with respect to stress components along fiber direction, $S11$. At the end of the result acquisition process, total number of 4 files is obtained. 2 of them include average cross-sectional SCF results while the other 2 include peak SCF results. To get these results easily and in significantly less time, Python® script, developed in [11] to extract the results, is used instead of recording them manually. With the aid of this Python® script, 2 results files are obtained. The first one includes SCF results of each fiber for each layer of elements. From SCF results of broken fiber in this file, ineffective length is obtained. In the second one, maximum SCF value along the fiber direction for each fiber with their lateral distance to broken fiber are recorded. These two files are created with respect to cross-sectional average fiber stresses. Also, with some modifications on the script, both files are also created for peak fiber stresses causing 4 files in total in the end.

During calculation of cross-sectional average SCFs, stress values on each Gaussian point of each element are multiplied by their corresponding integration point volume, IVOL, and the values on same layer are sum-up for each fiber separately. These summations of each layer for each fiber are divided by their corresponding integration point volume summations. As a result, cross-sectional average stress values on each layer of each fiber are recorded. By applying the SCF formula given in chapter 1, SCFs are obtained from these values and the first two files related to cross-sectional average SCFs are created. Similar procedure is applied to obtain peak stress results. Maximum Gaussian point stresses on each layer of each fiber are picked and recorded. SCF formula is applied to these values and the other two files related to peak stresses are created.

3.4. Verification of the Developed Finite Element Models

In this section, accuracy of the developed finite element models is verified. It is performed by comparing the results of the developed code with the stress recovery profile of broken fiber, and the maximum SCFs in intact fibers, obtained for improved strategy in Swolfs et. al. [1]. The developed codes generate the finite element models similar to the original code in general. Firstly, the modified code which generates finite element models with hexagonal-shaped fibers was created. Due to the different cross-sectional shapes of fibers, modelling of fibers for original and modified scripts differ from each other with the usage of different commands and algorithms. Also, there is an extra algorithm in modified script for random rotations of individual fibers around their longitudinal axes. Differences in the seeding process are the partition of fiber faces and extra partitions on fiber borders. Elasto-plastic properties of fiber material are defined in the modified script and lastly, some portions of the original script related to matrix cracks and multiple fiber cracks are not used in modified script as they are unneeded in this study. The modified script which generates finite element models with circular-shaped fibers is more similar to the original script due to the same fiber shape. It is created from the first modified script by only changing the algorithms related to fiber shapes. For verification of modified scripts, the same random fiber distribution with circular cross-sectional fibers in [1] is used to generate the finite element models. Random fiber distribution with 50% V_f is shown in Figure 3.20.

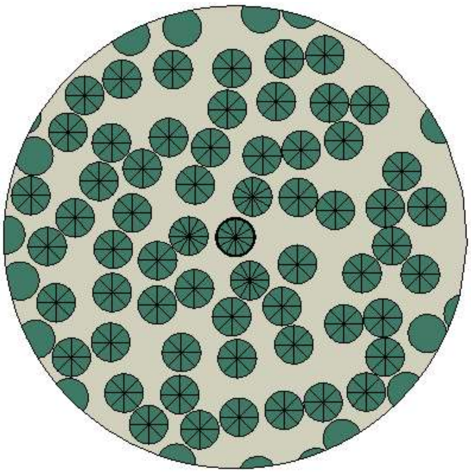

Figure 3.20. Random fiber distribution of circular cross-sectional fibers with 50% V_f for verification study.

Carbon fibers are modelled with 3.5 μm fiber radius [11]. Diameter and length of the RVE are $24 * r_f$ and $120 * r_f$, respectively. Linear elastic, transversely isotropic carbon properties are assigned as the fiber material given in *Table 3.6* [11]. Elastoplastic properties of epoxy are defined as matrix material, whose material properties were given in *Table 3.4* and in Figure 3.15.

Table 3.6. *Linear elastic material properties of transversely isotropic carbon.*

Property	*Value*
E_{11} [GPa]	230
E_{22} [GPa]	15
E_{33} [GPa]	15
ν_{12}	0.25
ν_{13}	0.25
ν_{23}	0.25
G_{12} [GPa]	13.7
G_{13} [GPa]	13.7
G_{23} [GPa]	6

Displacement corresponding to 2% strain is applied to the entire top plane. Symmetric boundary conditions are applied to bottom plane except the middle fiber, i.e. broken fiber, as explained in detail in section 3.2.6. When elasto-plastic material properties are defined for at least one material in the finite element model, due to the nonlinearity in stress-strain curve, different SCF results are obtained for different strain inputs in case the elastic limit of one of the materials is reached [9]. Despite these differences, calculating SCFs at a strain close to failure strain of the composite gives accurate results [9]. Therefore, displacement corresponding to 2% strain is applied as an input in [1]. Properties of the verification model are given in *Table 3.7*.

Table 3.7. *Properties of the verification model*

Property	*Value*
V_f [%]	50
Applied strain [%]	2
r_f [μm]	3.5
Diameter of RVE	$24 * r_f$
Length of RVE	$120 * r_f$
Number of elements	120075
Number of nodes	449176

Figure 3.21 and Figure 3.22 present the stress recovery profiles of broken fibers and maximum cross-sectional average SCF results of intact fibers, respectively, for both models created by original and modified scripts. Descriptions of z/R and d/R ratios for stress recovery profile and SCF graphs, respectively, are given in Figure 3.23.

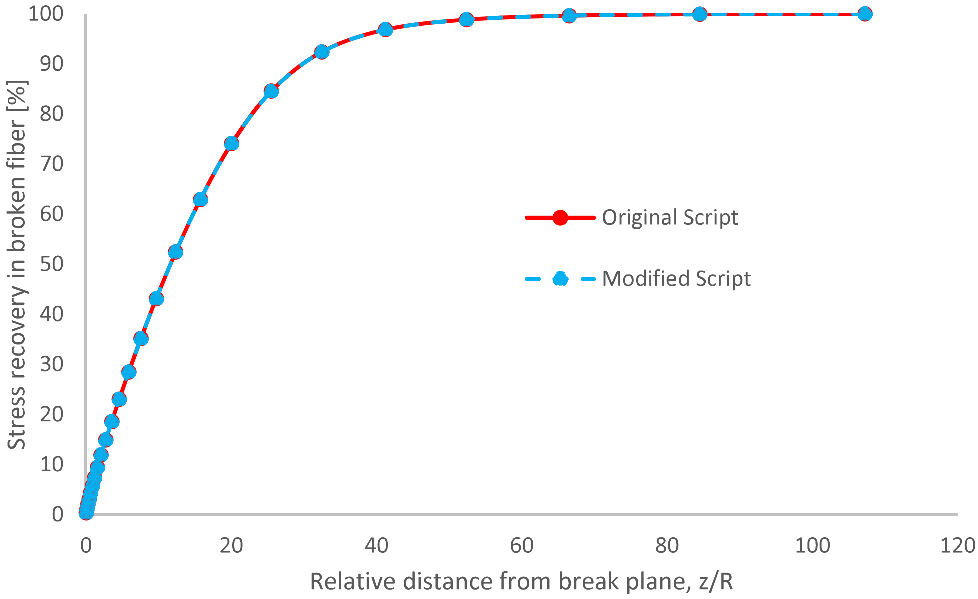

Figure 3.21. Stress recovery profiles of broken fibers for models of both original and modified scripts.

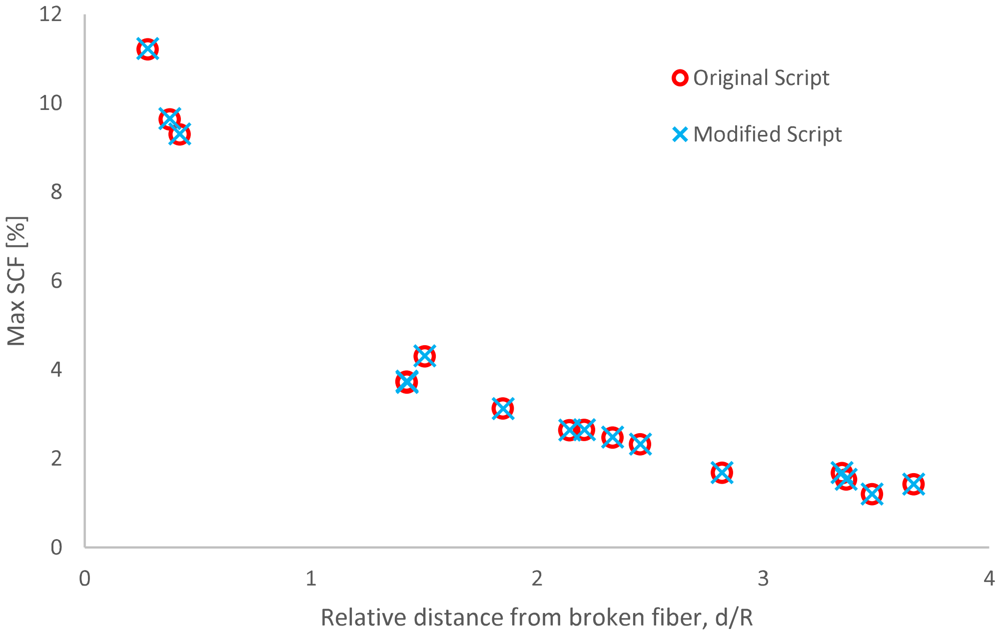

Figure 3.22. Maximum cross-sectional average SCF results of intact fibers for models of both original and modified scripts.

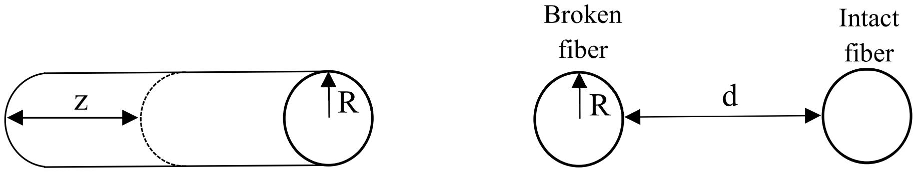

(a) (b)

Figure 3.23. Descriptions of ratios existing in stress recovery profile and SCF graphs: (a) z/R, and (b) d/R.

Considering Figure 3.21 and Figure 3.22, it can be seen that stress recovery profiles of broken fibers and maximum cross-sectional average SCF results of intact fibers are the same for both finite element models created by original and modified scripts. Therefore, accuracy of the developed finite element models created by modified scripts is assured by obtaining the same results with respect to figures 2 and 3 for improved strategy in [1].

CHAPTER 4

EFFECTS OF CROSS-SECTIONAL FIBER SHAPE ON SCF AND INEFFECTIVE LENGTH

In this chapter, effects of cross-sectional fiber shape on SCF and ineffective length with respect to cross-sectional average and peak fiber stresses are investigated. This is performed by analyzing the results of the finite element models with circular- and hexagonal-shaped fibers which have the same properties including the fiber locations. The cross-sectional average and the peak stress results are investigated with the finite element models including elastic and elasto-plastic matrix material properties.

4.1. Analyzed Model Types

The model types and the properties are presented in Table 4.1. Total 8 different finite element models with 60% and 30% V_f were prepared. In the first 4 models, both fiber and matrix are defined with elastic properties while the matrix material of the other models is defined with elasto-plastic properties given in *Table 3.4* and Figure 3.15, respectively.

Table 4.1. *Properties of finite element models for cross-sectional fiber shape comparison.*

Model No.	***Model 1***	***Model 2***	***Model 3***	***Model 4***
V_f [%]	60	60	30	30
Fiber cross-section	Hexagonal	Circular	Hexagonal	Circular
Fiber material property	Elastic	Elastic	Elastic	Elastic
Matrix material property	Elastic	Elastic	Elastic	Elastic
Applied strain [%]	0.1	0.1	0.1	0.1
Model No.	***Model 5***	***Model 6***	***Model 7***	***Model 8***
V_f [%]	60	60	30	30
Fiber cross-section	Hexagonal	Circular	Hexagonal	Circular
Fiber material property	Elastic	Elastic	Elastic	Elastic
Matrix material property	Elastoplastic	Elastoplastic	Elastoplastic	Elastoplastic
Applied strain [%]	2	2	2	2

4.2. Analysis of Cross-Sectional Average Fiber Stresses

4.2.1. Cases with Elastic Matrix Material Properties

In elastic cases, 0.1% strain input is applied. Apart from 0.1% strain, other strain values give the same results because of the linearity in stress-strain curves of both materials. The stress recovery profiles of broken fibers and maximum cross-sectional average SCF results of intact fibers for 60% and 30% V_f are presented in Figure 4.1, Figure 4.2, Figure 4.3 and Figure 4.4, respectively. SCFs are calculated with respect to average stress value through the stress field for each plane along fiber direction and in SCF graphs, maximum values among these planes for each intact fiber are presented.

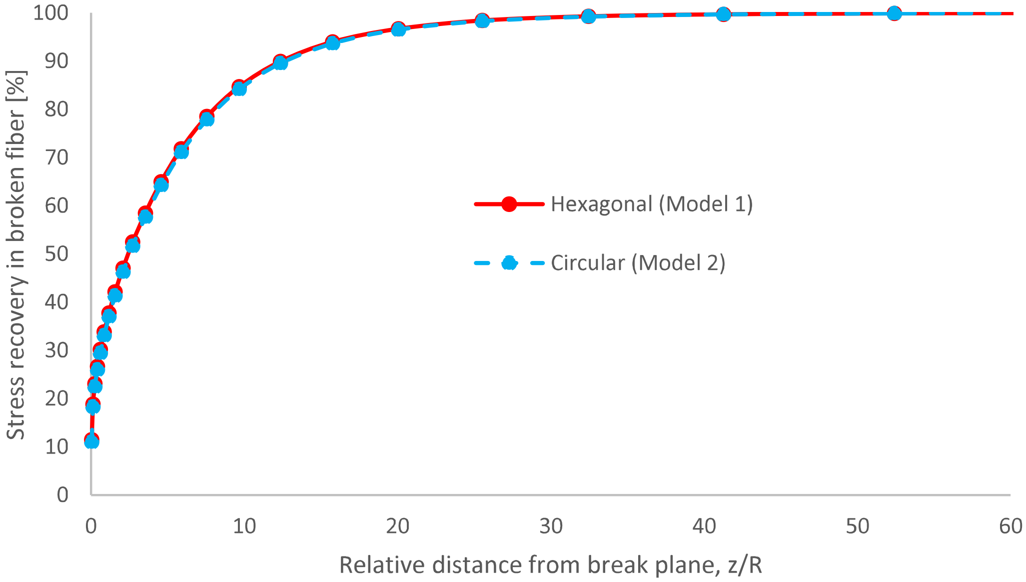

Figure 4.1. Stress recovery profiles of broken fibers for elastic cases with 60% V_f.

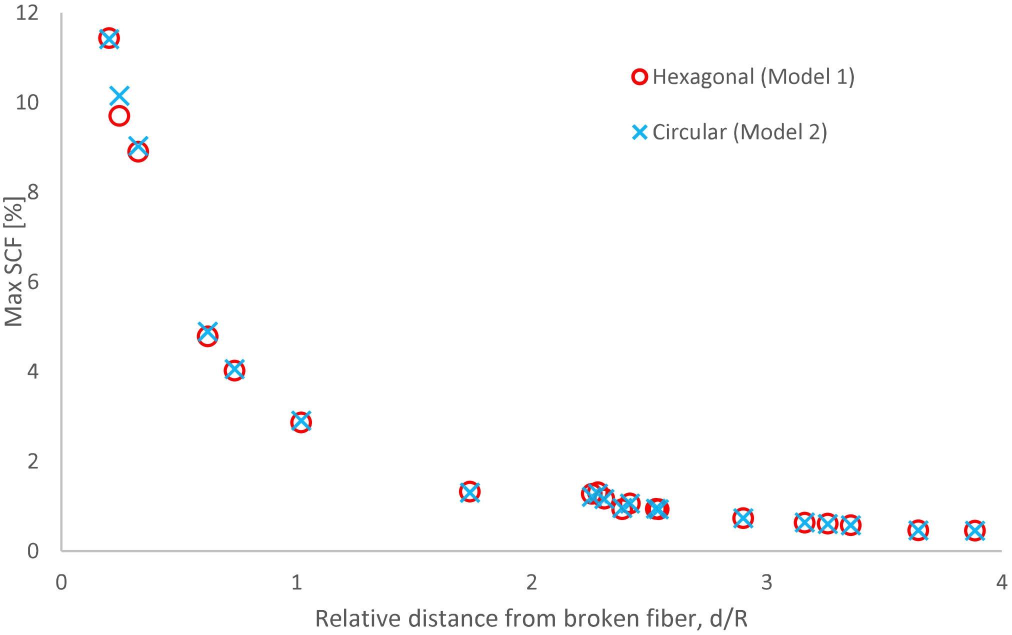

Figure 4.2. Maximum cross-sectional average SCF results for elastic cases with 60% V_f.

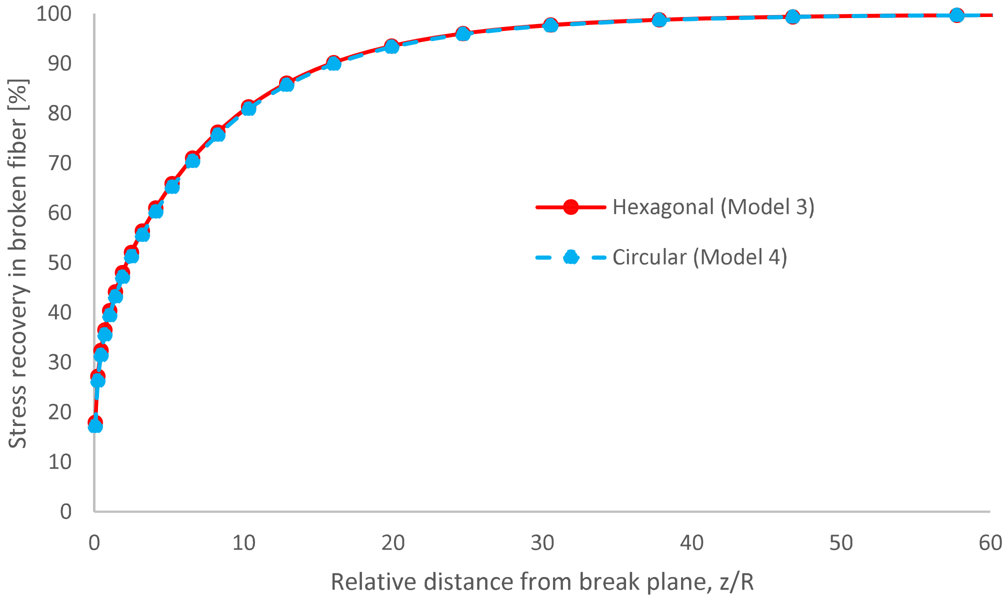

Figure 4.3. Stress recovery profiles of broken fibers for elastic cases with 30% V_f.

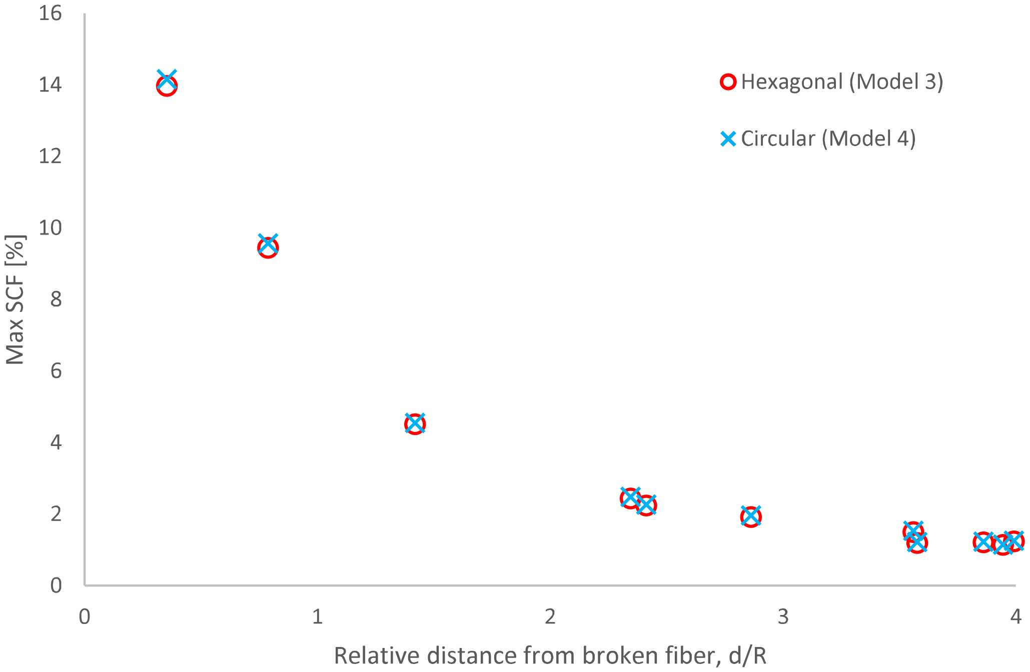

Figure 4.4. Maximum cross-sectional average SCF results for elastic cases with 30% V_f.

Considering the SCF results in Figure 4.2 and Figure 4.4, it can be seen that the results are nearly the same for hexagonal- and circular-shaped fibers. Since the cross-sectional areas of hexagonal- and circular-shaped fibers and their coordinates are the same, it is not unusual to obtain such similar results. Maximum SCF results of the closest few fibers for 60% V_f are presented in Table *4.2*. As it can be seen, for the first and seventh closest fibers, hexagonal shape results in higher SCF while for the rest of the fibers, vice versa so that any clear trend related to cross-sectional fiber shape cannot be observed. However, these small differences and unclear trend are due to the random rotations of the hexagonal-shaped fibers around their longitudinal axes. Hexagonal-shaped fiber rotations can cause them to be closer to or farther from each other unlike the circular-shaped fibers. They are closer to each other compared to circular-shaped fibers at the same coordinates if their corners are faced to each other and vice versa if their sides are faced to each other as shown in Figure 4.5. In the case that the intact and the broken fiber corners are faced to each other, corner of the intact fiber is loaded more as it is closer to the broken fiber. Therefore, depending on the rotations of the hexagonal-shaped fibers, a little higher or lower SCFs can be obtained on those small regions (corner or side) closest to broken fiber which causes the cross-sectional average SCFs to be obtained a little higher or lower. Since the rotations of the fibers are random, whether it is higher or lower cannot be predicted without looking at the rotations one by one. However, these differences caused by hexagonal-shaped fiber rotations are very small and it can be said that fiber shape barely affects the cross-sectional average SCF for elastic materials under uniaxial loading.

Table 4.2. *Maximum SCF results of the closest few fibers for 60% V_f with elastic material properties.*

d/R	SCF of hexagonal-shaped fibers [%]	SCF of circular-shaped fibers [%]
0.203	11.438	11.419
0.246	9.705	10.153
0.326	8.904	9.037
0.623	4.786	4.896
0.736	4.024	4.062
1.020	2.871	2.914
1.738	1.328	1.311

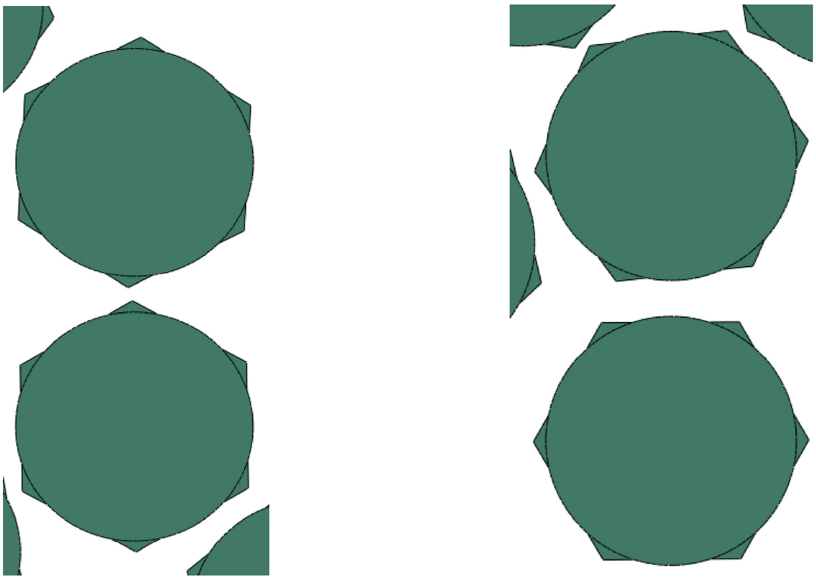
(a) (b)

Figure 4.5. Different rotations of hexagonal-shaped fibers presented with circular-shaped fibers: (a) corners are faced to each other, and (b) sides are faced to each other.

Considering Figure 4.1 and Figure 4.3, similar to the SCF results, stress recovery profiles of broken fibers nearly overlap with each other. The same reason in SCF results cause small differences between stress recovery profiles. Larger shear stresses on the material surrounding the broken fiber result in faster stress recovery in the broken fiber. Note that for the same applied strain, larger shear stresses occur in the material with larger stiffness value. When the corners of the closest intact fibers are directed to the broken fiber as in Figure 4.5a, then the stress recovery occurs a little faster for hexagonal broken fiber as those corner regions are formed of fiber material with high stiffness while matrix material with small stiffness exists on those regions in the case with circular fibers. Therefore, whether it is faster or slower depends on the rotations of the neighboring fibers. Similar to the differences in SCF results, differences in these results are so small, therefore, it can be said that fiber shape also barely affects the ineffective length results for elastic materials under uniaxial loading.

4.2.2. Cases with Elasto-plastic Matrix Material Properties

In section 4.2.1, it was shown that fiber cross-sectional shape barely affects the SCF and ineffective length for elastic materials. In this section, elasto-plastic material properties are defined for the matrix similar to the models in [1]. As explained in section 3.4, different SCF results are obtained for different strain inputs in case the elastic limit of one of the materials, for which elasto-plastic material properties are defined, is reached. Therefore, it is thought that together with elasto-plastic matrix properties, difference in fiber cross-sectional shape may affect the SCF and ineffective length results. For elasto-plastic matrix cases, 2% strain is used similar to the models in [1] which causes matrix to be deformed in plastic range. The stress recovery profiles of broken fibers and maximum cross-sectional average SCF results of intact fibers for 60% and 30% V_f are presented in Figure 4.6, Figure 4.7, Figure 4.8 and Figure 4.9, respectively.

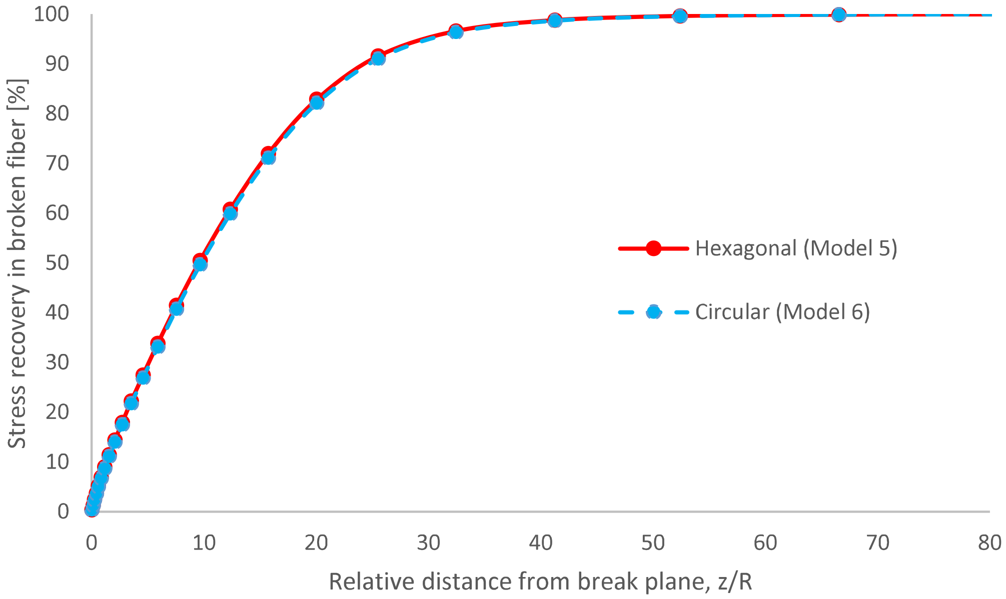

Figure 4.6. Stress recovery profiles of broken fibers for only matrix elasto-plastic cases with 60% V_f.

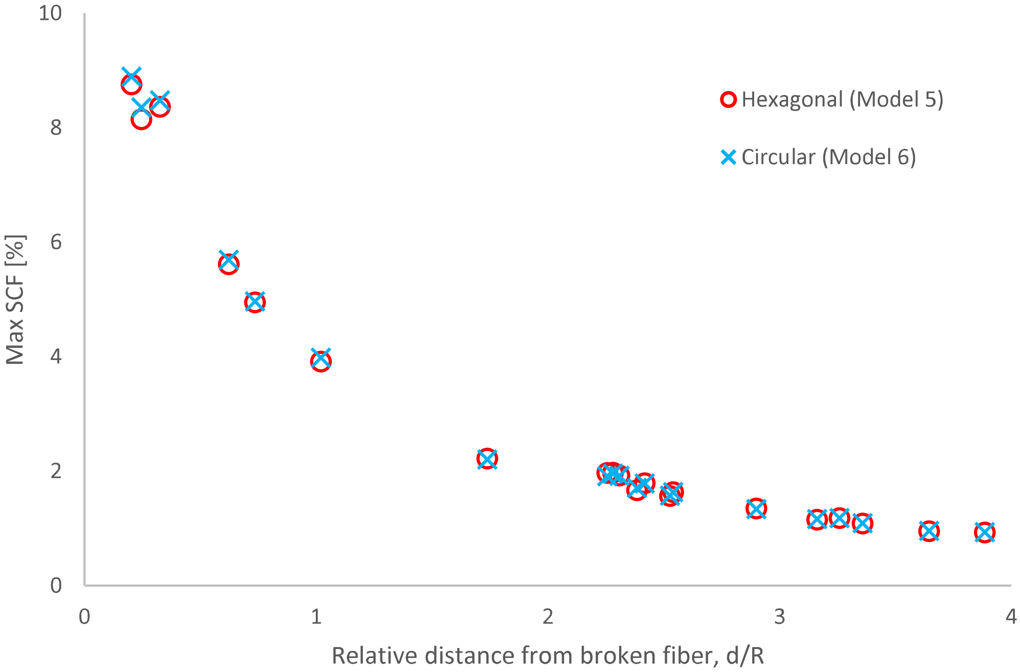

Figure 4.7. Maximum cross-sectional average SCF results for only matrix elasto-plastic cases with 60% V_f.

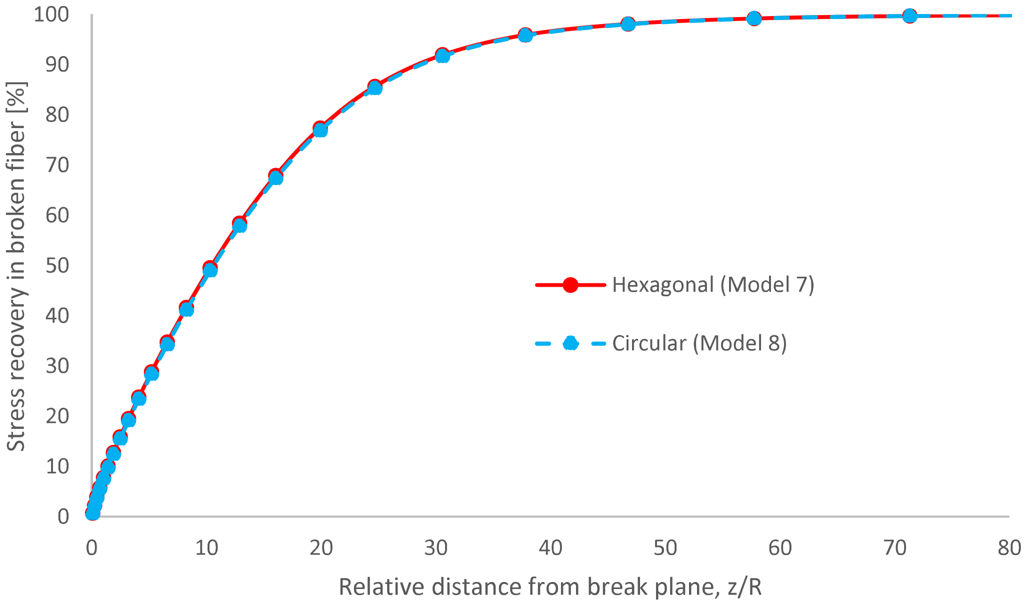

Figure 4.8. Stress recovery profiles of broken fibers for only matrix elasto-plastic cases with 30% V_f.

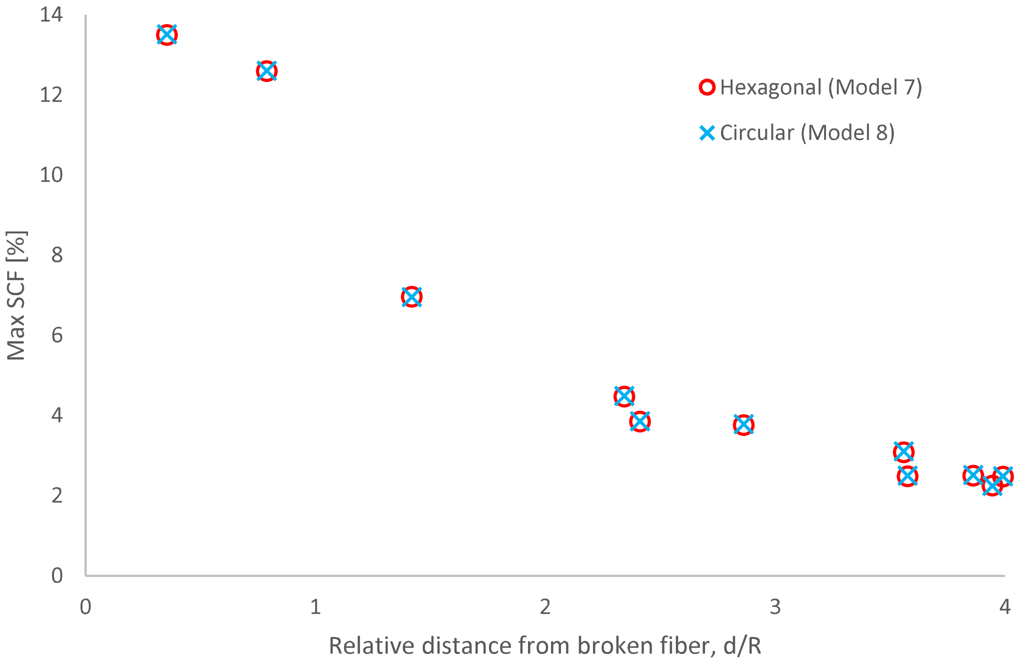

Figure 4.9. Maximum cross-sectional average SCF results for only matrix elasto-plastic cases with 30% V_f.

Considering the similar results in Figure 4.6, Figure 4.7, Figure 4.8 and Figure 4.9, it can be said that irrespective of the material properties defined in finite element models, cross-sectional fiber shape barely affects the cross-sectional average SCF and ineffective length. Those very small differences are due to the hexagonal-shaped fiber rotations as explained in section 4.2.1.

4.3. Analysis of Peak Fiber Stresses

As explained before, the stress field through fiber cross-section is not constant. As mentioned in [11], stresses higher than the cross-sectional average stress are found in the regions closest to the broken fiber. Therefore, in this section, SCFs in terms of peak stresses are examined instead of the cross-sectional average stresses as there might be differences due to the possibility of high stress concentrations on the sharp corners of hexagonal-shaped fibers. Initially, the results of models 1 and 2 are examined. SCF results of hexagonal- and circular-shaped fibers in terms of peak stresses are presented in Figure 4.10.

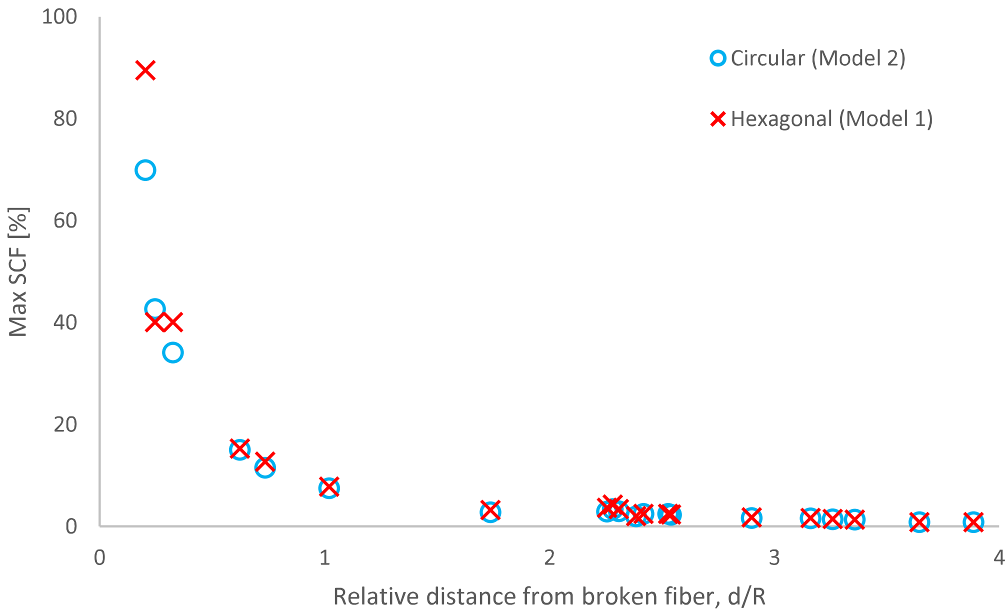

Figure 4.10. SCF results of hexagonal- and circular-shaped fibers in terms of peak stresses.

As can be seen in Figure 4.10, there is a significant difference between the hexagonal and circular closest fibers to the broken middle fiber. For a more detailed examination, results of the first five closest fibers to the broken fiber are given in Table *4.3*.

Table 4.3. *SCF results of hexagonal- and circular-shaped fibers for the first five closest fibers in terms of peak stresses.*

d/R	*Hexagonal peak SCF [%]*	*Circular peak SCF [%]*
0.203	89.494	69.911
0.246	40.069	42.646
0.326	40.075	34.136
0.623	15.249	15.022
0.736	12.702	11.523

Considering the results in *Table 4.3*, it is obvious that the difference between the closest fibers is significantly large while the others are relatively small, even most of them are negligible. Also, SCF results of hexagonally-shaped fibers are greater except for the second closest fibers to the broken fiber so that it is not possible to specify a clear trend for these results. According to the results, the difference in SCFs seems to be the hexagonal shape generating stress concentrations. However, a careful investigation attributed this to the same reason as described in section 4.2: random rotations of the hexagons. In Figure 4.11, the closest five intact fibers to the broken fiber can be seen with hexagonal and circular cross-sections. Due to the cornered shape of hexagonal cross-sections, unlike circular-shaped fibers, the actual values for the closest distance between intact and broken fibers to fiber radius ratio (d_h/R) for hexagonal-shaped fibers are not as given in *Table 4.3*. The actual values for both cross-sections are given in *Table 4.4*.

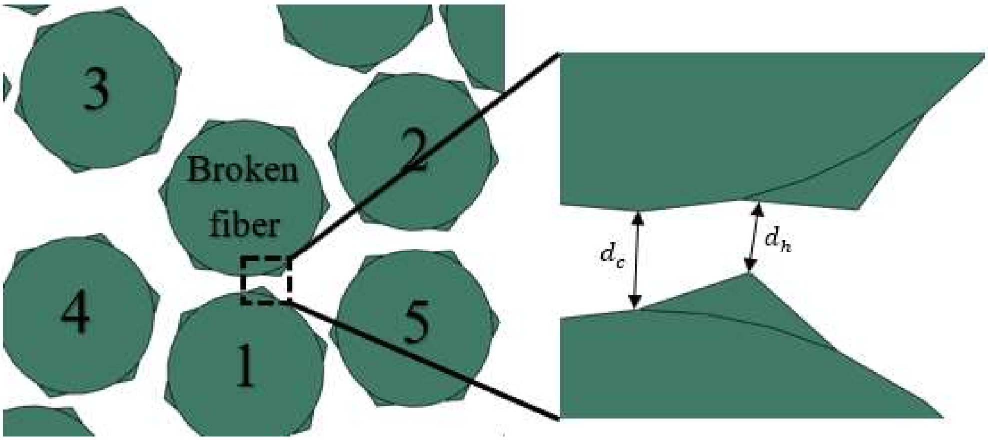

Figure 4.11. The closest five intact fibers to the broken fiber with hexagonal and circular shapes.

Table 4.4. *Actual d/R values for hexagonal and circular cross-sections*

Hexagonal, d_h/R	*Circular, d_c/R*
0.149	0.203
0.294	0.246
0.307	0.326
0.575	0.623
0.753	0.736

As it is presented in Table *4.4*, the closest points of the first, third and fourth closest hexagons are 36%, 6% and 8% closer to the broken fiber compared to their circular counterparts, respectively, while closest points of the second and fifth hexagons are 16% and 2% farther from the broken fiber, respectively. In order to understand whether the shape or distance affects the SCFs in terms of peak stresses, another finite element model with circular fibers was created where the closest five fibers are moved to their new positions so that the minimum distances between those five fibers to the broken fiber are the same for both models with hexagonal and circular cross-sections. Peak SCF results of the two models are given in Figure 4.12. Also, numerical values are given in Table *4.5* to examine them in detail.

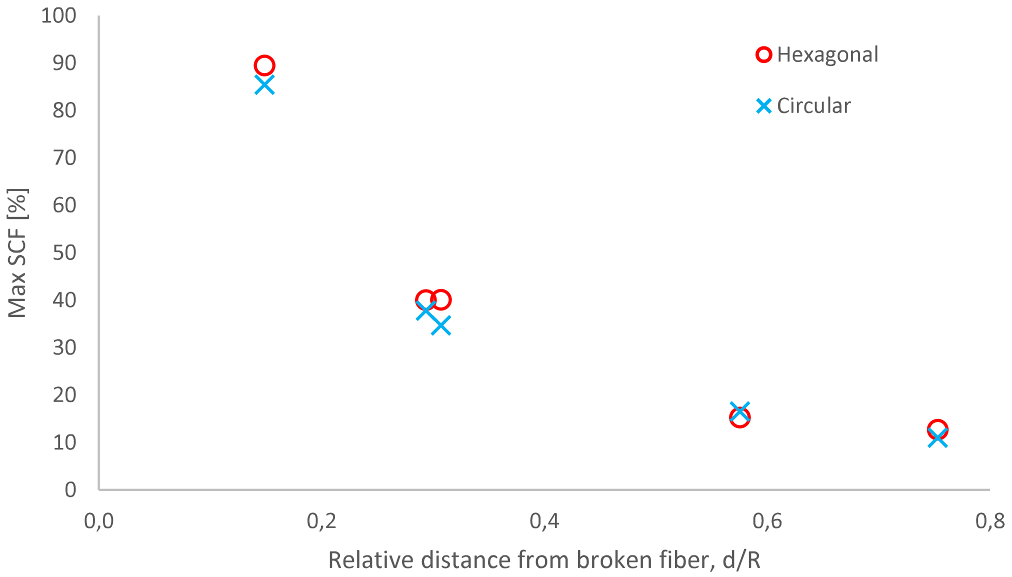

Figure 4.12. SCF results of hexagonal- and circular-shaped fibers in terms of peak stresses with the same minimum distances.

Table 4.5. *Numerical SCF results of hexagonal- and circular-shaped fibers in terms of peak stresses with the same minimum distances (previous values for fibers with circular cross-section given in parenthesis).*

d/R	*Hexagonal peak SCF [%]*	*Circular peak SCF [%]*
0.149	89.494	85.454 (69.911)
0.294	40.069	37.809 (42.646)
0.307	40.075	34.726 (34.136)
0.575	15.249	16.566 (15.022)
0.753	12.702	11.051 (11.523)

As can be seen in Table *4.5*, SCF values of the first, third and fourth closest circular-shaped fibers increased as they got closer to the broken fiber in the new finite element model while vice versa for the rest of the two fibers as they got farther. There was a large SCF difference between the first closest fibers due to that hexagonal-shaped intact fiber was 36% closer to the broken fiber. Therefore, the largest SCF result change occurred in the first closest circular-shaped fiber due to the 36% distance change while the others had minor changes due to the smaller distance differences. Consequently, the modified distances brought the results for both fiber shapes significantly closer together. This demonstrates that rather than the cross-sectional fiber shape, the surface-to-surface distance between broken and intact fibers affects the SCFs in terms of peak stresses.

In this study, all SCF results are presented with respect to the parameter d/R. In case of a fiber break in strength models, the stress value on a certain intact fiber is increased considering the distance between the broken and that certain intact fibers and considering the calculated SCF profile on that distance which is shown in [1]. Therefore, it is necessary to present the SCF results with respect to the parameter d/R as the results are implemented in strength models with respect to this parameter. However, during manufacturing process of composite materials, the surface-to-surface distance is not a controllable parameter, therefore, the peak SCF results can be related to the controllable parameter V_f as well. In composite materials with smaller V_f, due to the rareness of fibers, the distances between intact and broken fibers are larger compared to the ones in the materials with higher V_f. As it is shown in this section, with decreasing distance, peak SCF results increase. Therefore, it can be concluded that with increasing V_f, peak SCF results on the surrounding fibers increases.

CHAPTER 5

EFFECTS OF MECHANICAL BEHAVIOR OF THE MATERIALS AND THE APPLIED STRAIN ON SCF AND INEFFECTIVE LENGTH

In this chapter, effects of mechanical properties of the materials and the applied strain on SCF and ineffective length in terms of cross-sectional average fiber stresses are investigated. All finite element models have the same random fiber distribution for the same fiber volume fraction similar to the models in chapter 4.

5.1. Model Properties

4 new finite element models with 60% and 30% V_f are prepared in which both materials are defined with elasto-plastic properties. Corresponding material properties can be found in *Table 3.4*, Figure 3.15 and Figure 3.16. All models are prepared with hexagonal-shaped fibers without a need of circular-shaped fibers since in chapter 4, similar results were obtained for both cross-sections. 2% strain is applied as an input in two of the models to compare them with former models in chapter 4 (both elastic and only matrix elasto-plastic cases). For other two models, 7% strain is applied as it was reported in [6] as the strain-to-failure value of unidirectional steel fiber-reinforced composites. Properties of the four finite element models are given in Table *5.1*.

Table 5.1. *Properties of finite element models for elasto-plastic material cases.*

Model No.	***Model 9***	***Model 10***	***Model 11***	***Model 12***
V_f **[%]**	60	60	30	30
Fiber cross-section	Hexagonal	Hexagonal	Hexagonal	Hexagonal
Fiber material property	Elastoplastic	Elastoplastic	Elastoplastic	Elastoplastic
Matrix material property	Elastoplastic	Elastoplastic	Elastoplastic	Elastoplastic
Applied strain [%]	2	7	2	7

5.2. Results and Discussion

Stress recovery profiles of broken fibers and maximum cross-sectional average SCF results of intact fibers for Model 1 (both elastic case), Model 5 (only epoxy elastoplastic case) and Model 9 (both elastoplastic case) with 60% V_f are presented in Figure 5.1 and Figure 5.2, respectively. The same plots are given for 30% V_f (Model 3, Model 7 and Model 11) in Figure 5.3 and Figure 5.4.

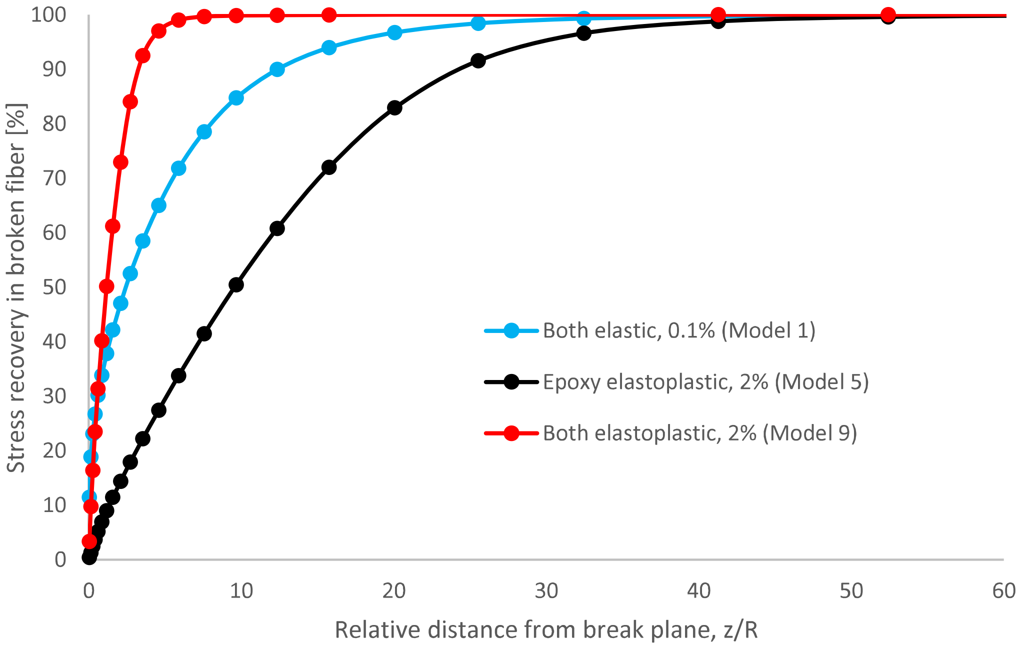

Figure 5.1. Stress recovery profiles of broken fibers for material mechanical behavior comparison with 60% V_f.

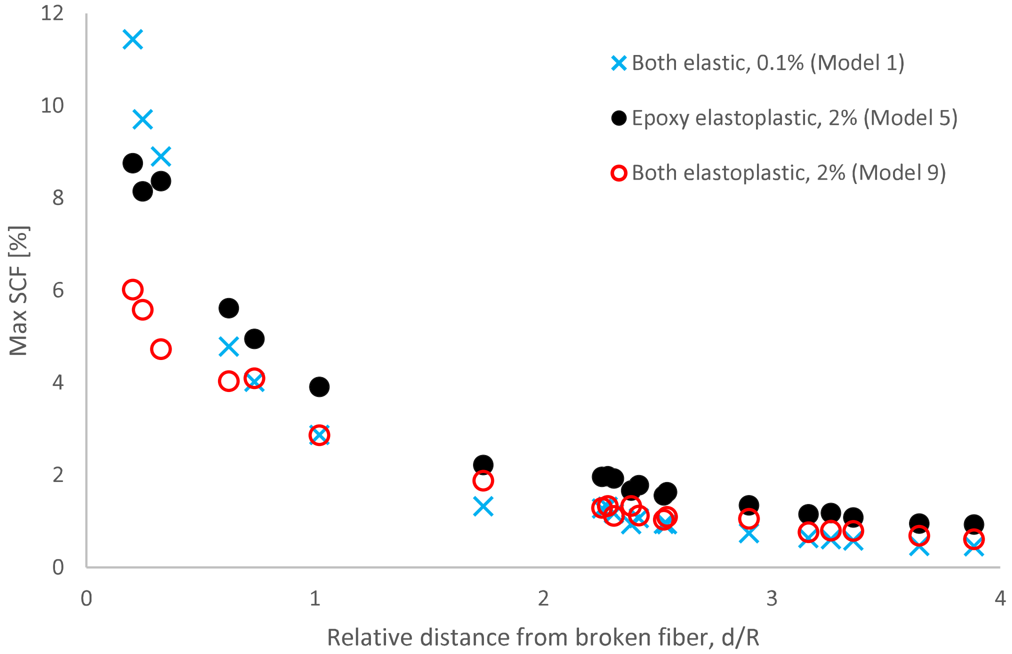

Figure 5.2. Maximum cross-sectional average SCF results of intact fibers for material mechanical behavior comparison with 60% V_f.

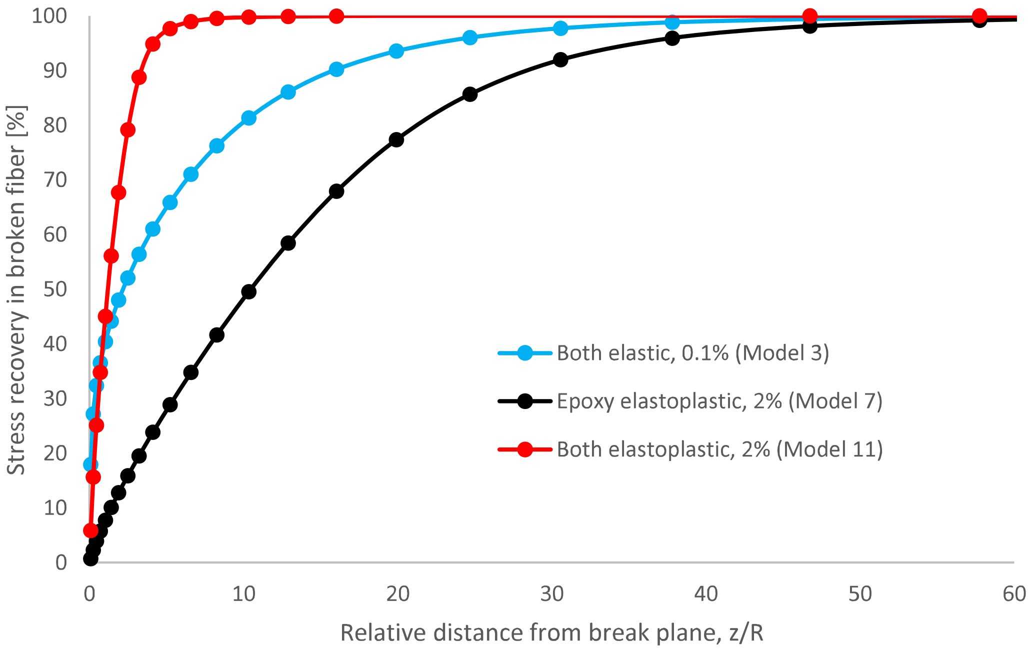

Figure 5.3. Stress recovery profiles of broken fibers for material mechanical behavior comparison with 30% V_f.

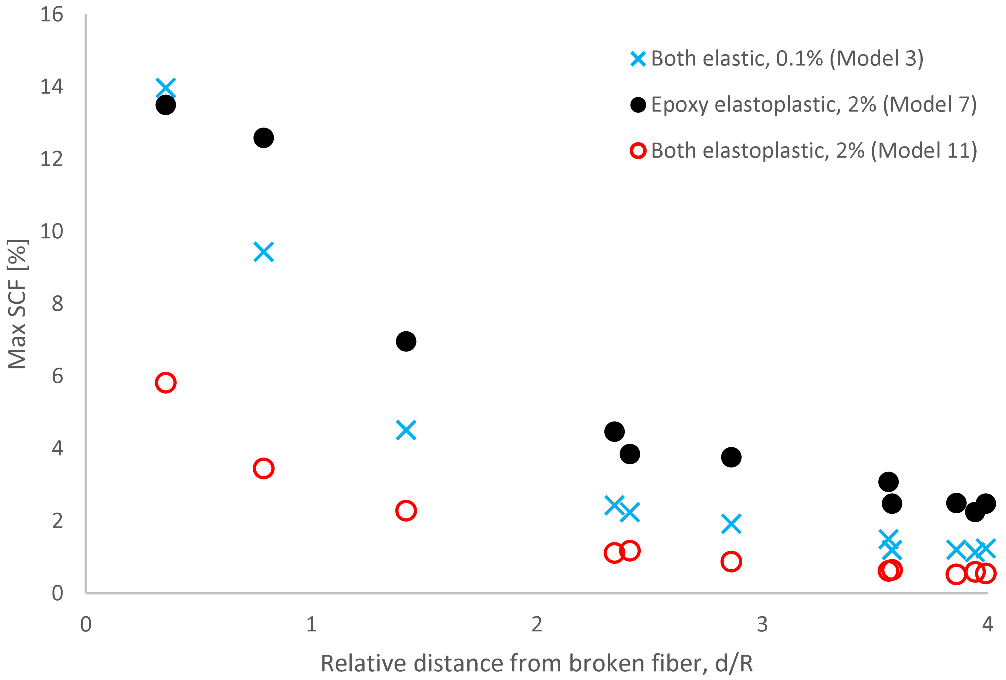

Figure 5.4. Maximum cross-sectional average SCF results of intact fibers for material mechanical behavior comparison with 30% V_f.

Considering the stress recovery results in Figure 5.1 and Figure 5.3 for Model 1 vs. Model 5 and Model 3 vs. Model 7, it can be seen that stress recovery of broken fibers in both elastic cases occur more rapidly. The reason for that is the shear stress build-up on the surrounding matrix. For the elastic materials cases (Model 1 and Model 3), the ratio of the broken fiber stress to be recovered to the shear stress developed on the surrounding matrix is constant due to the linear elastic behavior of the constituent materials. However, this ratio is larger for only matrix elastoplastic cases (Model 5 and Model 7) as shear stress development on matrix decelerates in plastic region. As shear stress build-up on the matrix in elastic cases is greater, the stress recovery occurs more rapidly in these cases. Similar reason applies to the differences between the results of Model 5 vs. Model 9 and Model 7 vs. Model 11. When elastoplastic material properties are defined for steel, the stress developed on steel fibers for a strain value in plastic region would be much lower compared to that of elastic-defined steel (nearly one tenth for 2% strain input). Therefore, the stress value of the broken fiber to be recovered is much lower which makes the stress recovery process more rapid and ineffective length shorter. The results show that in steel fiber composites under high strain, the plastic behavior of steel fibers speeds up the stress recovery process while the plastic behavior of epoxy matrix slows down the stress recovery process.

Considering the maximum cross-sectional average SCF results in Figure 5.2 and Figure 5.4 for Model 1 vs. Model 5 and Model 3 vs. Model 7, it can be said that stress concentrations on the intact fibers of models with elastoplastic epoxy are mostly greater than that of models with elastic material properties. The reason for that is the stiffness-dependency of SCF results. In all four models, stiffness of the fibers is constant due to linear elasticity. However, for the models with elastoplastic epoxy (Model 5 and Model 7), the tangential stiffness of the matrix is smaller in plastic region compared to that in models with elastic epoxy (Model 1 and Model 3). For the same applied strain, matrix material with smaller stiffness value on that strain carries smaller loads compared to matrix with higher stiffness and consequently intact fibers in the model with elastoplastic-defined matrix carry more load which causes higher SCFs on those intact fibers. Similar effect can be seen between Model 5 vs. Model 9 and Model 7 vs. Model 11 results. In Model 9 and Model 11, elastoplastic properties are defined for steel and for strain inputs in plastic region, steel fiber has smaller tangential stiffness values compared to elastic-defined steel. In these models (Model 9 and Model 11), due to stiffnesses of epoxy and steel becoming closer for strain input in plastic region, epoxy in Model 9 and Model 11 carries more load than the epoxy in Model 5 and Model 7. Therefore, smaller stress concentrations on intact fibers in Model 9 and Model 11 are obtained. Therefore, it can be concluded that in steel fiber composites under high strain, the plastic behavior of the matrix increases the stress concentrations whereas the plastic behavior of steel fibers reduces the stress concentrations.

Stress recovery profiles of broken fibers and maximum cross-sectional average SCF results of intact fibers for Model 9 (2% strain input) and Model 10 (7% strain input) with 60% V_f are presented in Figure 5.5 and Figure 5.6, respectively. The same plots are given for 30% V_f (Model 11 and Model 12) in Figure 5.7 and Figure 5.8.

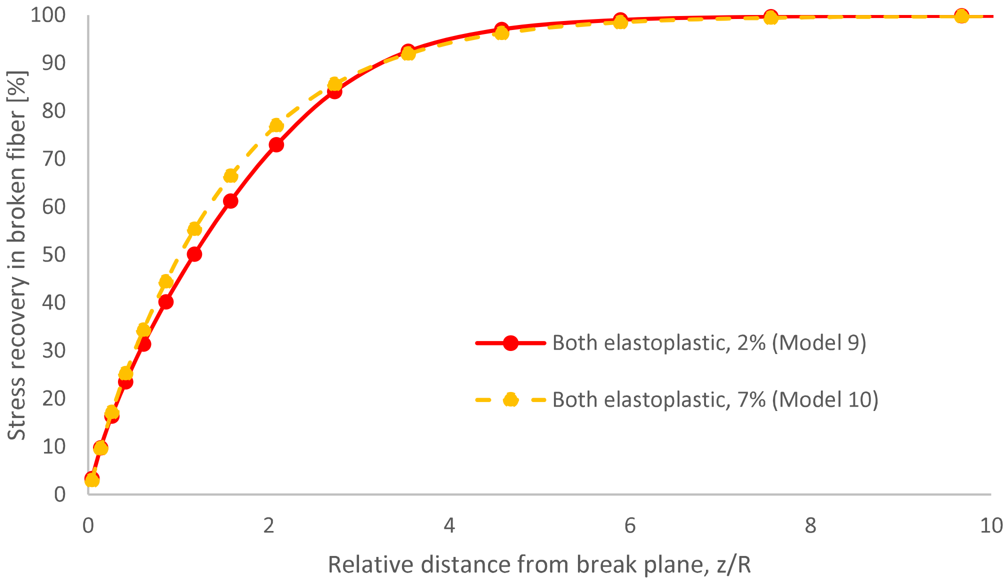

Figure 5.5. Stress recovery profiles of broken fibers for the models with 2% and 7% strain inputs and 60% V_f.

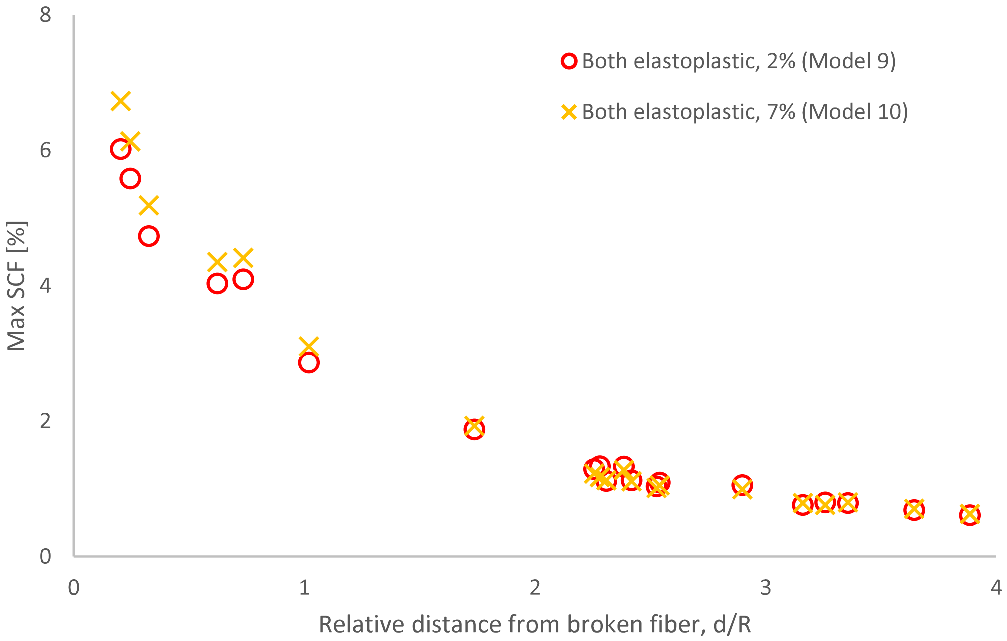

Figure 5.6. Maximum cross-sectional average SCF results of intact fibers for the models with 2% and 7% strain inputs and 60% V_f.

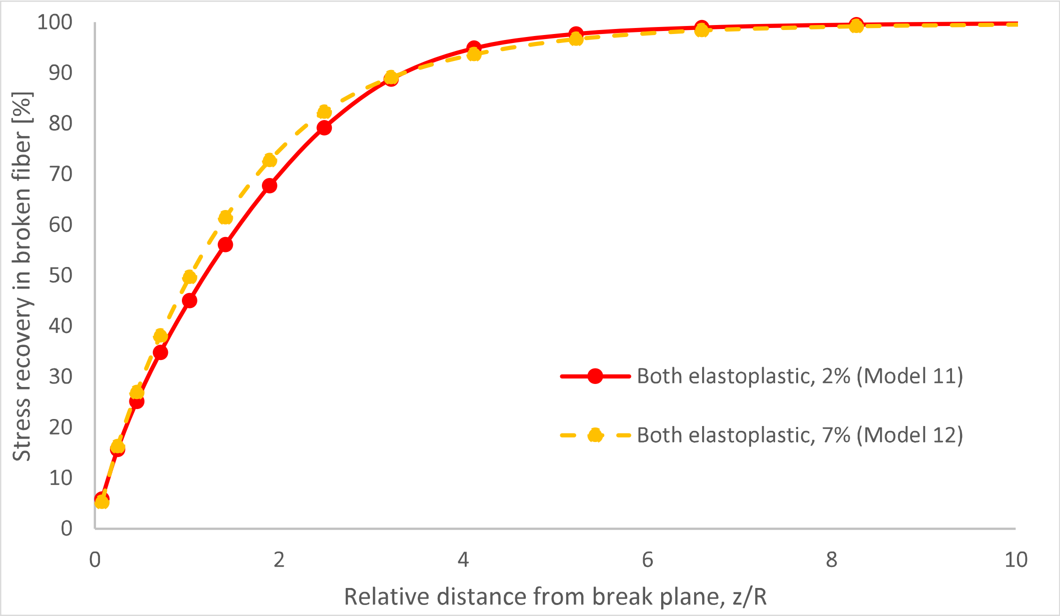

Figure 5.7. Stress recovery profiles of broken fibers for the models with 2% and 7% strain inputs and 30% V_f.

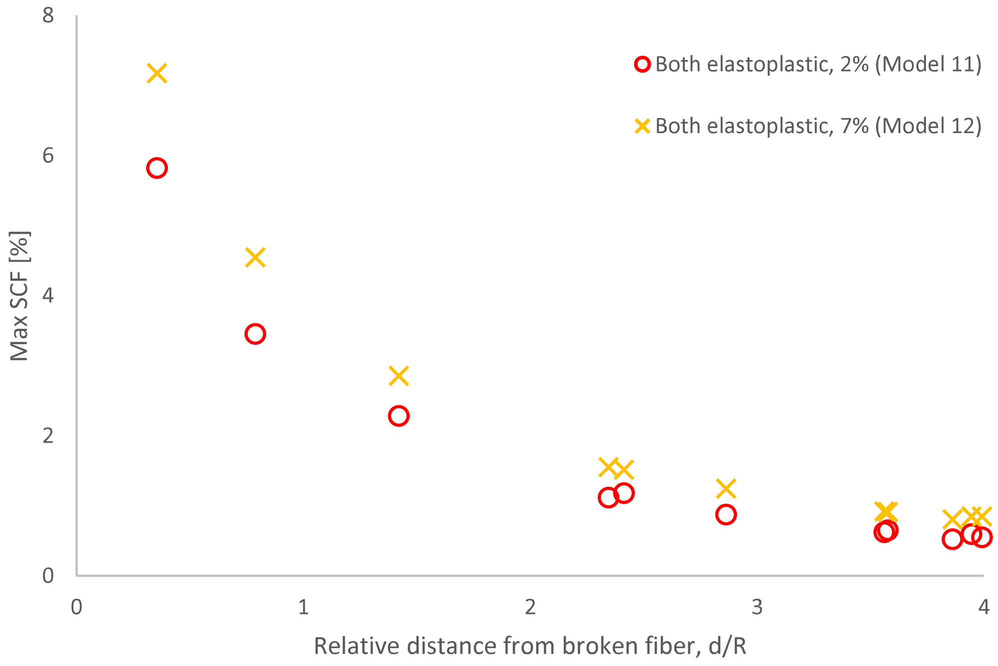

Figure 5.8. Maximum cross-sectional average SCF results of intact fibers for the models with 2% and 7% strain inputs and 30% V_f.

Examining the results in Figure 5.5 and Figure 5.7, it is obvious that stress recovery profiles of broken fibers for 2% and 7% applied strains are very close to each other. This can be explained as that stress to be recovered for broken steel fiber to shear stress on surrounding epoxy ratios for both strain levels are close to each other. The differences between them show up in SCF results (Figure 5.6 and Figure 5.8), where the results of the 7% strain level are slightly higher than the 2% one. The reason for this can be explained by examining the stress – strain plots of steel and epoxy used in this work given in Figure 5.9.

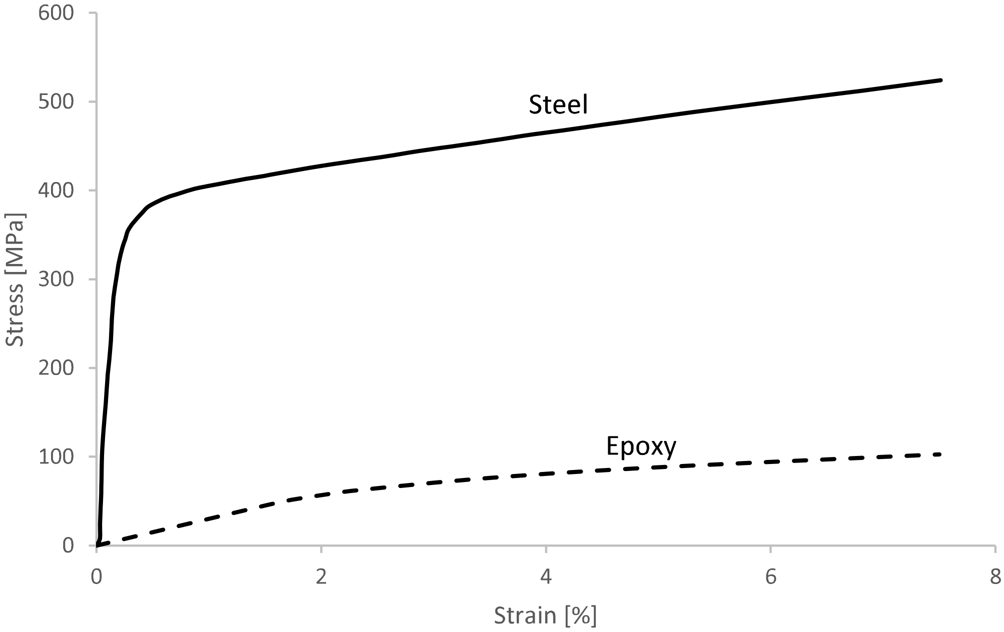

Figure 5.9. Stress – strain plots of steel and epoxy up to around 8% strain.

Apparently, slopes of the curves, thus the tangential modulus values, decrease with increasing strain. This decrease rate is higher in epoxy compared to steel fibers. Therefore, stiffness ratio of steel and epoxy increases for higher strains. Due to the increase in the stiffness ratio, intact fibers in the model with 7% applied strain carry more load compared to those in the models with 2% applied strain causing higher stress concentrations. So, the effect of higher strain in the plastic region depends on the relative mechanical behavior of fibers and epoxy in the plastic region.

5.3. Hypothetical Model

As explained before, ineffective length depends on the shear stress build-up on the surrounding material and SCF depends on material stiffnesses. In this section, a hypothetical (unrealistic) finite element model is prepared where elastoplastic material properties are defined for steel while only elastic properties are defined for matrix with Young's modulus of epoxy. Corresponding material properties can be found in *Table 3.4* and Figure 3.16. For strain levels in plastic region, the stress values on steel fibers are lower than that of the elastic-defined fibers. Besides this, matrix material is elastic and with increasing strain, stress build-up on it increases linearly and therefore, for elastic-defined matrix, stress value would be greater than that of elastoplastic-defined matrix in case the elastic limit is reached. Also, stiffness remains on its maximum value. With these mechanical properties of the materials, it is expected to obtain stress recovery to be more rapid and SCFs on intact steel fibers to be smaller. The same random fiber distribution in models 9 and 10 is used. Properties of this new finite element model are given in Table *5.2*.

Table 5.2. *Properties of hypothetical finite element model*

Model No.	***Model 13***
V_f [%]	60
Fiber cross-section	Hexagonal
Fiber material property	Elastoplastic
Matrix material property	Elastic
Applied strain [%]	7

The hypothetical model is compared with Model 9 (both elastoplastic, 2% strain) and Model 10 (both elastoplastic, 7% strain) as the smallest SCF results and the fastest stress recovery are obtained from Model 9 and Model 10, respectively. Stress recovery profiles of broken fibers and maximum cross-sectional average SCF results of intact fibers for Model 9, Model 10 and Model 13 are presented in Figure 5.10 and Figure 5.11, respectively.

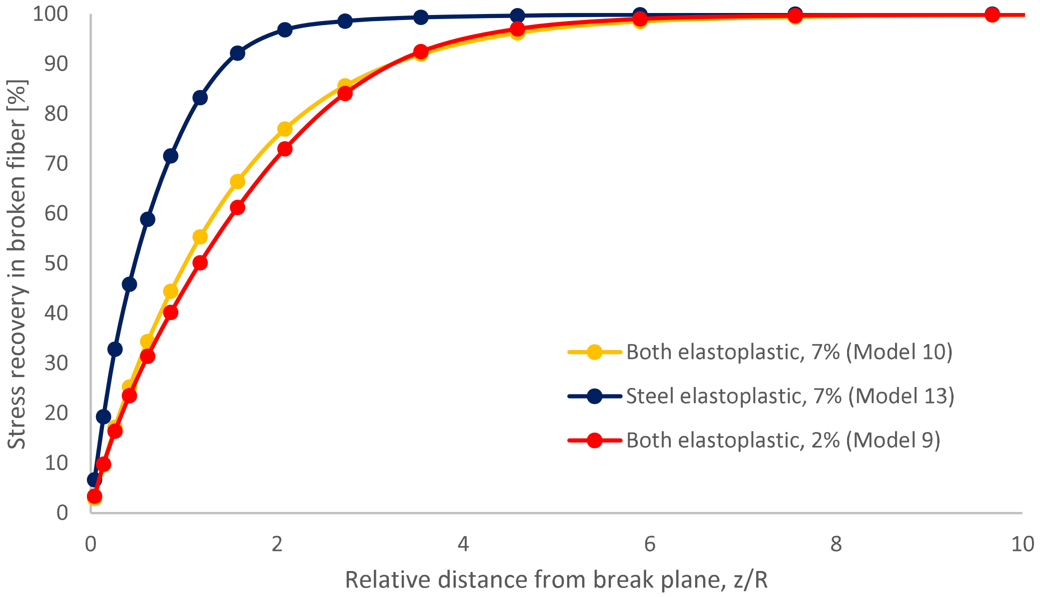

Figure 5.10. Stress recovery profiles of broken fibers for models 9, 10 and 13.

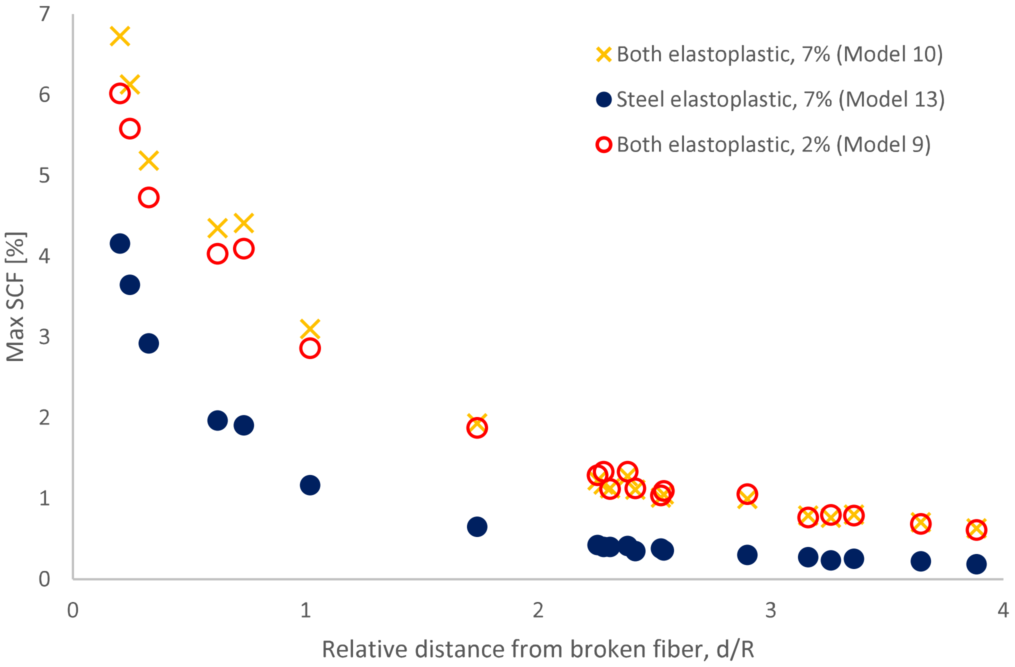

Figure 5.11. Maximum cross-sectional average SCF results of intact fibers for models 9, 10 and 13.

As can be seen from Figure 5.10 and Figure 5.11, the stress recovery occurs more rapidly and maximum cross-sectional average SCFs are significantly smaller for hypothetical model (Model 13), which were expected. These results mean that when a fiber is broken in a plane, the extra loads carried by intact fibers would be smaller and the broken fiber would recover its load carrying capacity in a shorter distance in fiber direction. These features, therefore, increase the failure strain of the composite material. Using such a matrix material could be beneficial for enhancing the structural integrity of the products.

In this chapter, the results of several finite element models with different mechanical properties of steel and epoxy materials were compared with the application of two different strain values. As a result, it was shown that changing mechanical properties of materials cause different ineffective length and SCF results. In case the elastic limit is reached, plastic behavior of steel fibers reduces the stress concentrations and speeds up the stress recovery while plastic behavior of the matrix increases the stress concentrations and slows down the stress recovery. Also, it was shown that results change depending on the applied strain and as it was mentioned before in section 3.4, calculating SCFs at a strain close to failure strain of the composite gives more accurate results [9]. Therefore, since failure strain of steel fiber-reinforced composites, i.e. 7% reported in [6], are in the vicinity of plastic region for both steel and epoxy, defining elastoplastic properties to both materials with the proper strain input in finite element analyses gives more accurate results while predicting the failure strain of steel fiber-reinforced composites.

CHAPTER 6

STRESS CONCENTRATIONS IN STEEL FIBERS AFTER UNLOADING AND RELOADING

In chapters 4 and 5, stress concentrations in steel fibers in case of a broken fiber were examined after loading the models for different parameters. Due to the ductile nature of steel fibers, loadings resulted in plastic deformations on the matrix and fibers for these cases. Thus, these permanent deformations are expected to cause residual stresses on the matrix and fibers after unloading which can alter the stress redistributions when the composite is reloaded. In this chapter, therefore, the stress concentrations are investigated in the case when the tensile load is applied in the elasto-plastic range, removed and applied again. Same random fiber distributions for the same fiber volume fractions are used similar to the models in chapters 4 and 5.

6.1. Description of Unloading and Reloading Processes

Initially, models are loaded with a displacement input corresponding to the desired strain causing a plastic deformation on the matrix and fibers. After that, models are unloaded to zero-load condition and at the end, they are reloaded. It should be noted that, due to the plastic deformation, the displacement does not return to zero at zero load. A state of residual stress arises in the fibers and the matrix. Different than the previous cases, these processes require two different analyses. In the first analysis, it is aimed to determine the displacement input corresponding to zero-load condition on the surface after unloading process. This analysis includes several steps to determine the zero-load strain. In the first step, desired displacement is applied on the surface as loading process. In the following ones, displacement input is decreased to an estimated value step by step. This estimated value is roughly calculated to be around the value corresponding to zero-load condition. Since the main load-carrying components in composite materials are fibers, these rough calculations are done as if the whole part is comprised of fiber material. After the analysis is completed, the reaction forces on the surface are calculated for each step to detect the strain value at which the reaction forces are approximately zero. A sample calculation of estimated strain value is as follows:

Let the applied strain be 7%. According to Figure 3.16, 7% strain value corresponds to approximately 516 MPa of average stress in steel. After unloading, the elastic strain is recovered, and only residual plastic strain is left. This plastic strain is calculated as follows:

$$\varepsilon_p = \varepsilon_{total} - \varepsilon_e = 0.07 - \frac{516\ MPa}{193000\ MPa} = 0.0673 \qquad \text{(Eq. 6.1)}$$

where 193000 MPa corresponds to Young's modulus of fiber. Thus, the permanent strain left after the application of 7% strain is around 6.73%. In the next step, the applied strain value is decreased gradually until 6.6% strain which is slightly lower than the calculated permanent strain value. The reaction forces in fiber direction corresponding to each strain is calculated (Table *6.1*).

Table 6.1. *Reaction forces after decreasing the strain to 6.6% for 7% loading strain input.*

Strain [%]	***Reaction Force on Surface [N]***
7	35.62
6.95	29.65
6.9	23.68
6.85	17.71
6.8	11.74
6.75	5.77
6.725	2.78
6.7	-0.20
6.65	-6.17
6.6	-12.14

As expected, the reaction force on the surface decreases linearly and its sign changes between 6.70625% and 6.7% strains. Linear interpolation is performed between these values to find the zero-load condition strain and it is found as 6.7017%. After finding zero-load condition strain, in the second analysis, only three steps are created to execute loading, unloading and reloading processes. In the first step, 7% strain is applied and after that, this value is decreased to 6.7017%. As a last step, strain input is increased to 7% again, by which all three processes are completed. The results of unloading and reloading processes are compared with the results of loading process. Reaction forces on the surface for the first two steps, loading and unloading, are given in Table *6.2*. Since the calculated reaction forces for loading and unloading processes are in the order of 10^1 N and 10^{-3} N, respectively, it can be said that decreasing strain to 6.7017% represents the zero-load condition for 7% applied strain. The same procedure is applied for 4% and 2% applied strains and the results can be seen in Table 6.3, Table 6.4, Table 6.5 and Table 6.6. The last strain values in Table *6.4* and Table *6.6* represent the unloaded conditions. Besides reloading the material to the same initial applied strain in loading, a different method is also used. In this method, the material unloaded from 7% loading strain is reloaded with a displacement input corresponding to a force that gives 2% and 4% strain to the initial undeformed material. After that, the results of these reloading processes are compared with the results of pure loading processes with 2% and 4% applied strains.

Table 6.2. *Reaction forces after loading and unloading processes for 7% applied strain.*

Strain [%]	***Reaction Force on Surface [N]***
7	35.62
6.7017	0.0031

Table 6.3. *Reaction forces after decreasing the strain to 3.7% for 4% loading strain input.*

Strain [%]	***Reaction Force on Surface [N]***
4	31.73
3.9	19.79
3.8	7.85
3.75	1.88
3.7	-4.09

Table 6.4. *Reaction forces after loading and unloading processes for 4% applied strain.*

Strain [%]	***Reaction Force on Surface [N]***
4	31.73
3.73425	0.000122

Table 6.5. *Reaction forces after decreasing the strain to 1.75% for 2% loading strain input.*

Strain [%]	***Reaction Force on Surface [N]***
2	28.49
1.9	16.55
1.8	4.61
1.75	-1.36

Table 6.6. *Reaction forces after loading and unloading processes for 2% applied strain.*

Strain [%]	***Reaction Force on Surface [N]***
2	28.49
1.76139	0.000017

6.2. Model Properties

Three new finite element models were prepared to examine the stress concentrations in intact fibers due to the residual stresses after unloading and the tensile stresses after reloading the steel fiber-reinforced composites. Materials were defined with elastoplastic material behavior. The procedure of three steps was described in section 6.1. The model properties are presented in Table *6.7*.

Table 6.7. *Model properties for unloading and reloading processes.*

Model No	**Model 14**	**Model 15**	**Model 16**
V_f [%]	60	60	60
Fiber cross-section	Hexagonal	Hexagonal	Hexagonal
Fiber material property	Elastoplastic	Elastoplastic	Elastoplastic
Matrix material property	Elastoplastic	Elastoplastic	Elastoplastic
Applied strain [%]	2	4	7

6.3. Results and Discussion

The results of all three steps are obtained for all three models. Maximum cross-sectional average SCF and ineffective length results of unloading and reloading processes are compared with the results of loading process.

6.3.1. Unloading Process

Maximum cross-sectional average SCF results of unloading and loading processes for 7%, 4% and 2% applied strains are given in Figure 6.1, Figure 6.2 and Figure 6.3, respectively. According to the figures, after unloading, there is an increase in the cross-sectional average SCFs. In Figure 6.4 and Figure 6.5, average axial stresses in the closest fiber to and a fiber faraway from the broken fiber with respect to axial distance can be seen for 7% loading strain input. In this case, the material is loaded with 7% strain and unloaded. The same results of loading process are given in Figure 6.6 and Figure 6.7 to compare the stress levels of loading and unloading processes.

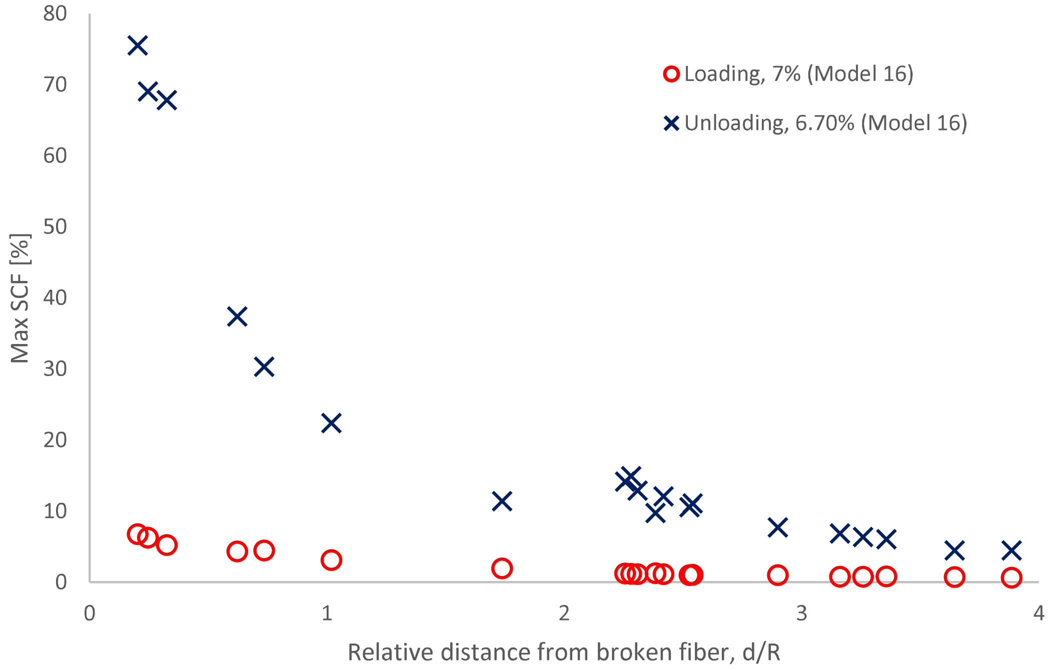

Figure 6.1. Maximum cross-sectional average SCF results of loading and unloading for 7% applied strain.

Figure 6.2. Maximum cross-sectional average SCF results of loading and unloading for 4% applied strain.

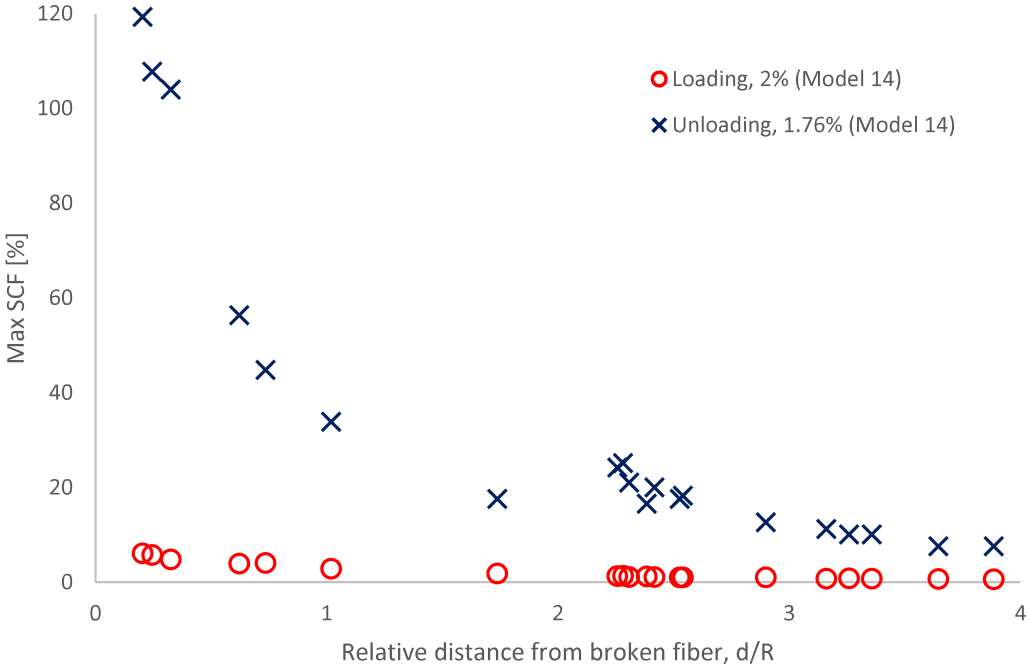

Figure 6.3. Maximum cross-sectional average SCF results of loading and unloading for 2% applied strain.

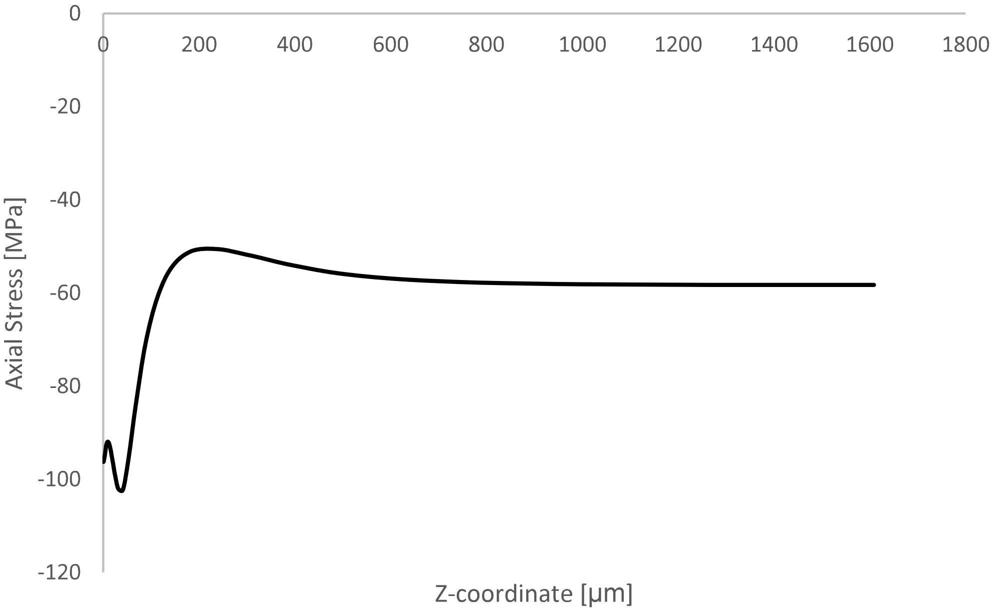

Figure 6.4. Axial stress vs. axial distance plot of the closest fiber to the broken fiber after unloading process for 7% loading strain input.

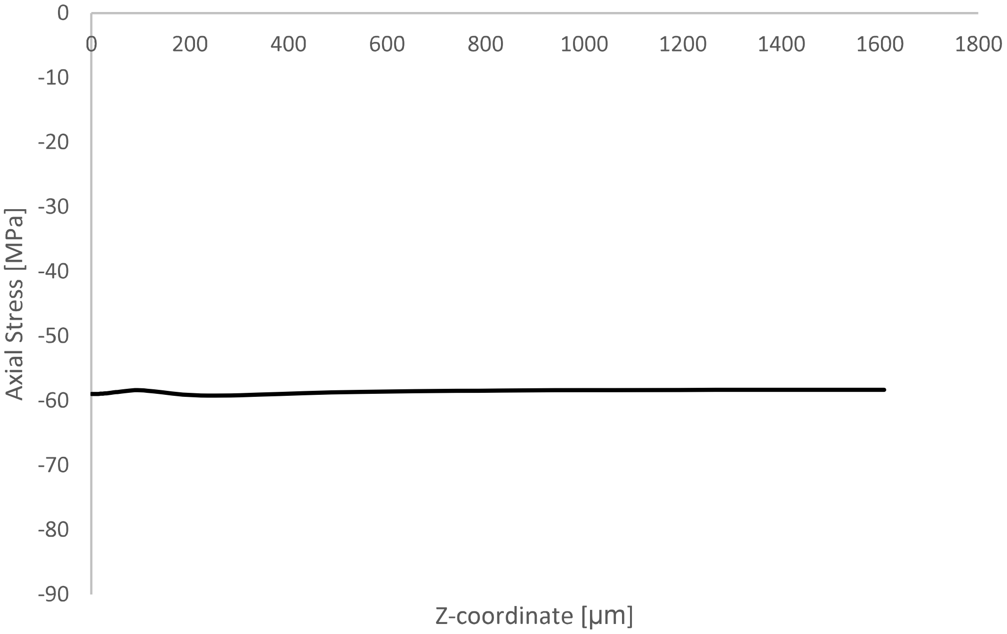

Figure 6.5. Axial stress vs. axial distance plot of a fiber faraway from the broken after unloading process for 7% loading strain input.

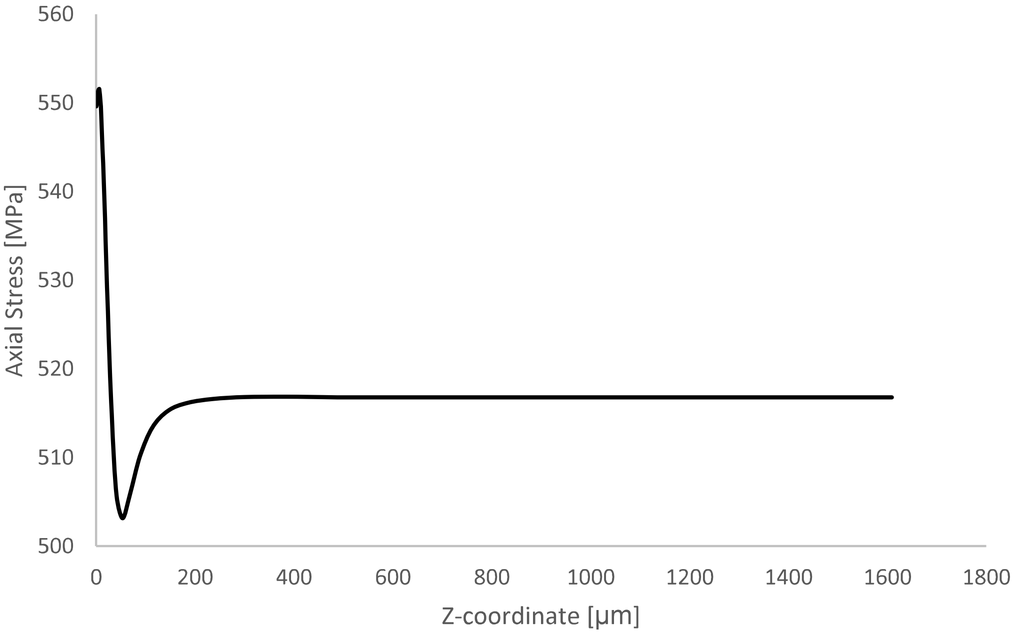

Figure 6.6. Axial stress vs. axial distance plot of the closest fiber to the broken fiber after loading process for 7% loading strain input.

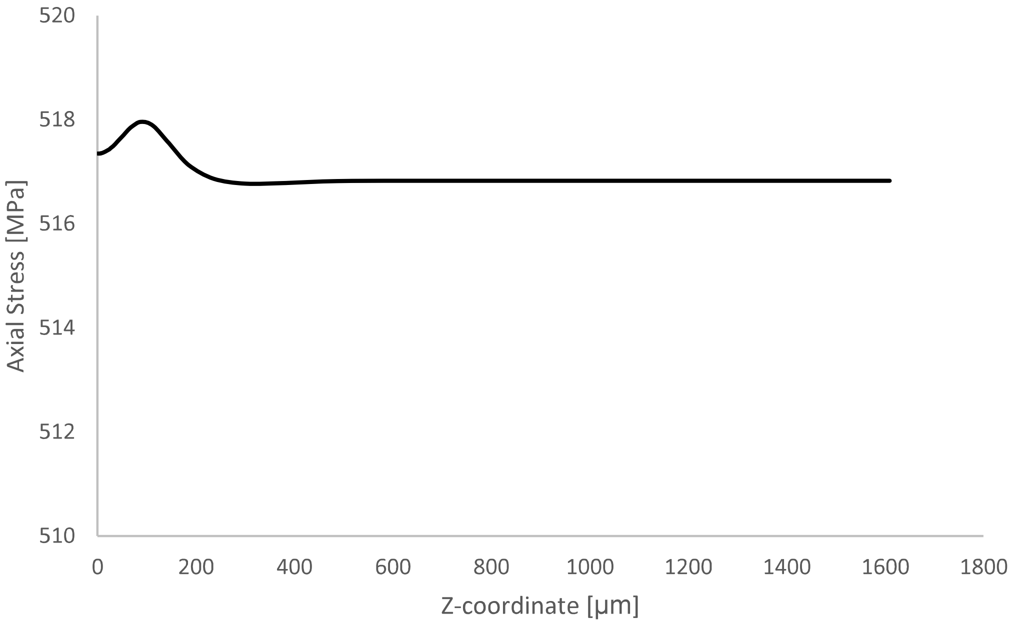

Figure 6.7. Axial stress vs. axial distance plot of a fiber faraway from the broken after loading process for 7% loading strain input.

As shown in Figure 6.4 and Figure 6.5, axial fiber stresses after unloading are negative which means that they are in compression. As it was mentioned in section 6.1, the main load-carrying components are fibers. Therefore, most of the load are relieved from the fibers during unloading which causes zero-load strain value to be close to the residual plastic strain value of fiber material. However, this is not the case for matrix material. Due to the low stiffness value of matrix material, only a small portion of the tensile load on matrix is relieved during unloading. This results in matrix to remain in tension and accordingly fibers to be in compression after unloading. The following sample calculations explain the reason for the fibers to be in compression. Zero-load strain value was found as 6.7017% for 7% loading strain in section 6.1. Axial stress in epoxy after unloading can be calculated as in equation 6.2.

According to Figure 3.15, 7% strain value corresponds to approximately 100 MPa of average stress in epoxy.

$$\sigma_{residual} = 100\ MPa - (0.07 - 0.067017) * 3000\ MPa = 91\ MPa \quad \text{(Eq. 6.2)}$$

The axial residual stress on epoxy after unloading of whole composite material is around 91 MPa which means that the entire elastic strain on matrix is not recovered and therefore it is still in tension. This results in fibers to be in compression to obtain zero load on the surface. Axial fiber stress after unloading can be calculated as follows:

$$\begin{aligned}\sigma_{residual} &= 516\ MPa - (0.07 - 0.067017) * 193000\ MPa \\ &= -60\ MPa\end{aligned} \qquad \text{(Eq. 6.3)}$$

As a result, after unloading, due to the different stiffness values of epoxy and steel, one of them is left in tension and the other in compression balancing each other.

Stress recovery results of loading and unloading processes for 7%, 4% and 2% applied strains are given in Figure 6.8, Figure 6.9 and Figure 6.10, respectively. Axial stress values of the broken fiber with respect to axial distance after loading and unloading processes are given in Figure 6.11. In this case, the material is loaded with 7% strain and unloaded.

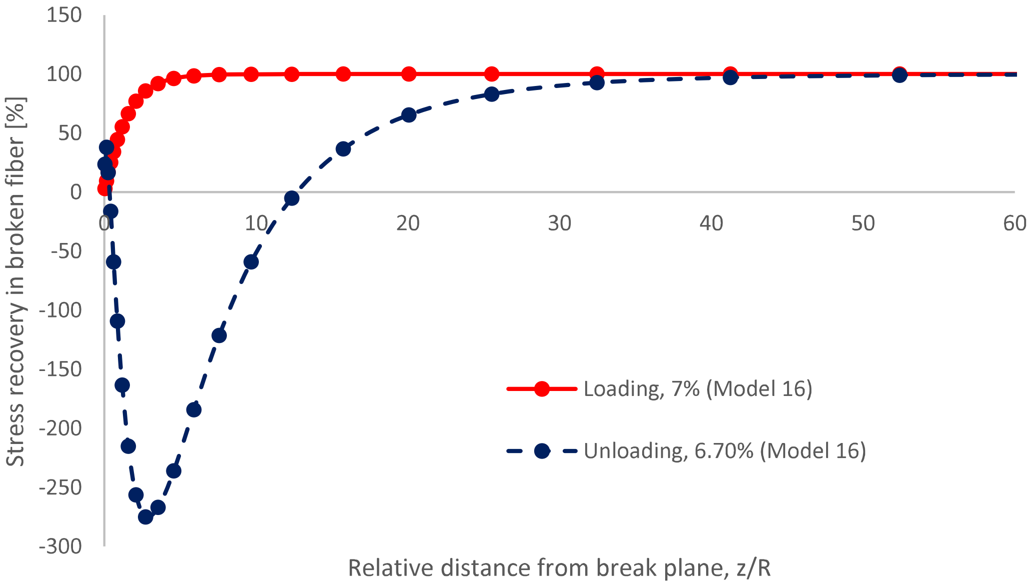

Figure 6.8. Stress recovery results of loading and unloading processes for 7% applied strain.

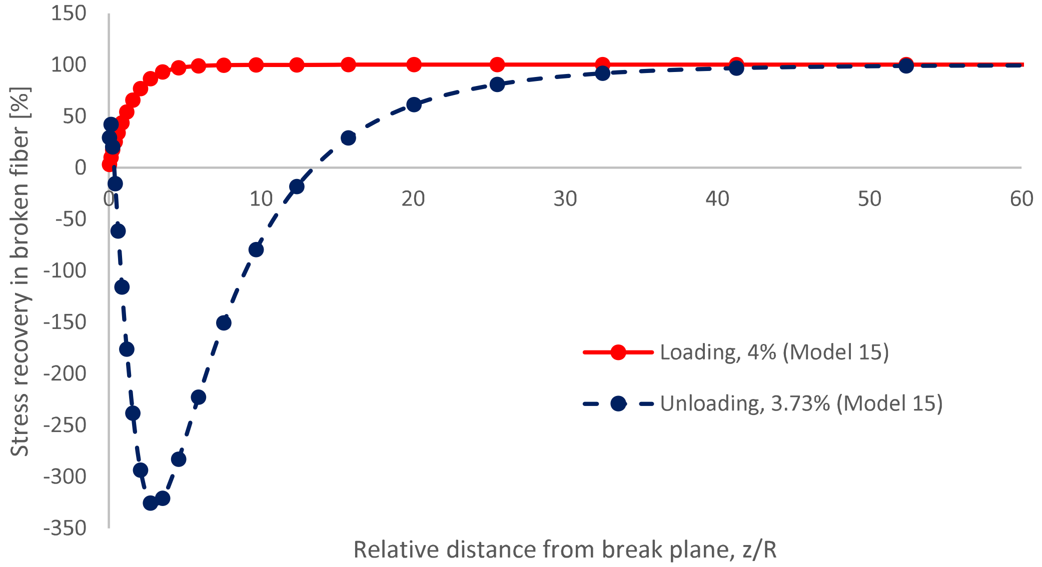

Figure 6.9. Stress recovery results of loading and unloading processes for 4% applied strain.

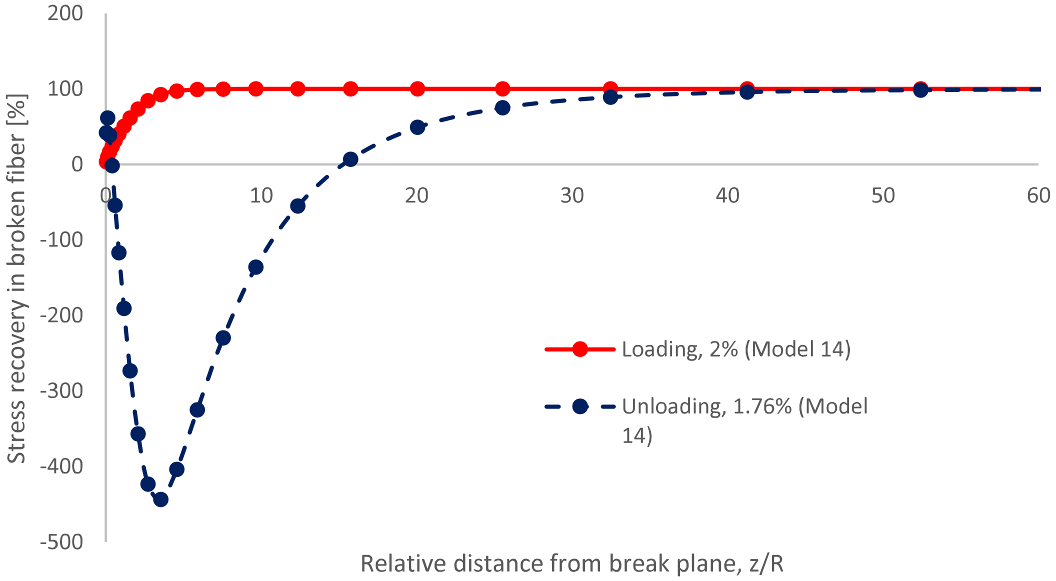

Figure 6.10. Stress recovery results of loading and unloading processes for 2% applied strain.

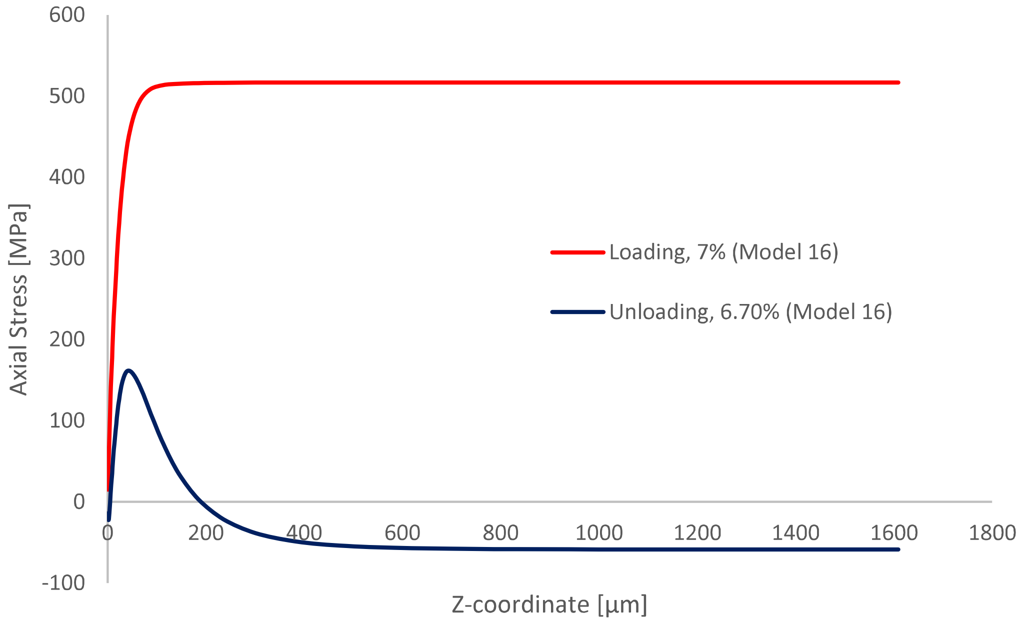

Figure 6.11. Axial stress vs. axial distance plot of the broken fiber for 7% applied strain.

Considering the stress recovery plots presented in Figure 6.8, Figure 6.9 and Figure 6.10, it can be said that stress recovery trend of the broken fiber at the end of unloading process is different than that of the loading process. In loading process, stress recovery gradually increases while getting away from the crack plane. However, in unloading process, stress recovery starts after a dramatic decrease. Therefore, it is completed in a much longer distance from the crack plane compared to that of loading process. The reason for the dramatic decrease near the crack plane is the axial stress values on the broken fiber. As shown in Figure 6.11, after unloading process, broken fiber is in tension in some regions that are very close to crack plane. After getting away more from the crack plane, broken fiber turns out to be in compression and axial stress converges to its final value which is obtained at a faraway distance that is not affected by fiber break. In Table *6.8*, axial stress results on broken fiber at the end of loading and unloading processes can be seen. Also, their differences are given.

Table 6.8. *Axial stress results on broken fiber at the end of loading and unloading processes for 7% applied strain.*

Z-coordinate [µm]	End of loading [MPa]	End of unloading [MPa]	Axial stress difference [MPa]
0.636	15.247	-13.919	29.165
2.079	49.652	-22.228	71.880
3.910	88.732	-9.810	98.542
6.231	130.486	9.475	121.011
9.175	177.346	34.622	142.724
12.909	229.353	64.042	165.311
17.645	285.687	95.935	189.752
23.652	343.195	126.408	216.787
31.269	397.519	150.543	246.976
40.930	442.185	161.484	280.700
53.184	474.808	156.795	318.014
68.724	496.962	138.569	358.393
88.433	508.721	108.225	400.495
113.430	513.487	71.346	442.142
145.133	515.237	34.721	480.516
185.341	515.971	2.992	512.979
236.336	516.333	-21.559	537.892
301.012	516.554	-38.450	555.004
383.039	516.592	-48.790	565.382
487.071	516.522	-54.379	570.901
619.012	516.496	-56.997	573.493
786.350	516.499	-58.094	574.594
998.580	516.500	-58.526	575.026
1267.747	516.500	-58.681	575.181
1609.124	516.500	-58.727	575.227

At the end of loading process, all fibers are in tension. Axial tensile stress value decreases towards the crack plane for broken fiber. After unloading, all fibers are compressed, and axial stress values reach to a certain amount. As it is presented in axial stress difference column in Table *6.8*, the amount of compression on the broken fiber decreases towards the crack plane due to the free surface of the broken fiber on the crack plane. Because of this reason, some portion of broken fiber is left in tension and this causes such a stress recovery trend in broken fiber.

Stress concentrations at the end of the unloading are found to be much higher than that of the loading processes. Also, stress recovery of broken fiber after unloading is much slower than one after loading. From these results, at the first sight one could think that stress state of the fibers after the unloading process is more critical. However, in this case, the material is in unloaded condition and the residual stress values on the fibers after unloading process are around 60 MPa (for 7% strain input case), so the stress concentrations were calculated with respect to these values. At the end of loading process, these values are found to be around 500 MPa for the same strain input case. Besides, the residual stress is compressive. Hence, despite the high stress concentrations and slow stress recovery profiles, materials are not in a critical condition after unloading process.

6.3.2. Reloading to Initial Strain Level

Maximum cross-sectional average SCF results of reloading and loading processes for 7%, 4% and 2% strain inputs are given in Figure 6.12, Figure 6.13 and Figure 6.14, respectively. Stress recovery results of loading and reloading processes for 7%, 4% and 2% strain inputs are given in Figure 6.15, Figure 6.16 and Figure 6.17, respectively.

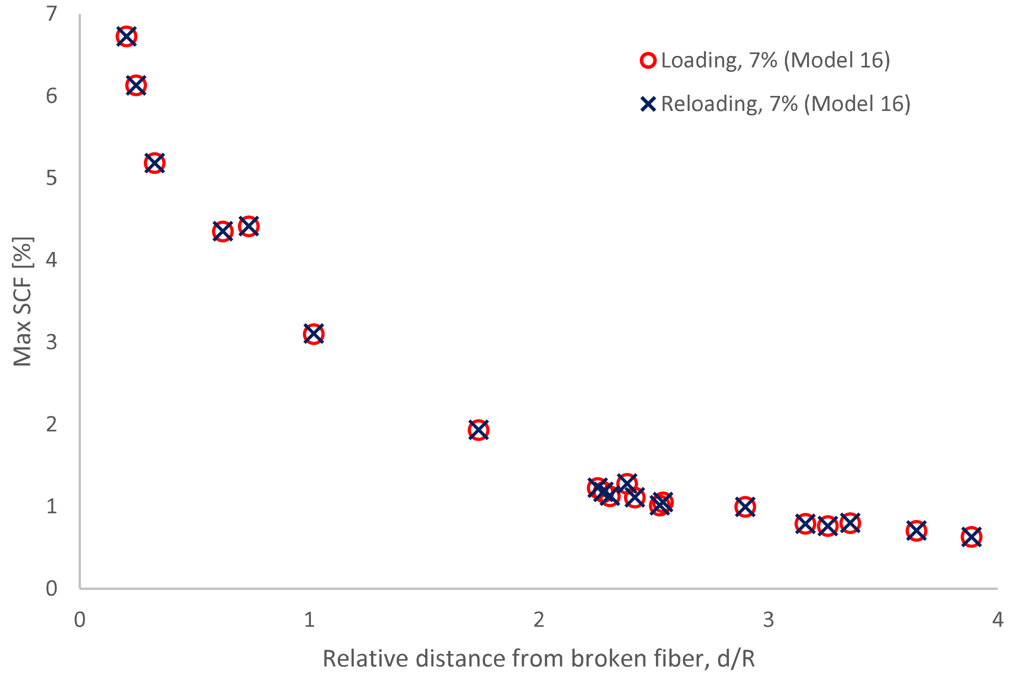

Figure 6.12. Maximum cross-sectional average SCF results of loading and reloading for 7% applied strain.

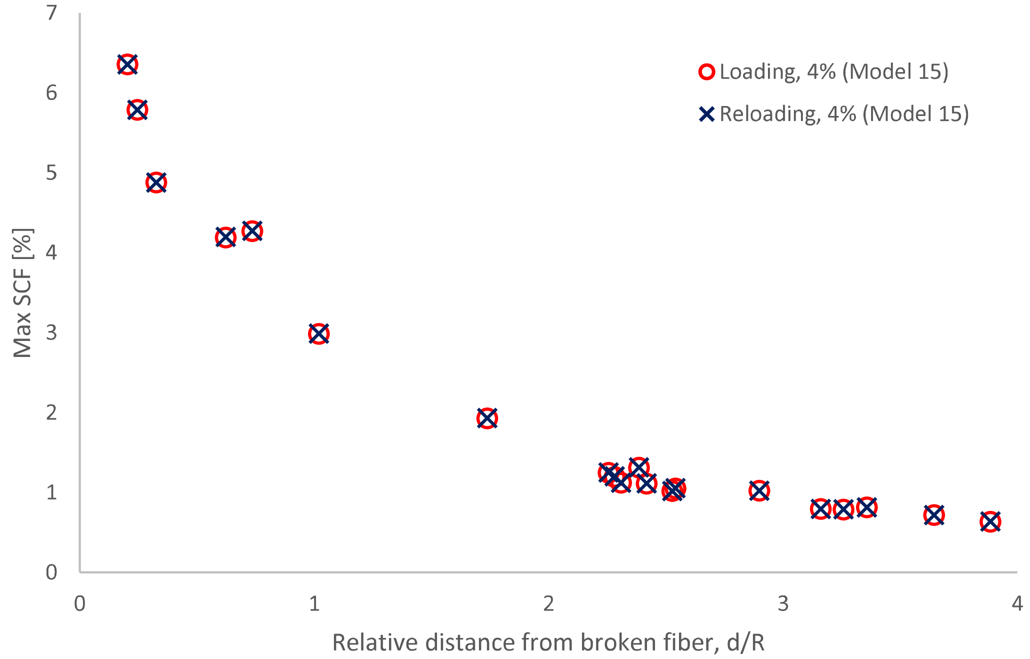

Figure 6.13. Maximum cross-sectional average SCF results of loading and reloading for 4% applied strain.

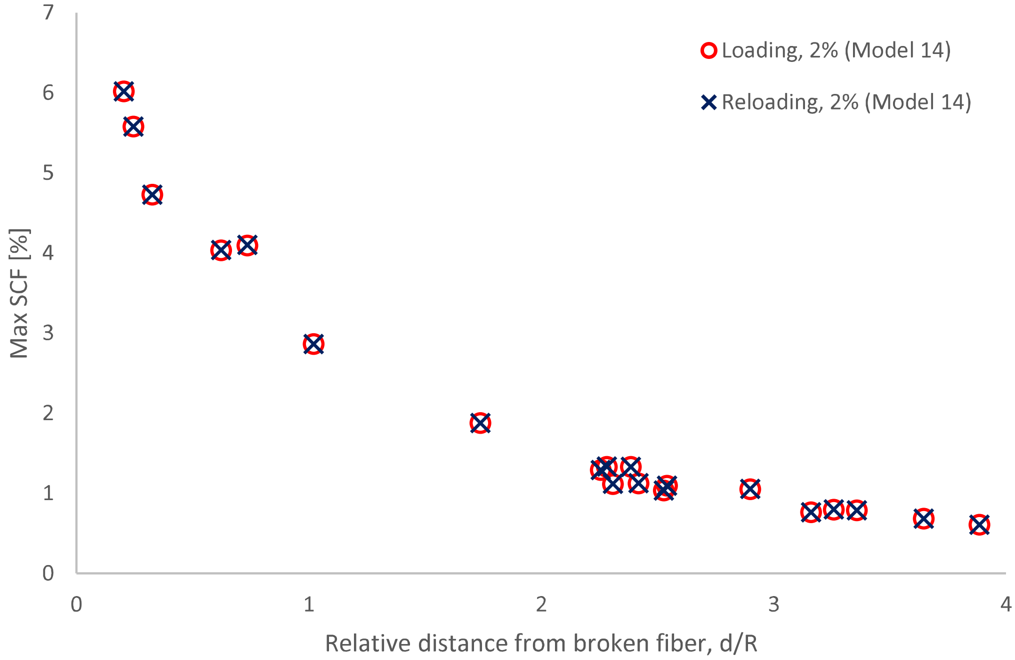

Figure 6.14. Maximum cross-sectional average SCF results of loading and reloading for 2% applied strain.

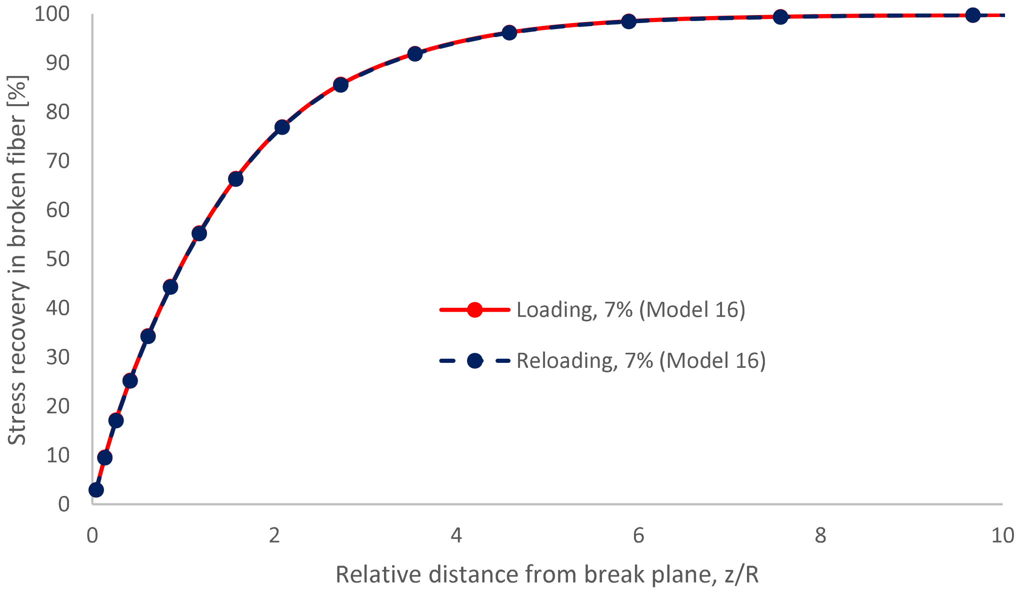

Figure 6.15. Stress recovery results of loading and reloading for 7% applied strain.

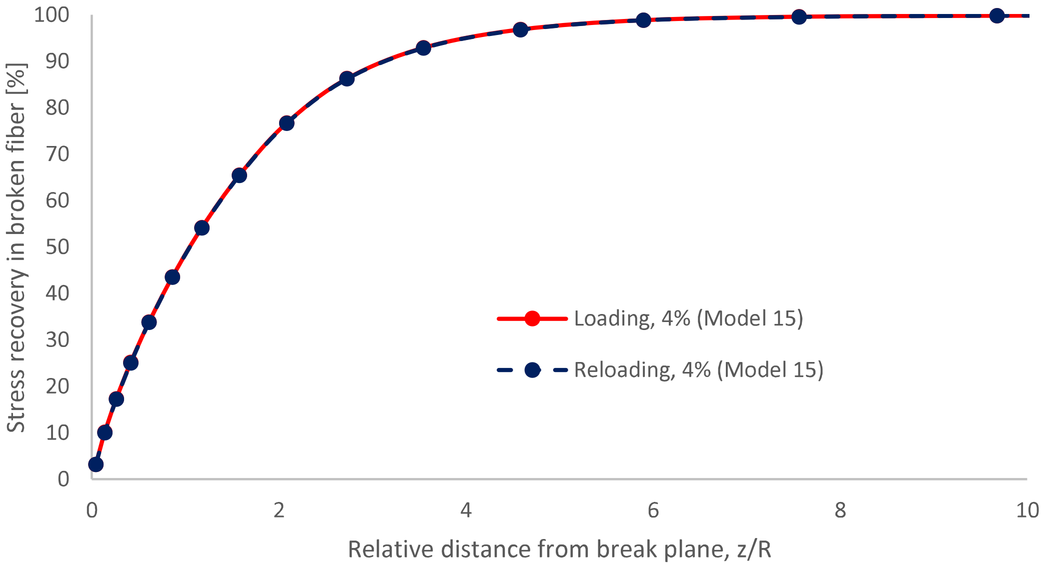

Figure 6.16. Stress recovery results of loading and reloading for 4% applied strain.

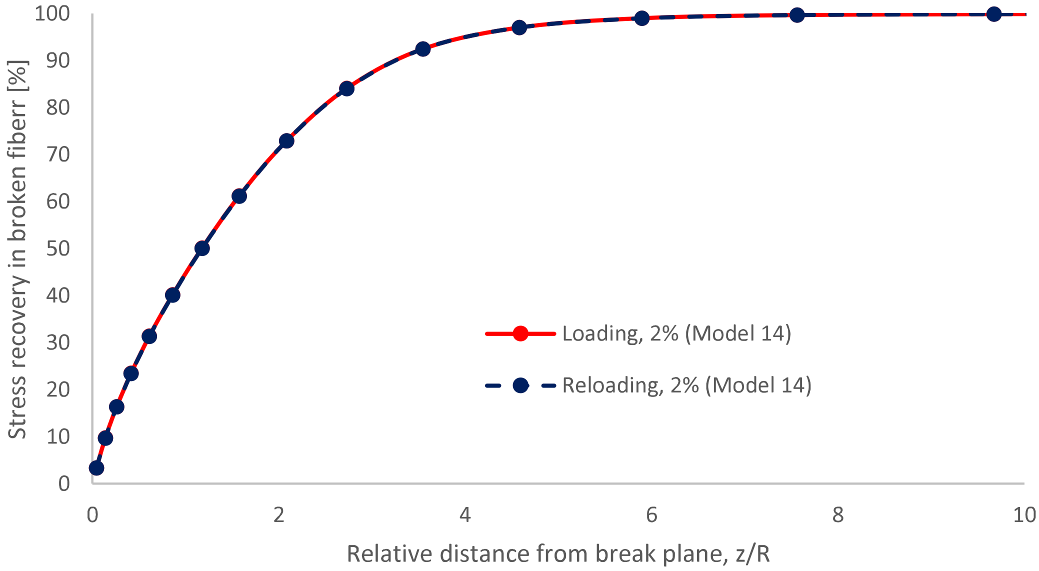

Figure 6.17. Stress recovery results of loading and reloading for 2% applied strain.

It is obvious from the figures that maximum cross-sectional average SCF and ineffective length results of loading and reloading processes are the same for all applied strains. The stress levels on the fibers after both processes are the same as well. The presented results are expected to be accurate only for a few cycles of loading as polymeric materials such as epoxy relieve themselves after subsequent loading and so, ratcheting and plastic deformation accumulation are expected after several cycles of loading [34,55]. Thus, a difference in the results is expected as the cycle number is increased.

6.3.3. Reloading in Elastic Limits

In this section, results of 2% and 4% strain loadings (with no prior loading-unloading cycle) are compared with the results for reloading of the composite which has already experienced a higher loading followed by full unloading. Maximum cross-sectional average SCF results of reloading and loading processes for 2% and 4% applied strains are given in Figure 6.18 and Figure 6.19, respectively. Stress recovery results of loading and reloading processes for 2% and 4% applied strains are given in Figure 6.20 and Figure 6.21, respectively.

In reloading, the composite is loaded first with 7% strain, then unloaded to zero load strain (6.7017%) and reloaded to a certain level after which the surface force in fiber direction is obtained as equal to the surface force in the pure loading case with 2% strain. Thus, composite at the end of both cases, loading with 2% strain and reloading, is under the effect of the same external load. At the end of this reloading process, the material reaches to the 6.9403% strain. Lastly, load is increased more to reach the level in which the surface force of the reloaded composite is equal to the surface force in the pure loading case with 4% strain. At the end of this reloading process, the material reaches to the 6.9675% strain. Note that at the end of the reloading process, strain level does not reach to 7% and so, it occurs in elastic range.

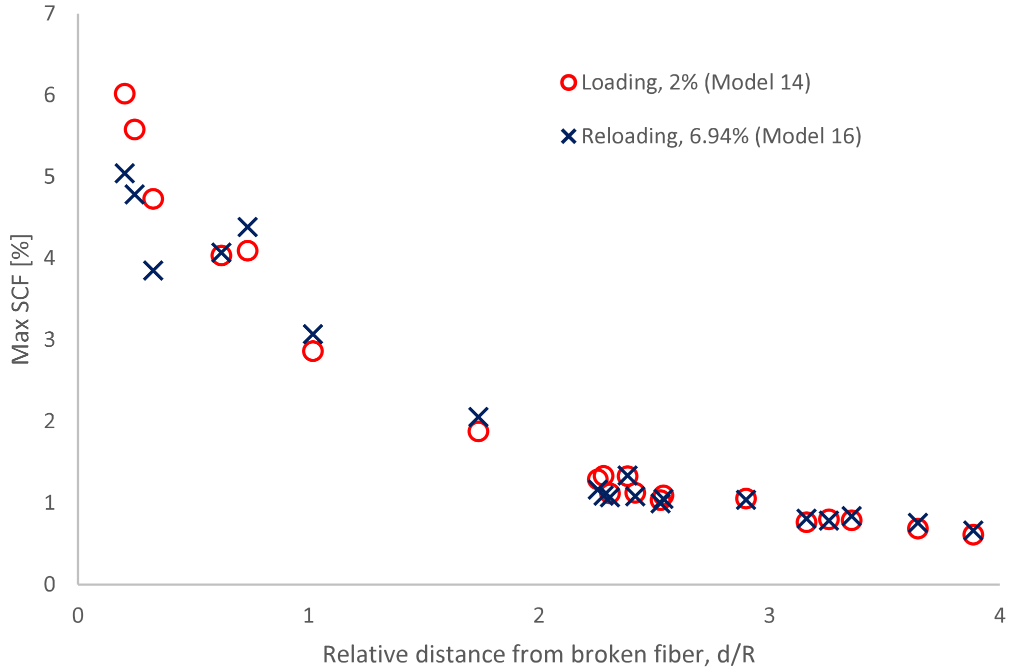

Figure 6.18. Maximum cross-sectional average SCF results of loading with 2% strain and reloading with displacement input corresponding to force that gives 2% strain to undeformed composite.

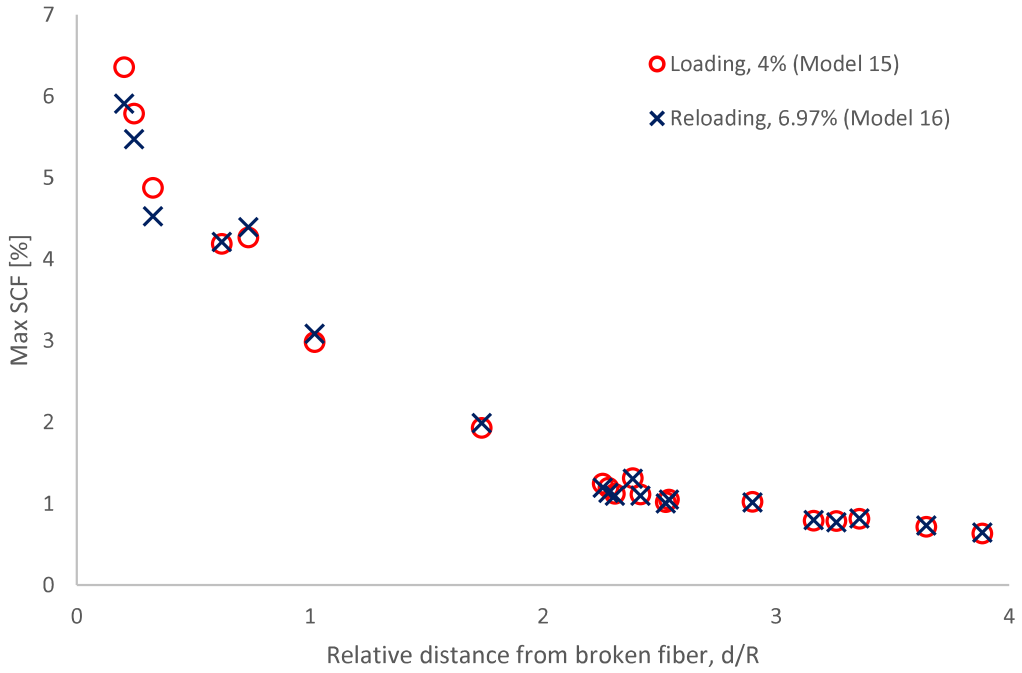

Figure 6.19. Maximum cross-sectional average SCF results of loading with 4% strain and reloading with displacement input corresponding to force that gives 4% strain to undeformed composite.

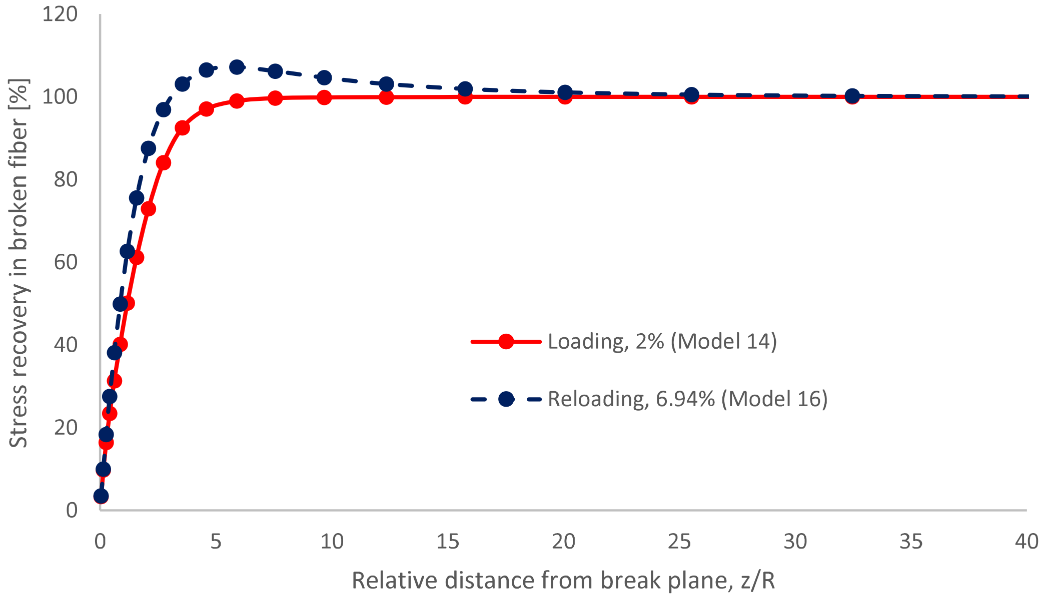

Figure 6.20. Stress recovery results of loading with 2% strain and reloading with displacement input corresponding to force that gives 2% strain to undeformed composite.

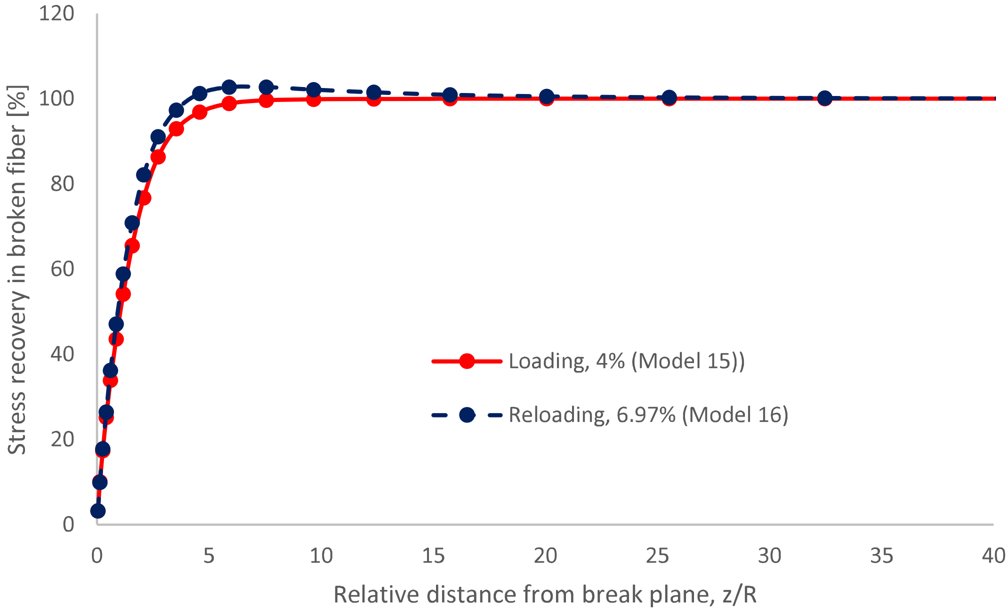

Figure 6.21. Stress recovery results of loading with 4% strain and reloading with displacement input corresponding to force that gives 4% strain to undeformed composite.

As seen in Figure 6.18, SCF results in reloading are lower than those in loading for the first three closest fibers to the broken fiber and there are slight differences for the rest of the fibers. Also, stress recovery occurs more rapidly in reloading (see Figure 6.20). Besides, stress levels on the fibers in reloading process are slightly lower than those in loading process which is shown in Figure 6.22. Considering these results, it can be said that composite at the end of reloading process is in less critical condition, but with small differences. These differences are smaller for the case of 4% strain (see Figure 6.19 and Figure 6.21) and as it is shown in section 6.3.2, the results become equal when the material is reloaded to the initial loading strain (7%).

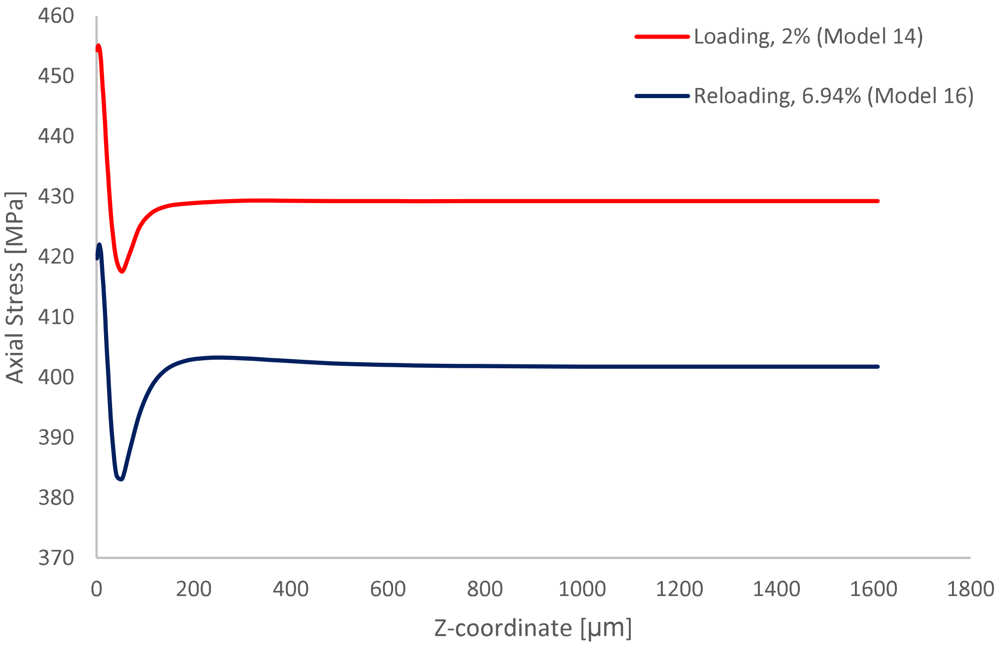

Figure 6.22. Axial stress vs. axial distance plot of the closest fiber in loading with 2% strain and reloading with displacement input corresponding to force that gives 2% strain to undeformed composite.

CHAPTER 7

CONCLUSIONS

7.1. Summary

A comprehensive understanding of mechanical behavior of structural materials is an important issue for designers and engineers to be able to cope with the difficulties encountered or to manufacture better parts. Fiber-reinforced composites are among these structural materials and understanding mechanical behavior and failure mechanism of them is necessary due to their widespread use. In this study, finite element models were developed to understand the mechanical behavior of steel fiber-reinforced composites in case of a broken fiber under longitudinal tensile loading. Stress concentration factors and ineffective lengths were investigated by executing several finite element analyses for different parameters, such as cross-sectional fiber shape, material property, applied strain and fiber volume fraction. Considering the previous studies in the literature, there are some novelties in this study. Basically, steel fiber-reinforced composite materials were examined under longitudinal loading. Peak SCFs were calculated and investigated by using finite element approach. Different from the hexagonal-shaped fibers in the literature which are oriented to the same direction, the hexagonal fibers in this study are randomly rotated around their longitudinal axes. Models created with this modification are more realistic representations of real-life composite structures. Also, steel is defined with elastoplastic material properties which is the actual property of ductile steel fibers. Relatively higher strain values are applied to the models and accordingly results with respect to different strain levels are compared. A hypothetical model is developed and matrix material properties which can enhance the structural integrity of the composite material is suggested.

The study started with the parametric finite element model development. Several models for different parameters were created. The details of parametric finite element model development were explained in chapter 3. The accuracy of the models also verified in this chapter. After creating the models, in chapter 4, effects of cross-sectional shapes of fibers on SCF and ineffective length were examined with respect to peak and cross-sectional average fiber stresses. Hexagonal and circular cross-sectional shapes were used for this purpose. Also, shape comparison was performed by defining different mechanical properties to constituent materials. In chapter 5, effects of different mechanical properties of materials on SCF and ineffective length were investigated in terms of cross-sectional average fiber stresses. Mechanical behavior of both fiber and matrix materials were examined separately. Effects of applied strain were analyzed in this chapter as well. Finally, different from the chapters 4 and 5 with only loading process, SCF and ineffective length results were obtained for unloading and reloading processes in chapter 6.

7.2. Key Findings and Outcomes

Key findings and outcomes obtained from this study can be summarized as follows:

1. Cross-sectional shape of fibers barely affects the cross-sectional average SCF and ineffective length results under longitudinal tensile loading. Those negligibly small differences between hexagonal and circular shapes are due to the rotations of the hexagons around their longitudinal axes.
2. Rather than the cross-sectional shape of fibers, the surface-to-surface distance between the intact and the broken fibers affects the stress concentrations of intact fibers in terms of peak stresses.
3. In case the elastic limit is reached, plastic behavior of steel fibers reduces the stress concentrations in intact fibers and speeds up the stress recovery in broken fiber while the plastic behavior of matrix increases the stress concentrations and slows down the stress recovery.

4. The effects of applied strain in the plastic region on stress concentrations depend on the relative mechanical properties of fibers and epoxy in the plastic region. Thus, calculating SCFs at a strain close to failure strain of the composite gives more accurate results [9].
5. Sustaining a high stiffness of elastic matrix material results in smaller stress concentrations and faster stress recovery in case of a fiber break. This means that a composite material including such a matrix material will be more immune to a fiber break. Using a matrix material which remains elastic throughout the loading and therefore, preserves its stiffness will be beneficial for enhancing the structural integrity of the products.
6. Stress concentrations are much higher and stress recovery process is much slower for unloading process compared to loading process. Despite these characteristics, materials after unloading process are not in a critical condition since the material is in unloaded condition and the residual stress values on the fibers after unloading process are much lower than those after loading process. Besides, the fibers are in compression.
7. Stress concentrations in intact fibers and stress recovery profiles of broken fibers for loading and reloading processes are the same for all applied strains if the material is reloaded to the initial strain in loading process. An occasional loading – unloading – reloading to initial strain cycle would not make the situation worse so far as the SCFs are concerned.
8. If the material is reloaded to a lower loading levels than the initial loading, slightly smaller SCFs and faster stress recovery with slightly smaller stress levels in fibers are obtained in reloading compared to loading at the same lower loading level. Concerning the SCFs, the material after reloading is in less critical condition for this case.

7.3. Future Work

Evaluating the key findings and outcomes of this study, some suggestions can be presented as a future work.

1. All the results presented in this study are output of static loading. This parametric study can be conducted to obtain stress concentrations and ineffective lengths for dynamic loading conditions.
2. A mathematical strength model or models can be created to estimate the failure strain of steel fiber-reinforced composites by using the results obtained in this study. These models can be created in a way that they may use the results for both static and dynamic loadings or use them separately.
3. With increasing computational power, mathematical strength models for composites can be combined with finite element models with bigger scales. While loading the material and calculating the stress concentrations, calculations regarding to failure of the composite can be done simultaneously. Thus, progressive failure analyses of composites can be executed for strength and failure strain prediction.
4. Interactions between multiple fiber breaks may affect the stress redistributions around fiber breaks. Therefore, multiple fiber breaks can be modeled for steel fiber composites with finite element approach and their results can be implemented in the strength models of composite materials.

REFERENCES

[1] Y. Swolfs, R. M. McMeeking, I. Verpoest, and L. Gorbatikh, “Matrix cracks around fibre breaks and their effect on stress redistribution and failure development in unidirectional composites,” *Compos. Sci. Technol.*, 2015.

[2] M. G. Callens, L. Gorbatikh, and I. Verpoest, “Tensile behaviour of ductile steel fibre/epoxy composites,” *ECCM 2012 - Compos. Venice, Proc. 15th Eur. Conf. Compos. Mater.*, 2012.

[3] M. G. Callens, P. De Cuyper, L. Gorbatikh, and I. Verpoest, “Effect of fibre architecture on the tensile and impact behaviour of ductile stainless steel fibre polypropylene composites,” *Compos. Struct.*, 2015.

[4] M. G. Callens, L. Gorbatikh, E. Bertels, B. Goderis, M. Smet, and I. Verpoest, “Tensile behaviour of stainless steel fibre/epoxy composites with modified adhesion,” *Compos. Part A Appl. Sci. Manuf.*, 2015.

[5] A. K. Ghosh, E. Bertels, B. Goderis, M. Smet, D. Van Hemelrijck, and B. Van Mele, “Optimisation of wet chemical silane deposition to improve the interfacial strength of stainless steel/epoxy,” *Appl. Surf. Sci.*, 2015.

[6] M. G. Callens, L. Gorbatikh, and I. Verpoest, “Ductile steel fibre composites with brittle and ductile matrices,” *Compos. Part A Appl. Sci. Manuf.*, 2014.

[7] K. Allaer, I. De Baere, P. Lava, W. Van Paepegem, and J. Degrieck, “On the in-plane mechanical properties of stainless steel fibre reinforced ductile composites,” *Compos. Sci. Technol.*, 2014.

[8] F. M. Zhao and N. Takeda, “Effect of interfacial adhesion and statistical fiber strength on tensile strength of unidirectional glass fiber/epoxy composites. Part II: Comparison with prediction,” *Compos. Part A Appl. Sci. Manuf.*, 2000.

[9] Y. Swolfs, I. Verpoest, and L. Gorbatikh, “A review of input data and modelling assumptions in longitudinal strength models for unidirectional fibre-reinforced composites,” *Composite Structures*. 2016.

[10] R. L. Smith, S. L. Phoenix, M. R. Greenfield, R. B. Henstenburg, and R. E. Pitt, “Lower-Tail Approximations for the Probability of Failure of Three-Dimensional Fibrous Composites with Hexagonal Geometry,” *Proc. R. Soc. A Math. Phys. Eng. Sci.*, 2006.

[11] Y. Swolfs, L. Gorbatikh, V. Romanov, S. Orlova, S. V. Lomov, and I. Verpoest, “Stress concentrations in an impregnated fibre bundle with random fibre packing,” *Compos. Sci. Technol.*, 2013.

[12] H. Fukuda, “Stress concentration factors in unidirectional composites with

random fiber spacing," *Compos. Sci. Technol.*, 1985.

[13] B. W. ROSEN, "Tensile failure of fibrous composites," *AIAA J.*, 2008.

[14] B. Sabuncuoglu, S. Orlova, L. Gorbatikh, S. V. Lomov, and I. Verpoest, "Micro-scale finite element analysis of stress concentrations in steel fiber composites under transverse loading," *J. Compos. Mater.*, 2015.

[15] J. M. Hedgepeth, "Stress concentrations in filamentary structures," *Fibre Sci. Technol.*, 1970.

[16] J. M. Hedgepeth and P. Van Dyke, "Local Stress Concentrations in Imperfect Filamentary Composite Materials," *J. Compos. Mater.*, 1967.

[17] M. R. Nedele and M. R. Wisnom, "Three-dimensional finite element analysis of the stress concentration at a single fibre break," *Compos. Sci. Technol.*, 1994.

[18] Z. Xia, T. Okabe, and W. A. Curtin, "Shear-lag versus finite element models for stress transfer in fiber-reinforced composites," *Compos. Sci. Technol.*, 2002.

[19] A. E. Scott, I. Sinclair, S. M. Spearing, A. Thionnet, and A. R. Bunsell, "Damage accumulation in a carbon/epoxy composite: Comparison between a multiscale model and computed tomography experimental results," *Compos. Part A Appl. Sci. Manuf.*, 2012.

[20] A. Thionnet, H. Y. Chou, and A. Bunsell, "Fibre break processes in unidirectional composites," *Compos. Part A Appl. Sci. Manuf.*, 2014.

[21] Q. D. Zeng, Z. L. Wang, and L. Ling, "A study of the influence of interfacial damage on stress concentrations in unidirectional composites," *Compos. Sci. Technol.*, 1997.

[22] C. M. Landis and R. M. McMeeking, "Stress concentrations in composites with interface sliding, matrix stiffness and uneven fiber spacing using shear lag theory," *Int. J. Solids Struct.*, 1999.

[23] Z. Xia, W. A. Curtin, and P. W. M. Peters, "Multiscale modeling of failure in metal matrix composites," *Acta Mater.*, 2001.

[24] R. Lane, S. . Hayes, and F. . Jones, "Fibre/matrix stress transfer through a discrete interphase: 2. High volume fraction systems," *Compos. Sci. Technol.*, 2001.

[25] P. W. J. van den Heuvel, S. Goutianos, R. J. Young, and T. Peijs, "Failure phenomena in fibre-reinforced composites. Part 6: A finite element study of stress concentrations in unidirectional carbon fibre-reinforced epoxy composites," *Compos. Sci. Technol.*, 2004.

[26] A. C. Johnson, F. M. Zhao, S. A. Hayes, and F. R. Jones, "Influence of a matrix crack on stress transfer to an α-alumina fibre in epoxy resin using FEA and

photoelasticity," *Compos. Sci. Technol.*, 2006.

[27] H. Li, Y. Jia, G. Mamtimin, W. Jiang, and L. An, "Stress transfer and damage evolution simulations of fiber-reinforced polymer-matrix composites," *Mater. Sci. Eng. A*, 2006.

[28] P. W. J. Van Den Heuvel, M. K. Wubbolts, R. J. Young, and T. Peijs, "Failure phenomena in two-dimensional multi-fibre model composites: 5. a finite element study," *Compos. Part A Appl. Sci. Manuf.*, 1998.

[29] T. Okabe, M. Nishikawa, N. Takeda, and H. Sekine, "Effect of matrix hardening on the tensile strength of alumina fiber-reinforced aluminum matrix composites," *Acta Mater.*, 2006.

[30] S. Behzadi, P. T. Curtis, and F. R. Jones, "Improving the prediction of tensile failure in unidirectional fibre composites by introducing matrix shear yielding," *Compos. Sci. Technol.*, 2009.

[31] B. Fiedler, A. Klisch, and K. Schulte, "Stress concentrations in multiple fibre model composites," *Compos. Part A Appl. Sci. Manuf.*, 1998.

[32] P. W. J. Van Den Heuvel, T. Peijs, and R. J. Young, "Failure phenomena in two-dimensional multi-fibre microcomposites. Part 4: A Raman spectroscopic study on the influence of the matrix yield stress on stress concentrations," *Compos. Part A Appl. Sci. Manuf.*, 2000.

[33] S. Blassiau, A. Thionnet, and A. R. Bunsell, "Micromechanisms of load transfer in a unidirectional carbon fibre-reinforced epoxy composite due to fibre failures. Part 2: Influence of viscoelastic and plastic matrices on the mechanisms of load transfer," *Compos. Struct.*, 2006.

[34] S. Blassiau, A. Thionnet, and A. R. Bunsell, "Three-dimensional analysis of load transfer micro-mechanisms in fibre/matrix composites," *Compos. Sci. Technol.*, 2009.

[35] J. H. Oh, K. K. Jin, and S. K. Ha, "Interfacial strain distribution of a unidirectional composite with randomly distributed fibers under transverse loading," *J. Compos. Mater.*, 2006.

[36] M. G. Knight, L. C. Wrobel, and J. L. Henshall, "Micromechanical response of fibre-reinforced materials using the boundary element technique," *Compos. Struct.*, 2003.

[37] T. Matsuda, N. Ohno, H. Tanaka, and T. Shimizu, "Effects of fiber distribution on elastic-viscoplastic behavior of long fiber-reinforced laminates," in *International Journal of Mechanical Sciences*, 2003.

[38] E. N. Sakharova and A. S. Ovchinskii, "Influence of dynamic effects accompanying rupture of fibers and separation of fibers from the matrix on

interaction between failure micromechanisms of composite materials," *Mech. Compos. Mater.*, 1984.

[39] M. L. Accorsi, A. Pegoretti, and A. T. Dibenedetto, "Dynamic analysis of fibre breakage in single-and multiple-fibre composites," *J. Mater. Sci.*, 1996.

[40] R. O. Ochola, K. Marcus, G. N. Nurick, and T. Franz, "Mechanical behaviour of glass and carbon fibre reinforced composites at varying strain rates," *Compos. Struct.*, 2004.

[41] Z. Z. Du and R. M. McMeeking, "Creep models for metal matrix composites with long brittle fibers," *J. Mech. Phys. Solids*, 1995.

[42] N. Iyengar and W. A. Curtin, "Time-dependent failure in fiber-reinforced composites by matrix and interface shear creep," *Acta Mater.*, 1997.

[43] G. Dai and L. Mishnaevsky, "Fatigue of hybrid glass/carbon composites: 3D computational studies," *Compos. Sci. Technol.*, 2014.

[44] M. R. Wisnom, "The effect of fibre misalignment on the compressive strength of unidirectional carbon fibre/epoxy," *Composites*, 1990.

[45] M. Ryvkin and J. Aboudi, "Three-dimensional continuum analysis for a unidirectional composite with a broken fiber," *Int. J. Solids Struct.*, 2008.

[46] L. G. Zhao, N. A. Warrior, and A. C. Long, "A micromechanical study of residual stress and its effect on transverse failure in polymer-matrix composites," *Int. J. Solids Struct.*, 2006.

[47] S. Behzadi and F. R. Jones, "The effect of temperature on stress transfer between a broken fibre and the adjacent fibres in unidirectional fibre composites," *Compos. Sci. Technol.*, 2008.

[48] L. Mishnaevsky and P. Brøndsted, "Micromechanisms of damage in unidirectional fiber reinforced composites: 3D computational analysis," *Compos. Sci. Technol.*, 2009.

[49] Y. Swolfs, L. Gorbatikh, and I. Verpoest, "Stress concentrations in hybrid unidirectional fibre-reinforced composites with random fibre packings," *Compos. Sci. Technol.*, 2013.

[50] B. Sabuncuoglu, "On the high stress concentrations in steel fiber composites under transverse loading," *J. Reinf. Plast. Compos.*, 2014.

[51] A. R. Melro, P. P. Camanho, and S. T. Pinho, "Generation of random distribution of fibres in long-fibre reinforced composites," *Compos. Sci. Technol.*, 2008.

[52] V. Romanov, S. V. Lomov, Y. Swolfs, S. Orlova, L. Gorbatikh, and I. Verpoest, "Statistical analysis of real and simulated fibre arrangements in unidirectional

composites," *Compos. Sci. Technol.*, 2013.

[53] Dassault Systèmes, "Abaqus 2016 Documentation," © *Dassault Systemes*. 2016.

[54] T. Okabe, K. Ishii, M. Nishikawa, and N. Takeda, "Prediction of tensile strength of unidirectional CFRP composites," *Adv. Compos. Mater.*, 2010.

[55] X. Shen, Z. Xia, and F. Ellyin, "Cyclic deformation behavior of an epoxy polymer. Part I: Experimental investigation," *Polym. Eng. Sci.*, 2004.